

Feasibility Analysis of a Two-Phase Solar Thermal Water Heater

by

Hesham Mellad Alkarak

A thesis submitted to the
School of Graduate Studies
in partial fulfillment of the requirement for the degree of
Master of Mechanical Engineering

Faculty of Engineering & Applied Science

Memorial University of Newfoundland

October 2015

St. John's

Newfoundland

Canada

Abstract

Experiments were conducted to measure the heat transfer characteristics of non-boiling two-phase segmented flow in a solar thermal collector. The solar thermal collector was manufactured to have a serpentine flow path (residential serpentine design) and the diameter of collector pipe was 0.0109 m.

The working fluids used in the experiments were water, ethylene glycol and air. Single phase water was examined first, and the results were used as a basis for comparison for the water-air two-phase flow results. Two-phase experiments using ethylene glycol-air and single phase ethylene glycol were then conducted. The flow rates of the water-air and ethylene glycol-air phases were varied between a range of values during each experiment and the system pressure and temperatures were recorded at each combination of flow rates.

The experimental data was used to calculate the number of variables, such as the heat transfer rate Q , temperature difference between the entrance and exit of the solar thermal collector ΔT , average bulk temperature \bar{T}_b , the time required for raising the temperature inside the tank from 25°C to 70°C, and the energy gained from the tank \dot{E} . It has been shown that the heat transfer enhancement of two-phase flow system was better than the single phase flow system.

Several experiments were conducted to study the effects of liquid void fraction α_l . The effect of liquid void fraction showed that the heat transfer rate was highest in all experiments when the liquid void fraction was 0.5, while the heat transfer rate was at its lowest value when the liquid void fraction was 0.79. The effect of void fraction was found to be a controlling factor due to its impact on liquid slug length, which in turn affects the heat transfer rate. Finally, the four two-phase experiments were compared with single phase flow experiment. The result illustrated that the two-phase flow system was better than the single phase flow system.

Acknowledgement

I am deeply indebted to my thesis supervisors and research advisors; Dr. Yuri Muzychka, Professor in Department of Mechanical Engineering at Memorial University of Newfoundland, and Dr. Kiven Pope, Assistant Professor of Mechanical Engineering. Grateful acknowledgment is due for their sincere support, valuable guidance, fruitful discussions, and comments throughout the courses of this study. I would like to thank them for giving me this great opportunity; it was a rewarding experience, both professionally and personally.

I would like to thank the staff at Mechanical Department Laboratory who have helped me a lot, made my work easier, and added pleasant moments to my work, Tom Pike.

I wish to acknowledge the support and cooperation of my colleagues, and classmates during my study at Memorial University. I would also like to thank my parents, my brothers, and my sisters. These people supported me throughout my studies and encouraged me when I need it.

Table of Contents

Abstract	i
Acknowledgements	ii
List of Table	vi
List of Figures	vii
Nomenclature	ix
Chapter 1 - Introduction	1
1.1 General	1
1.2 Two-Phase Flow	1
1.3 Flow-Pattern Definitions and Classifications	2
1.3.1 Horizontal and Near-Horizotal Flow	3
1.3.1.1 Stratified Flow (ST)	3
1.3.1.2 Intermittent Flow (I)	4
1.3.1.3 Annular Flow (A)	4
1.3.1.4 Dispersed-Bubble Flow (DB)	4
1.3.2 Vertical and Sharply Inclined Flow	4
1.3.2.1 Bubble Flow	5
1.3.2.2 Slug Flow	5
1.3.2.3 Churn Flow	5
1.3.2.4 Annular Flow	5
1.3.2.5 Dispersed-Bubble Flow	6
1.4 Segmented Flow	6
1.5 Solar Water Heating Systems	6
1.5.1 Types of Solar Water Heating Systems	7
1.5.1.1 Open and Closed Systems	7
1.5.1.2 Direct and Indirect Systems	8
1.5.1.3 Integrated Collector Storage System (Passive)	8
1.6 Solar Energy Collectors	8
1.6.1 Flat Plate Collectors	9
1.6.2 Collector Performance	10
1.7 Research Objective	11
1.8 Outline	11

3.7.5 Intermediate Tubing	45
3.7.6 Air Injection System	45
3.7.6.1 Compressor and Air Hose	46
3.7.6.2 Injection Manifold	46
3.7.6.3 Solenoid Valve	47
3.7.6.4 PIC Controller	48
3.7.7 Data Collection	48
3.7.8 Setup and Operation of Experiment	48
3.7.9 Fluids	50
Chapter 4 - Experimental Results	51
4.1 Introduction	51
4.2 Data Analysis	51
4.3 Single-and Two-Phase Flow in a Solar Collector with Water	52
4.4 Single-and Two-Phase Flow in a Solar Collector with Glycol	60
4.5 Experiments at Variable Liquid Void Fraction	79
Chapter 5 - Conclusion and Recommendations	89
5.1 Conclusion of Present Study	89
5.2 Recommendations for Future Work	90
References	51
Appendix A - Solar Thermal Collector Specification	91
Appendix B - Compressor Specification	94
Appendix C - Solenoid Valve Specification	100
Appendix D - PIC Microcontroller Code	103
Appendix F - Measurement Devices Specifications	105
Appendix G – Turbine Flow Meter Specifications	118

List of Table

Table 2.1: Values of Chisholm Constant.....	15
Table 3.1: Components of the injection manifold.....	47
Table 3.2: Components of the solenoid valve.....	47
Table 3.3: The properties of water, glycol and air.....	50
Table 4.1: Summary of results for single-phase (water) and two-phase flow (water-air) experiments.....	60
Table 4.2: Summary of single-phase (glycol) and two-phase flow (glycol-air) experiments.....	78
Table 4.3: Experimental heat transfer enhancement of a two-phase flow solar collector.....	78
Table 4.4: Summary of experiments at variable liquid void fraction.....	79

List of Figures

Figure 1.1: Gas-liquid flow regimes in horizontal pipes.....	3
Figure 1.2: Gas-liquid flow regimes in vertical pipes.....	5
Figure 1.3: Schematic diagram of natural circulation system (Goswani et al, 2000).....	7
Figure 1.4: Flat plate collector (solar server, 2011).....	9
Figure 1.5: Flat plate collector exploded view (sabonnadiere, 2009).....	10
Figure 3.1: Internal liquid plug circulation (a) hydrophobic surface (b) hydrophilic surface (Muzychka, 2011).....	29
Figure 3.2: Gas-liquid slug flows for different slug length (Muzychka, 2011).....	30
Figure 3.3: Geometry of void fraction.....	36
Figure 3.4: System Configuration.....	42
Figure 3.5: Serpentine design of flat plate.....	43
Figure 3.6: Light table.....	43
Figure 3.7: Configuration of air injection system.....	46
Figure 3.8: Injection manifold.....	46
Figure 3.9: Solenoid valve components.....	47
Figure 4.1: Thermal effectiveness at 1.552 (L/min) for (a) inlet and outlet temperature,(b) temperature difference, and (c) heat transfer rate.....	54
Figure 4.2: Thermal effectiveness at 2.062 (L/min) for (a) inlet and outlet temperature,(b) temperature difference and (c) heat transfer rate.....	57
Figure 4.3: Thermal effectiveness at 2.516 (L/min) for (a) Inlet and outlet temperature,(b) temperature difference and (c) heat transfer rate.....	59
Figure 4.4: Transient thermal effectiveness at 0.653 (L/min) for (a) inlet and outlet temperature,(b) temperature difference, (c) heat transfer rate, (d) temperature difference in the tank, and (e) average bulk and tank temperature.....	64

Figure 4.5: Transient thermal effectiveness at 1.7071 (L/min) for (a) inlet and outlet temperature,(b temperature difference, (c) heat transfer rate, (d) temperature difference in the tank, and (e) average bulk and tank temperature.....	69
Figure 4.6: Transient thermal effectiveness at 2.148 (L/min) for (a) inlet and outlet temperature,(b) temperature difference, (c) heat transfer rate, (d) temperature difference in the tank, and (e) average bulk and tank temperature.....	73
Figure 4.7: Transient thermal effectiveness at 2.987 (L/min) for (a) inlet and outlet temperature,(b) temperature difference, (c) heat transfer rate, (d) temperature difference in the tank, and (e) average bulk and tank temperature.....	77
Figure 4.8: Transient thermal effectiveness for two-phase flow at 1.368 (L/min) and liquid void friction of 0.79 for (a) inlet and outlet temperature, (b) heat transfer rate, and (c) average bulk and tank temperature.....	81
Figure 4.9: Transient thermal effectiveness for two-phase flow at 1.306 (L/min) and liquid void friction of 0.51 for (a) inlet and outlet temperature, (b) heat transfer rate, and (c) average bulk and tank temperature.....	83
Figure 4.10: Transient thermal effectiveness for two-phase flow at 1.369 (L/min) and liquid void friction of 0.66 for (a) inlet and outlet temperature, (b) heat transfer rate, and (c) average bulk and tank temperature.....	85
Figure 4.11: Transient thermal effectiveness for two-phase flow at 1.331 (L/min) and liquid void friction of 0.5 for (a) inlet and outlet temperature, (b) heat transfer rate, and (c) average bulk and tank temperature.....	87
Figure 4.12: Transient tank temperature at different two-phase flow rates.....	88
Figure 4.13: Transient tank temperature at different liquid void fractions.....	88

Nomenclature:

A	Area, m^2
A_g	Cross-sectional area of air, m^2
A_l	Cross-sectional area of liquid, m^2
B_o	Bond number
C	Chisholm constant
C	Model constant – Eq.(2.31)
C_a	Capillary number
c	Concentration, mol/m^3 – Eq.(2.11), (2.12), (2.13)
c	Capacitance, F – Eq.(2.25), (2.26), (2.27)
c_p	Specific heat, $\text{J}/\text{kg}\cdot\text{K}$
D	Diameter, m
D_h	Hydraulic diameter, m
D_i	Internal diameter, m
D_t	Tube diameter, m
dp/dz	Pressure gradient, Pa/m
\dot{E}	Gained energy from tank, W
E_o	Eötvös number
f	Fanning friction factor
F_r	Froude number
g	Gravitaty force, m/s^2
G	Mass flux, $\text{kg}/m^2 \cdot s$
G_z	Graetz number
h	Heat transfer coefficient, $\text{W}/m^2 \cdot K$
\bar{h}	Average heat transfer coefficient, $\text{W}/m^2 \cdot k$
H	Height of channel, m
H	Vertical height, m – Eq.(3.43)
J	Rate of transfer, mol/m – Eq.(3.43)
J	Volumetric flux, m/s – Eq.(3.38)
k	Thermal conductivity, $\text{W}/\text{m}\cdot\text{k}$

L	Channel length, m
L_a	Laplace number
L_g	Gas length, m
L_l	Liquid length, m
L^*	Dimensionless length
L_s^*	Dimensionless plug length
\dot{m}	Mass flowrate, kg/s
Nu	Nusselt number
\bar{Nu}	Average Nusselt number
Nu_{SP}	Single-phase Nusselt number
Nu_{TP}	Two-phase Nusselt number
Nu_w	Nusselt number for fully developed flow
n	Droplet ratio – Eq.(2.26), (2.27)
n	Blending parameter – Eq.(2.43)
P	Pressure, Pa – Eq.(3.42)
ΔP	Differential pressure, Pa
$\Delta P_{friction}$	Frictional pressure drop, Pa
$\Delta P_{momentum}$	Momentum pressure drop, Pa
ΔP_{static}	Static pressure drop, Pa
P	Fitting parameter
Pe	Peclet number
Pr	Prandtl number
\dot{Q}	Flow rate, m^3/s
q	Heat transfer rate, W
q^*	Dimensionless heat transfer
r	Radius, m
R^*	Coiled aspect ratio
R_L	Liquid holdup
Re	Reynolds number
Re_{TP}	Two-phase of Reynolds number
T	Temperature, K
T_a	Dimensionless average temperature of fluid, K
T_i	Inlet temperature, K

T_m	Bulk temperature, K
T_o	Outlet temperature, K
T_r	Time required to heat tank, hr
T_w	Wall temperature, K
\bar{T}_{bulk}	Average bulk temperature in solar thermal collector, °C
\bar{T}_w	Mean wall temperature, K
ΔT_{ln}	Log mean of temperature difference
$\frac{\Delta T}{\Delta t}$	Slope tank temperature, °C/hr
S	Slip ratio
S_{Tank}	Slope tank temperature, °C/hr
u	Velocity, m/s
u_b	Bubble velocity, m/s
\bar{u}_{drop}	Average bulk velocity, m/s
V	Voltage, V – Eq.(2.25)
V	Amount of working fluid in the tank, m^3
W	Channel width, m
W_a	Weber number
x	mass quality or mass fraction
x_i	Inlet of mass fraction
x_o	Outlet of mass fraction
X	Lockhart-Martinelli parameter
z^*	Dimensionless position for thermally developing flow

Greek Symbols

ϕ_l	Liquid two-phase flow multiplier
ϕ_g	Gas two-phase flow multiplier
α_l	Liquid void fraction
α_g	Gas void fraction
ε	Aspect ratio
γ	Shape factor
ζ	Arbitrary length scale
ρ	Density, kg/m^3

μ	Dynamic viscosity, $\text{N.s}/\text{m}^3$
θ	Angle with respect to horizontal position
θ_m	Dimensionless mean temperature of bulk
α_{ch}	Void fraction (length)
α_{c-s}	Void fraction (cross-sectional area)
α_{vol}	Void fraction (volume)
β	Volumetric quality
ρ_m	Mean density of both phases, kg/m^3
σ	Surface tension, N/m^2

Subscripts

a	Average
b	Bubble
c	Coil
drop	Droplet
Dev	Developed flow region
Ent	Entrance region
g	Gas phase
i	Inlet
l	Liquid phase
lower	Lower bound
ln	Log mean
LS	Liquid slug
o	Outlet
P	Graetz plug flow
SP	Single-phase
S	Slug flow
TP	Two-phase
t	Tube
upper	Upper bound
w	Wall

Chapter 1

Introduction

1.1 General

This thesis uses a solar collector and aims to design a two-phase solar heater by employing the theoretical principles of gas-liquid segmented slug flow with a constant heat flux. Various experimental studies reveal gas bubbles in the flow stream increases the quantity of heat transferred to the experimenting fluid. If heat transfer is increased, less time is required to heat the fluid. No current devices exist that use gas-liquid segmented plug flow for solar water heaters; and this thesis aims to prove the applicability of this concept. Experiments are conducted by the developing single phase flow as a base and compared with two-phase flow. The main aim of this thesis is to improve the performance and heat transfer rate. The system also shows additional improvement in the performance coefficient of the base, suggesting a potential for various commercial applications. Some of the benefits for consumers include a reduction in energy consumption, and heating time, as well as availability for a limited quantity of sunlight. Increasing costs and environmental degradation increase in concerns of typical energy generation. Hot water consumption is a demanding residential applications. If we efficiently harness solar energy to provide a more effective method to supplement either electrical or gas fired water heating, it will provide significant economic and environmental protection. The system can also reduce fossil fuel consumption, and reduce public demands on electrical grids.

1.2 Two-Phase Flow

Two-phase flow mainly occurs in a system that consists of two phases (typically gas-liquid) with a meniscus that separates the phases. Two-phase flow is not only restricted to gas-liquid flows but can also refer to solid-gas, solid-liquid, and liquid-liquid flows. The two-phase flows possess numerous applications that mainly occur in different chemical, petroleum, bio-medical, refrigeration and air-conditioning systems, among

others. The fluid system might be either macro-scale, mini-scale, or micro-scale depending upon the application. Recently, two-phase flows have been reported to have many uses in microfluidic systems including MEMS (micro electromechanical systems), LOC (lab-on-chip) devices and Nano fluidic systems. Numerous researches have also been conducted over the last sixty years, on two-phase flow. Initially research typically focused on macro-scale flows, however, recent researches has focused on both micro-scale and mini-scale flows.

A wide range of different models have been established both analytically and theoretically for predicting pressure drop in two-phase frictional and transport characteristics. These parameters are importance to many engineers who are working with such two-phase flow systems. Furthermore, the models used for two-phase flow can be further categorized into two unique classes: homogenous flow models and separated flow models. The homogenous flow model firstly employs effective fluid properties determined from the important properties of both phases currently in the flow. Major properties such as viscosity and density are mainly determined via effective property models, followed by frictional pressure drop, and then the transport characteristics are calculated by using equations for calculating single phase flow. Typically, a homogenous flow model can be referred to as a zero-slip flow model. Whereas, a separated flow model mainly tries to show that both phases possess unique thermophysical properties and have different velocities.

1.3 Flow-Pattern Definitions and Classifications

The most fundamental difference between the single-phase flows and gas-liquid two-phase is the presence of flow patterns and flow regimes in the case of two-phase flow. Flow pattern basically refers to the overall geometrical configuration of both gas and the liquid phases in the pipe. When gas and liquid simultaneously flows in a pipe, the two phases can actively distribute themselves in a variety of different flow configurations. The flow configurations are significantly different from each other in interface spatial distribution due to different flow characteristics, velocity and the holdup distributions.

All existing patterns of flow in any two-phase flow system are highly dependent on the following variables:

- Operational parameters that include gas and liquid flow rates.
- Physical properties associated with the two phases, including gas and liquid densities, surface tension and viscosities.
- Geometrical variables, such as pipe diameter and inclination angle.

Flow pattern determination is an important problem, specifically in analysis of two-phase flow. Major design variables associated with the flow strongly depend on the existing flow pattern. The design variables include gradient, pressure, heat, mass-transfer coefficients, liquid holdup, residence-time distribution, and chemical reaction.

1.3.1 Horizontal and Near-Horizontal Flow

Flow patterns that are horizontal and near-horizontal can be classified as stratified flow (for both stratified-smooth and stratified-wavy), annular flow, dispersed-bubble flow and intermittent flow (including both the slug flow and elongated-bubble flow). Gas-liquid flow regimes in horizontal pipes are illustrated in Fig. 1.1.

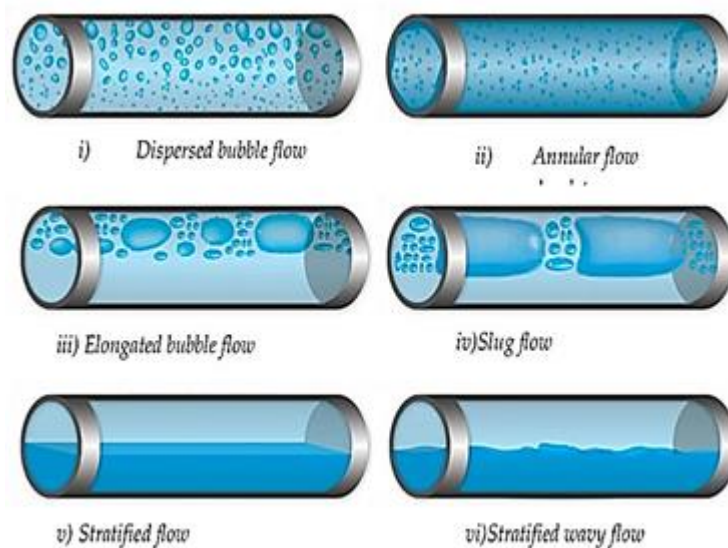


Figure 1.1: Gas-Liquid Flow Regimes in Horizontal Pipes (*Ove Bratland, 2010*)

1.3.1.1 Stratified Flow (ST)

This flow pattern mainly occurs at relatively lower gas and liquid-flow rates. The two phases get separated from the force of gravity, where the liquid-phase typically flows

at the pipe's bottom, while the gas-phase flows at the top. A Stratified-flow pattern is also sub-classified as stratified-smooth or stratified-wavy.

1.3.1.2 Intermittent Flow (I)

Intermittent flow is mainly characterized by the alternative flow of liquid and gas. Either plugs or slugs filling the entire cross-sectional area of the pipe, are separated by gas pockets containing a highly stratified liquid layer that flows along the entire bottom of the pipe. The mechanism of its flow follows that of a fast moving liquid slug that overrides the much more slowly moving liquid film that is placed ahead of it.

1.3.1.3 Annular Flow (A)

Annular flow occurs at a relatively high gas-flow rate. The gas-phase flows at the center and might contain entrained droplets of liquid. The liquid flows specifically in the form of a very thin film present around the pipe wall.

1.3.1.4 Dispersed-Bubble Flow (DB)

At considerably high liquid-flow rates, the liquid-phase typically occurs in nearly a continuous-phase which the entire gas-phase is dispersed in the form of discrete bubbles. The transition to this flow pattern can be defined with the help of a condition in which the bubbles are suspended first in the liquid or gas pockets, which typically touches the very top of the pipes, and are eventually destroyed.

1.3.2 Vertical and Sharply Inclined Flow

For a range of inclination angles, the stratified regime disappears and is replaced by churn flow. The flow patterns are usually more symmetric around the pipe and less affected by the force of gravity. Gas-liquid flow regimes in vertical pipes are illustrated in Fig. 1.2.



Figure 1.2: Gas-Liquid Flow Regimes in Vertical pipes (*Ove Bratland, 2010*)

1.3.2.1 Bubble Flow

In bubble flow, the gas-phase is dispersed into much smaller discrete bubbles that move upward in a zigzag motion as well as in a constant liquid-phase. The distribution of bubbles is nearly homogeneous via the pipe cross section.

1.3.2.2 Slug Flow

Slug flow in vertical pipes is very symmetric around the pipe axis. The majority of the gas-phase is located in a much larger bullet-shaped pocket, known as the Taylor-bubble and has a diameter approximately equal to the pipe diameter. The flow consists of successive Taylor-bubbles as well as liquid slugs filling the pipe's cross section.

1.3.2.3 Churn Flow

Churn flow is characterized by a highly oscillatory motion of the liquid-phase. Churn flow is similar to slug flow, with no clear or strict boundaries between the two phases. Typically, this occurs at much higher gas-flow rates, where the liquid slugs fill the entire pipe and, are much shorter and frothier.

1.3.2.4 Annular Flow

Similar to horizontal flow, this type of flow is characterized by a fast-moving gas center having entrained liquid droplets and a much slower-moving liquid that flows around the entire pipe wall.

1.3.2.5 Dispersed-Bubble Flow

Similar to horizontal flow, dispersed-bubble flow in vertical and highly inclined pipes occurs at a relatively higher liquid-flow rate. The overall gas-phase is dispersed as discrete bubbles in the continuous liquid-phase.

1.4 Segmented Flow

Two-phase segmented flow has been extensively examined over the last ten years. It is characterized by splitting the entire fluid stream into a consecutive series of shorter plugs. One phase is the carrier or base fluid, while the second phase is the segmenting media or dispersed phase. Additionally, many previous researchers referred segmented gas-liquid flow as Taylor plug flow. The main reason is the work of Taylor (1961) who examined plug flows from an understanding of both the film thickness and deposition at the wall. Plug flow (Taylor flow) is the earliest form of segmented flow patterns; however, because surface tension is a non-dominant factor in macro-scale studies, it is almost impossible to create a steady train for the plugs with a thin liquid film.

Within liquid plugs of any segmented flow, the internal circulations will rise due to solid-liquid, gas-liquid, or liquid-liquid interfaces. These thermal enhancements mainly occur in segmented flows because of two mechanisms. One of mechanism is the internal circulations present within the liquid plugs and the other mechanism typically resulted from an increased velocity that was experienced by the liquid plugs, due to reduced liquid fraction, usually for a constant flow rate of mass. Furthermore, the latter was determined to be impossible by Muzychka et al. (2009), who used heat transfer theory. This leaves just the internal circulation mechanism for explaining the thermal enhancement that result from segmented flow.

1.5 Solar Water Heating Systems

Solar water heaters have been used since the 1800s. However, the main difference between early solar water heaters and modern versions is in the configuration modern systems, where the solar heaters are placed on a roof. Solar water heaters are environmentally friendly and help reduce energy bills (Staff and Campbell, 1978). Solar heaters come in different configurations and variations in terms of cost, design,

performance. Many systems also have auxiliary systems such as electricity or gas heaters.

1.5.1 Types of Solar Water Heating Systems

Currently, there are two major types of solar heating system configurations available, including natural and forced circulation. Natural circulation systems are simple and the overall cost of manufacturing is quite low. However, these systems are suitable only for warm climates since freezing occurs in colder climates. Forced circulation systems are more suitable for climates that are below freezing temperatures (Goswani et al, 2000). Natural circulation systems are also called thermosyphon systems. A typical schematic for this type of system is illustrated in Fig. 1.3

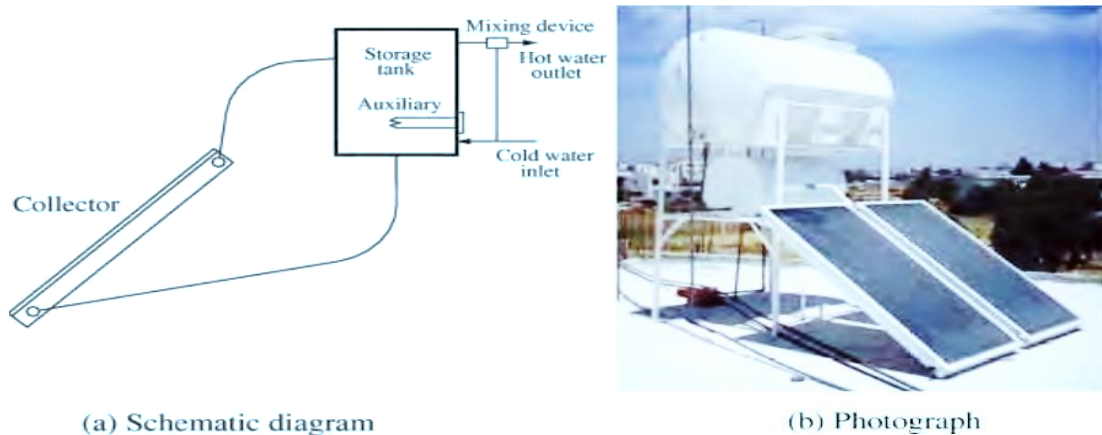


Figure 1.3: Schematic Diagram of Natural Circulation System (Goswani et al, 2000)

There is a wide range of disadvantages associated with thermosyphon solar heating systems since they are relatively taller units which makes them visibly intrusive on buildings and they are prone to damage in windy conditions. The overall design typically incorporates a cold water storage tank installed on the top.

1.5.1.1 Open and Closed Systems

Natural and forced circulation can be further categorized. In an open system, an open container is installed at the highest point to absorb volumetric expansion of the liquid that is caused by changes in temperature. The pressure in open systems is maintained at the static pressure associated with the liquid column. Closed (sealed) systems are typically designed for operating at a higher pressure (1.5-10 bar), which affects physical

properties, including the liquid's evaporation temperature. Closed systems need additional safety devices (German Solar Energy Society, 2007).

1.5.1.2 Direct and Indirect systems

Direct systems typically operate with water that continuously circulates from the solar heating storage tank to the main collector. Direct solar systems can be installed in different configurations. The system is typically connected to a separate pre-heater or can be linked to a combined cylinder having dedicated solar water storage unit. Additionally, this system can be connected to an already existing hot water vessel having a traditional heat source (German Solar Energy Society, 2007). An indirect system possesses two entirely separate circuits: the solar and the cold mains water circuits. This type of system is most commonly used in the UK. The system typically involves transferring heat from the fluid that passes through the main solar collector. This system also has the advantage of preventing contaminants from entering via incoming cold mains can diminish the efficiency of the solar collector (CIBSE, 2007).

1.5.1.3 Integrated Collector Storage Systems (Passive)

Integrated collector storage (ICS) systems employ hot water storage as a part of the solar collector, with the surface of the solar storage tank employed as an absorber. To improve stratification the hot water is drawn from the tank's top and cold water enters the tank's bottom on the opposite side. The major disadvantage associated with ICS systems is related to high thermal losses due to the high surface area of the solar storage tank that cannot be insulated thermally since it is used for absorption. In ICS systems, the water temperature substantially drops during the night, particularly during the winter (Soteris A. Kalogirou, 2003).

1.6 Solar Energy Collectors

Solar energy collectors have similarities to heat exchangers and can transform energy from one form to another, i.e. solar radiation into thermal energy. The main component allowing the exchange or transfer of energy is the solar collector. The solar collector absorbs radiation and converts it into heat. The heat is transferred to a fluid, either water or a glycol mixture, and flows through the collector (Kalogirou, 2004). The energy collected from the process is transferred from the fluid or to a solar water heating storage

tank. Two ways that solar collectors can be mounted are stationary or tracking. For mounting the collector in a stationary position, analysis are needed at the design stage for the optimum inclination of the solar panels for both location and usage. The solar collectors remain fixed to this tilt angle throughout the year. In a tracking system, the solar collector's inclination will change with the sun's angle to receive the optimum amount of solar radiation (Kalogirou, 2004).

1.6.1 Flat Plate Collectors

Flat plate collectors are typically manufactured in two different forms. Solar collectors using liquids with no glazing are manufactured with a black absorbent polymer coating in the absence of any insulated backing. The manufacturing cost for these are low, however, one major disadvantage is they have high heat losses, making them highly inefficient and are not suitable for low temperature installations (Sabonnadiere, 2009).

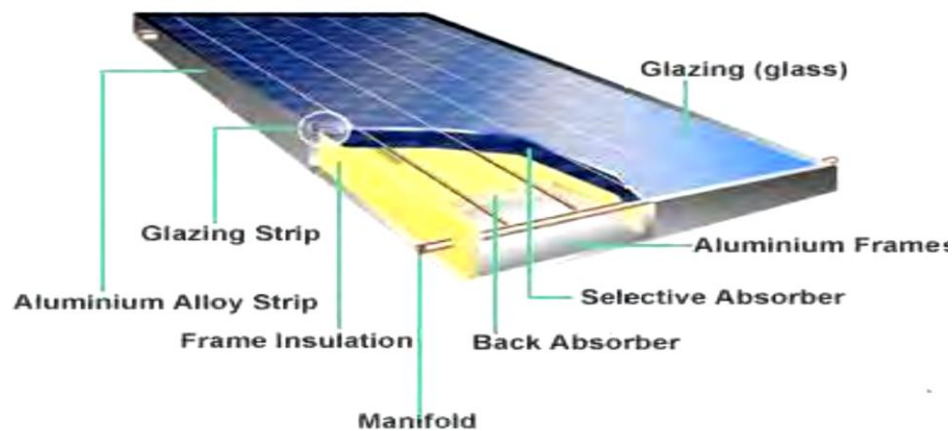


Figure 1.4: Flat Plat Collector (Solar Server, 2011)

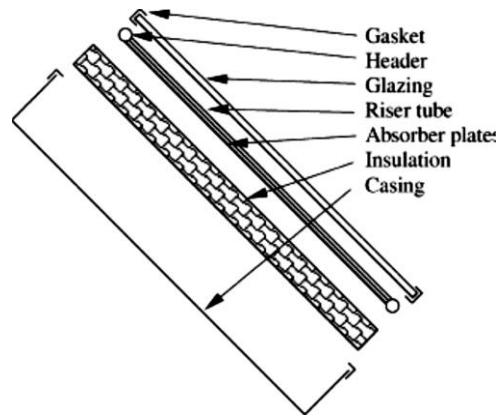


Figure 1.5: Flat Plate Collector Exploded View (Sabonnadiere, 2009)

Another type of flat plate solar collectors employs glazing (Fig. 1.4 & 1.5) and uses an absorber plate to absorb solar radiation and heats copper tubes containing a transfer liquid (Sabonnadiere, 2009). The entire side of the casing and underside of the absorber plate remains heavily insulated to reduce conduction losses during operation. The liquid tubes are welded to the main absorbing plate and can also be manufactured as part of the plate. These tubes are later connected at the ends large diameter header tubes (Kalogirou, 2004).

In order to receive the maximum amount of solar radiation per unit area, a tracking collector should be used. For both maximum efficiency and energy extraction, a solar collector should be aligned perpendicular to solar radiation.

1.6.2 Collector Performance

Collector performance can be characterized by two experimentally determined constants:

- conversion factor: the solar collector efficiency when the ambient air temperature is equal to the collector temperature.
- heat loss coefficient: the mean heat loss of the solar collector per aperture area for any measured temperature difference between the collectors and ambient air temperature.

These solar collector constants are mainly determined in reference to predefined conditions (such as angle of incidence, global radiation intensity, wind velocity, air temperature, etc.) (Fanniger, 2012). Furthermore, the heat balance of a collector should also possess three different components, absorbed heat – lost heat = removed heat by

the transferring fluid. A heat loss coefficient for solar collector is (Sen, 2008) heat loss coefficient = (absorbed heat – lost heat) / incident solar radiation.

1.7 Research Objectives

The main aim of this thesis is to examine the potential and applicability of heat transfer enhancement of uniformly segmented fluid streams. This requires a highly and controllable two-phase segmented plug flow to the solar thermal water heating system, that is optimized the research also compare the thermal water heating system with a benchmark, single-phase system. Two- phase flow at different sizes of liquid length and sizes of air plug length are also examined.

1.8 Outline

The remainder of thesis is organized as follows. Chapter 1 gives an introduction on the concept of using non-boiling two-phase segmented flow as a working fluid. The flow pattern definitions and classifications are presented. Solar water heaters and the types of solar water heaters are illustrated as well. The descriptions of research objectives are introduced. Chapter 2 provides a literature review of works addressing related topics. Chapter 3 shows the mechanism of heat transfer enhancement, system configuration, and components of the experiments. Chapter 4 illustrates the experimental results for the segmented flow used in the solar thermal collector. Chapter 5 provides a conclusion of the current study and recommendations for future studies

Chapter 2

Literature Review

2.1 Introduction

This chapter presents experimental and numerical research on two-phase flows as well as on the two-phase, with a focus on two-phase segmented flow. Improvements needed to implement frictional pressure drop and a transport correlation are developed through extensive research and are organized chronologically.

2.2 Literature Review

In 1949, Lockhart and Martinelli studied two-phase flow with air and liquids that flowed inside pipes having different diameters. The diameters of the pipes ranged from 0.0586 inches to 1.017 inches, and the liquids included kerosene, benzene, water and oils. Four different types of isothermal two-phase and two-component flow were identified, namely the turbulent liquid-turbulent gas, turbulent liquid-laminar gas, laminar liquid-turbulent gas, as well as laminar liquid-laminar gas. Lockhart and Martinelli (1949) correlated both the two-phase pressure drop that resulted from all four flow mechanisms into the following Martinelli parameter X

$$X^2 = \frac{\left(\frac{\Delta P}{L}\right)_l}{\left(\frac{\Delta P}{L}\right)_g} \quad (2.1)$$

Equation (2.1) is related to X by the ratio of both single pressure drops, similar to both individually flowing in the pipe. Lockhart and Martinelli (1949) presented their graphical correlation for each of the flow mechanisms that were identified. The Lockhart-Martinelli plots can be used for determining the two-phase flow characteristics for liquid, as well as gaseous phases with Eq. (2.2) and (2.3):

$$\phi_l^2 = \frac{\left(\frac{\Delta P}{L}\right)_{TP}}{\left(\frac{\Delta P}{L}\right)_l} \quad (2.2)$$

$$\phi_g^2 = \frac{\left(\frac{\Delta P}{L}\right)_{TP}}{\left(\frac{\Delta P}{L}\right)_g} \quad (2.3)$$

When the flow multiplier for the phase is determined, the frictional pressure of two-phase eventually drops and can also be calculated by using Eq. (2.2) or (2.3). Lockhart and Martinelli (1949) additionally demonstrated that the liquid fraction, α_l , along with the void fraction, α_g can also be correlated to the Martinelli parameter, X . However, the overall design of the equations was done to predict a drop in two-phase pressure and that only a graphical correlation was given.

Additionally, Taylor (1961) conducted experiments to examine plug flow, primarily film thickness or fluid deposition at the tube wall. The fluids that were used consisted of glycerin with a strong sucrose solution (i.e. golden syrup) which was further diluted with distilled water to make the viscosity 28 poise at 20°C. Glass tubes having a 2 mm and 3 mm internal diameters and lengths of approximately 1.22 m were used for the testing sections. A gas bubble was then released into the test section and the total amount of film that was left after the bubble was then measured.

The results of Taylor's (1961) experiments were graphically presented by plotting the parameter, m (liquid that was left in the tube) against the capillary number. The experiments were conducted over a much broader range of the capillary number, $0 < Ca < 2.0$. It was concluded that when the capillary number gradually increases the liquid film also increases. This relationship is not linear. At relatively higher values of the capillary number (i.e. $Ca > 0.56$) the parameter m would eventually reach a limiting value ($m \approx 0.5$). After Taylor's (1961) study, various other researchers began to refer to segmented gas-liquid flow as Taylor plug flow. One of the most important characteristics identified by Taylor (1961) was the presence of circulation pair zones, within the liquid plugs. Additionally, these zones were caused by the presence of either liquid/gas or liquid/liquid interfaces. These circulations affected the overall flow in a manner that promotes the radial transport of both heat and mass, as well as boundary layer renewal, mainly due to the fresh fluid that was being transported to the liquid plug's leading edge.

Oliver and Wright (1964) studied a series of different measurements for investigating the overall effect of plug flow on both heat transfer and friction in laminar flow. They concluded that the internal circulation significantly increases the heat transfer coefficient and, therefore, Graetz-Leveque theory and Shah and London (1978) cannot be applied to plug flow. Furthermore, the experiments consisted of both single and two-phase flow in 0.25 inch test sections of varying lengths (3 to 4 feet). Additionally, the liquids that were used in this experiment were 56.5% glycerol, 88% glycerol, 0.75% sodium carboxymethylcellulose (SCMC), 1.5% SCMC, and 0.5% polyox, in water and 2% of celacol solution. The gas was air.

The experimental results were represented graphically with Nusselt number and Graetz number, as well as the ratio of two-phase flow to single phase flow of Nusselt number and void fraction. Lastly, Oliver and Wright (1964) stated that the overall effect of void fraction was independent of the plug length, however, circulation effects are highest with plugs. A simplified model for a two-phase plug flow heat transfer coefficient was based on the experimental data. A modification of the Graetz-Leveque model was later developed:

$$Nu_{TP} = Nu_{SP} \left(\frac{1.20}{R_L^{0.36}} - \frac{0.20}{R_L} \right) \quad (2.4)$$

Where Nu_{TP} is two-phase Nusselt number, Nu_{SP} is single-phase Nusselt number and R_L is Liquid holdup.

Hughmark (1965) established a correlation mainly for estimating hold-up (void fraction) in the horizontal slug flow. He based this correlation on a relationship of bubble velocity and the liquid slug Reynolds number. Additionally, the bubble velocity during slug flow was reported by Hughmark (1965):

$$u_b = K_2 \left(\frac{Q_l + Q_g}{A} \right) \quad (2.5)$$

Where Q_l is flow rate for liquid phase, Q_g is flow rate for gas phase, A is cross section area and K_2 denotes a function of the liquid Reynolds number that remains constant at 0.22 when the Reynolds number is greater than 400,000, which is within the turbulent regime for the liquid phase. Additionally, Hughmark (1965) presented the liquid Reynolds number as:

$$Re_l = \left(\frac{Q_l + Q_g}{A} \right) \frac{\rho_l}{\mu_l} \quad (2.6)$$

Where Re_l is Reynolds number for liquid phase, ρ_l is density for liquid phase and μ_l is dynamic viscosity for liquid phase.

Hughmark (1965) also developed a much simpler model for slug flow heat transfer that was dependent on the momentum-heat transfer analogy for turbulent flow. The Graetz-Leveque equation used for laminar flow. The simplified model is:

$$\frac{h_{TP} D \sqrt{Re_l}}{K_l} = 1.75 \left(\frac{Q_l C_p}{R_L K_l L} \right)^{\frac{1}{3}} \left(\frac{\mu}{\mu_l} \right)^{0.14} \quad (2.7)$$

Where D is diameter, h_{TP} is heat transfer coefficient for two-phase, K_l is thermal conductivity, C_p is specific heat and L is channel length.

Hughmark (1965) also compared (Eq. (2.7)) with experimental data from Oliver and Wright (1964). The average absolute deviation the experimental data model is approximetly 8.4%.

Chisholm (1967) established an equation to predict drop in two-phase frictional pressure:

$$\phi_l^2 = 1 + \frac{C}{X} + \frac{1}{X^2} \quad (2.8)$$

Where ϕ_l is liquid two-phase flow multiplier, X is Lockhart-Martinelli and C is Chisholm constant.

Equation (2.8) relates the two-phase multiplier for liquid to the Martinelli parameter along, as well as mass quality. The Constant, C , is based on different types of flow, summarized in Table 2.1.

Table 2.1: Values of Chisholm Constant

Turbulent – Turbulent Flow	$C = 20$
Laminar – Turbulent Flow	$C = 12$
Turbulent – Laminar Flow	$C = 10$
Laminar – Laminar Flow	$C = 5$

Oliver Hoon (1968) tested isothermal flow of both Newtonian and non-Newtonian pseudoplastic fluids in slug flow and concluded that the circulation or streamline deflection is present within the liquid slugs, and is dependent on the thickness of the

liquid film. Both slug flow and annular flow were studied in a 0.25 inch glass testing section. To measure the void fraction, quick-close valves were adjusted both before and after the test section. The quick-close valves were closed simultaneously and the trapped liquid was drained and then measured. A camera was mounted on a movable platform to photograph the slugs. Graphite particles were introduced as tracer particles. Oliver and Hoon (1968) also determined that the entire streamline pattern in Newtonian slug flow was characterized by circulation and streamline deflections were observed only with non-Newtonian slug flow. The experimental data was compared to Lockhart and Martinelli's (1968) plots and agreed well for Newtonian fluids, however, non-Newtonian were far below the calculated values. Oliver and Hoon (1968) plotted the results of the experiments by Graetz number against the Nusselt number:

$$Gz = \frac{\pi}{4} Re_{TP} Pr \frac{D}{L} \quad (2.9)$$

$$Re_{TP} = \left(\frac{Q_l + Q_g}{A} \right) \frac{D \rho_l}{\mu_l} \quad (2.10)$$

Where Gz is Graetz number, Re_{TP} is two-phase of Reynolds number, Pr is Prandtl number and ρ_l is density for liquid phase.

Horvath et al. (1973) conducted experiments to measure the radial transport in homogenous flow, as well as two-phase slug flow. They used an opened tubular, heterogeneous enzyme reactor, with 60 cm length and 2.32 mm internal diameter. The substrate solution was working fluid. The length to diameter ratio (L/D) of this entire setup was 260. Experiments for homogenous flow were conducted for measuring the radial mass transport ratio to substrate solution. An average Nusselt number for single phase flow was calculated with Eq. (2.11). The logarithmic mean concentration C_{ln} was calculated with Eq. (2.12)

$$J = \overline{Nu} D \pi L C_{ln} \quad (2.11)$$

$$C_{ln} = \frac{(C_i - C_{w,o}) - (C_o - C_{w,o})}{\ln \left(\frac{C_i - C_{w,i}}{C_o - C_{w,o}} \right)} \quad (2.12)$$

Horvath et al. (1973) then experimented with two-phase plug flow and again measured the entire radial mass transport. The average Nusselt number for two-phase plug flow was calculated by using an altered version of Eq. (2.11) :

$$J = \overline{Nu} D \pi L (1 - \varepsilon) c_{ln} \quad (2.13)$$

The new variable, ε , introduced in Eq. (2.13) represents the void fraction (typically expressed as α_g in a two-phase). It was determined that when radial transport in plug flow is compared to single phase flow, the Nusselt number increases significantly. Horvath et al. (1973) also conducted experiments on homogenous and two-phase slug flow in case of a coiled reactor. The rate of reaction and average Nusselt number was calculated. The Nusselt number is dependent on the ratio of tube diameter to coiled diameter:

$$R^* = \frac{D_t}{D_c} \quad (2.14)$$

Where D_t , D_c and R^* represent the tube diameter, coil diameter, and coiled aspect ratio, respectively.

Horvath et al. (1973) determined for low Reynolds numbers and low void fractions, the coiling could produce 80% to 100% increase the average Nusselt number. The experimental data was presented in a plot of average Nusselt number and dimensionless plug length, for both coiled and non-coiled experiments.

Vrentas et al. (1978) studied characteristics associated with a plug flow field with solid spheres in a liquid tube. The experimental study was one of the first published studies on solid-liquid slug flow. Furthermore, Vrentas et al. (1978) showed that an increase in pressure drop across the entire tube in liquid slugs of every size also resulted in a highly elevated power requirement. Hence, both liquid film thickness and slug length should be selected to optimize the entire system of solid-liquid slug flow. Provisions for recycling and maintenance of the spheres is not factor in gas-liquid systems.

Different theoretical assumptions were made by Vrentas et al (1978) to ensure the analysis of solid-liquid slug flow was comparable to calculations on velocity and temperature fields for cylindrical cavities with a uniform translating wall. The Nusselt number was defined for an ideal heat exchanger as:

$$Nu = \frac{(h_a)_l D}{K} = \frac{Pe T_a r}{L(2 - T_a)} \quad (2.15)$$

Where J is the overall rate of reaction, \overline{Nu} is average Nusselt number, c_{ln} is logarithmic mean concentration, T_a represents the dimensionless average temperature of the fluid. Vrentas et al. (1978) employed a horizontal heat exchanger with a gear pump for

different experiments. The ratio of length to diameter (L/D) was 128. Dow corning silicone oil was the working fluid. Two grades, 100 cSt and 1000 cSt, were selected. Stainless steel spheres were introduced on consistent intervals. The spheres and fluid flowed in a 0.95 cm ID tube and less than a 0.0025 cm clearance was present between the spheres and tube wall. A reciprocating piston was transferred the spheres between the exit and entrance of the heat exchanger. Freon TF vapor ($CCl_2F-CClF_2$) maintained a steady wall temperature while it condensed. The fluid's exit temperature was not reliable when the experimental data was collected; thus, the heat transfer coefficient that was reported by Vrentas et al. (1978) was based on heat flows that were deduced from measured condensation rates.

Vrentas et al. (1978) represented their experimental data graphically by plotting the Peclet number versus Nusselt number for a range of different dimensionless plug lengths, in the form:

$$Nu = 1.62 \left(Pe \frac{D}{L} \right)^{\frac{1}{3}} \quad (2.16)$$

Muzychka and Yovanovich (2004) established a generalized model to the heat transfer coefficient in the combined region of entry of various non-circular ducts. The model was created by a combination of the solution with a model developed initially for Graetz flow. The model developed for Graetz flow was developed by a combination of a model that was designed for fully developed flow with Leveque approximation. The flow model is:

$$Nu_{\sqrt{A}} = c_1 \left(\frac{f Re_{\sqrt{A}}}{8\sqrt{\pi} \varepsilon \gamma} \right) \quad (2.17)$$

Where f is fanning friction factor, ε is aspect ratio and γ is shape factor.

Where $c_1 = 3.24$ for uniform wall temperature (UWT) and $c_1 = 3.86$ for uniform wall flux. The γ parameter is based on channel geometry, with the upper and lower bounds are fixed at 1/10 and 3/10, respectively. A Leveque approximation for a thermal boundary layer was developed near wall and the velocity profile is linear:

$$Nu_{\zeta} = c_2 c_3 \left(\frac{f Re_{\zeta}}{z^*} \right)^{\frac{1}{3}} \quad (2.18)$$

Where c_2 is one for various local conditions and is 3/2 for average conditions. The ζ variable represents the dimensionless parameters that are dependent on specific arbitrary length scales, and c_3 is approximately 0.427 for different UWT conditions and 0.517 for UWF conditions. Muzychka and Yovanovich (2004) combined Eqs. (2.17) and (2.18) by employing an asymptotic correlation method introduced by Churchill and Usagi (1972). The model represents the Graetz flow:

$$\text{Nu}_{\sqrt{A}} = \left[\left(c_2 c_3 \left(\frac{f \text{Re}_{\sqrt{A}}}{z^*} \right)^{\frac{1}{3}} \right)^5 + \left(c_1 \left(\frac{f \text{Re}_{\sqrt{A}}}{8\sqrt{\pi\epsilon\gamma}} \right) \right)^5 \right]^{\frac{1}{5}} \quad (2.19)$$

Values for various constants in Eq. (2.19) are summarized a table presented by Muzychka and Yovanovich (2004). The generalized model to predict a heat transfer coefficient for a combined entry region was later established by combining Eq. (2.19) with a flat plate solution. Hence, by applying an asymptotic correlation a general model was developed:

$$\text{Nu}_{\sqrt{A}}(z^*) = \left[\left(\frac{c_4 f(\text{Pe})}{\sqrt{z^*}} \right)^m + \left\{ \left(c_2 c_3 \left(\frac{f \text{Re}_{\sqrt{A}}}{z^*} \right)^{\frac{1}{3}} \right)^5 + \left(c_1 \left(\frac{f \text{Re}_{\sqrt{A}}}{8\sqrt{\pi\epsilon\gamma}} \right) \right)^5 \right\}^{\frac{m}{5}} \right]^{\frac{1}{m}} \quad (2.20)$$

The parameter m in Eq. (2.20) is a function of the Prandtl number:

$$m = 2.27 + 1.65 \text{Pr}^{\frac{1}{3}} \quad (2.21)$$

The generalized model is valid for $0.1 < \text{Pr} < \infty$, $0 < z^* < \infty$, uniform wall temperature and uniform wall flux, as well as for local and average Nusselt numbers. Muzychka and Yovanovich (2004) made a comparison of the model to available data found that the model clearly agreed within $\pm 15\%$ for the majority of non-circular ducts.

Kreutzer et al. (2005) wanted to established a pressure drop model for segmented flow that could be used in capillaries, with considering both the plug and bubble length. The plug length is determined with data from experimental pressure drop data. Experiments were conducted with the capillary tube having an internal diameter of 2.3 mm. An inlet was constructed a tapered channel as well as a hypodermic needle, allowing both the liquid plug and bubble length to vary. The segmented flows consisted of air-decane, air-water, and air-tetradecane were examined. Gas and liquid superficial velocities varied

from 0.04 m/s to 0.3 m/s. Kreutzer et al. (2005) also found experimentally and numerically that for plug flow with $Re \gg 1$, extra pressure terms can use the capillary number to Reynolds number ratio (Ca/Re). The model is represented as:

$$f = \frac{16}{Re} \left(1 + 0.17 \frac{1}{L_s^*} \left(\frac{Ca}{Re} \right)^{0.33} \right) \quad (2.22)$$

Kreutze et al. (2005) numerically modeled plug flow by employing the CFD code FIDAP. Comparing numerical and experimental data, a correlation was developed by replacing the value 0.17 in Eq. (2.22) by 0.07. The difference between experimental and numerical data was not attributed to experimental error and was explained in terms of the Marangoni effect caused by impurities in the experimental fluids. When Eq. (2.22) is used for modeling single phase flow, L_s^* approaches infinity. The model reduces to Hagen-Poiseuille flow for laminar flow:

$$f = \frac{16}{Re} \quad (2.23)$$

Lakehal et al. (2006) studied flow simulations of computational microfluidics to examine heat transfer in smaller tubes. The simulations were used the CMFD code TransAT^c that was developed at ASCOMP. Three flow patterns were studied, at different flow rates, in a 1 mm internal diameter pipe and included: slug flow, bubbly flow and bubbly-train slug. A uniform wall temperature was maintained and the effects of flow pattern on heat transfer were analyzed. The wall temperature was maintained at 340 K and the inflow temperature at 300 K.

The results obtained from Lakehal et al. (2006) show that the rate of heat removal in two-phase flow is much higher than single phase flow. A model for heat transfer in the two-phase slug flow is:

$$Nu \approx Nu_w + CPr_l^{0.4} Re_{Ls}^{\frac{4}{5}} \quad (2.24)$$

Where Nu_w represents the single phase Nusselt number, which is 3.67 for a uniform wall temperature and 4.36 for uniform wall flux condition. The variable C in Eq. (2.24) is the model constant with a value of 0.022. The model is valid for segmented flow in micro-scale devices with $L \approx 0$ mm and $Pr > 1$. Lakehal et al. (2006) described the model (Eq. (2.24)) as being a guideline for engineers for different designing purposes.

Yu et al. (2007) used experimental and numerical methods to examine a bubble shape, size formation mechanisms during segmented flow in micro-channels. Mechanisms were investigated for varied flow rates, mixer geometries, and capillary numbers. Yu et al. (2007) also examined two mixer geometries. Among these, one was typically a cross-shaped mixer with a channel that was perpendicular to one main channel and the other was a converging mixer and the liquid inlets were 45° to the main channel. All channels had a square cross-section, with a $125\ \mu\text{m}$ and $250\ \mu\text{m}$ side length. The fluids included air, sucrose solution (viscosity of 30 cP), glucose solution (viscosity of 60 cP), and a mineral oil (viscosity of around 75 cP). The simulations were conducted with the Lattice Boltzmann method (LBM). One of the biggest advantages of this method for two-phase flows is the main phase separation spontaneously took place in either the non-ideal fluid or between two specific immiscible fluid components and did not require interface tracking. The simulations were conducted 600 grid points, but to reduce simulation time, 300 grid points were used for the short channels. Yu et al. (2007) also presented experimental and LBM simulation results that were visually depicted as pictures for different combinations of flow rate and capillary number. The main combinations included $\text{Ca} = 0.007$ and $Q_g:Q_l = 1:1$, $\text{Ca} = 0.035$ and $Q_g:Q_l = 1:4$, and $\text{Ca} = 0.017$ with $Q_g:Q_l = 1:2$. The differences observed between the two mixer geometries were visually depicted. It was reported that the ratio of larger gas to liquid flow rate eventually leads to much longer gas bubbles. Maintaining the same ratio of flow rate while decreasing the capillary number implies that by changing fluids it could eventually yield a much longer gas bubble. The mixer geometry possessed effects on both bubble length and the spacing between bubbles. Converging channel geometry creates much longer liquid plugs between gas bubbles at $\text{Ca} = 0.035$ with $Q_g:Q_l = 1:4$, however, the oval bubble size was reported to be very similar in both the cases.

Mohseni and Baird (2007) later studied electro-wetting on dielectric (EWOD) as a driving force that can be used for a relatively new method to cool digitized heat transfer (DHT) micro devices. The EWOD is used to transport droplets of highly electrically and thermally conductive liquid metal alloys by applying an electric field normal to the entire direction of flow. The EWOD force is generated by lining the micro-channel both with the electrodes and sequentially firing to slug the leading edge continuously between the grounded electrodes. Mohseni and Baird (2007) also stated that this is one

of the best ways of generating two-phase segment flow of different liquid metal alloys and can lead to orders of higher magnitudes of thermal conductivities when compared to non-metallic liquids, including water and oils. The liquid metal alloy for the Galinstan was suggested to be the best candidate for a EWOD micro-cooling device as it was inexpensive, non-toxic, readily available, and is 65 times less thermal resistant than water. Mohseni and Baird (2007) derived simplified equations for various EWOD applications:

$$\bar{u}_{drop} = \frac{cV^2}{24\mu} \frac{H}{L} \quad (2.25)$$

Where \bar{u}_{drop} is average bulk velocity of the experimented droplet, c is capacitance per unit area, V is voltage, H is for height of the channel and L is channel length. The simple expressions for different characteristics of heat transfer for both uniform wall temperature and uniform wall flux conditions were also presented. For UWT conditions, the expression for heat transfer is:

$$q = \rho_l n V H W c (T_w - T_i) \quad (2.26)$$

Where n denotes the droplet ratio, W is channel width, and ρ_l is density for liquid metal alloys. In UWF conditions, an additional expression for the outlet temperature is:

$$T_o = \frac{qW}{\rho_l n V H W c} + T_i \quad (2.27)$$

Awad and Muzychka (2007) established a simpler expression for both the upper and lower bounds for the frictional pressure gradient in two-phase in both the mini-channels as well as the micro-channels. For the lower bounds, which were typically based on the Ali et al. (1993) correlation derived for laminar-laminar flow, the following Eq was developed (2.28):

$$\left(\frac{dp}{dz} \right)_{f,lower} = \frac{32G(1-x)\mu_l}{D^2\rho_l} \left[1 + \left(\frac{x}{1-x} \right) \left(\frac{\rho_l}{\rho_g} \right) \left(\frac{\mu_g}{\mu_l} \right) \right] \quad (2.28)$$

The upper bound was based on the Chisholm correlation derived for laminar-laminar flow:

$$\left(\frac{dp}{dz} \right)_{f,upper} = \frac{32G(1-x)\mu_l}{D^2\rho_l} \left[1 + 5 \left(\frac{x}{1-x} \right)^{0.5} \left(\frac{\rho_l}{\rho_g} \right)^{0.5} \left(\frac{\mu_g}{\mu_l} \right)^{0.5} + \left(\frac{x}{1+x} \right) \left(\frac{\rho_l}{\rho_g} \right) \left(\frac{\mu_g}{\mu_l} \right) \right] \quad (2.29)$$

Awad and Muzychka (2007) also developed an average or mean bound that was based on the arithmetic mean of both the lower and upper bounds

$$\left(\frac{dp}{dz}\right)_{f,ave} = \frac{32G(1-x)\mu_1}{D^2\rho_1} \left[1 + 2.5 \left(\frac{x}{1+x}\right)^{0.5} \left(\frac{\rho_1}{\rho_g}\right)^{0.5} \left(\frac{\mu_g}{\mu_1}\right)^{0.5} + \left(\frac{x}{1-x}\right) \left(\frac{\rho_1}{\rho_g}\right) \left(\frac{\mu_g}{\mu_1}\right) \right] \quad (2.30)$$

The mean model (Eq. (2.30)) is equivalent to the Chisholm correlation, with $C = 2.5$. Fries et al. (2008) studied segmented flow in a rectangular micro-channel with laser induced fluorescence (LIF) as well as confocal laser scanning microscopy (LSM). The microfluidic channel was 2 m in length and had a height and width of $200 \pm 2 \mu\text{m}$. The fluids included water, ethanol, and glycerol in their respective aqueous solutions at various concentrations, nitrogen was also used. Fries et al. (2008) changed the flow rates from around 20 - 60 $\mu\text{L}/\text{min}$ a liquid phase to 30 - 100 $\mu\text{L}/\text{min}$ mainly for the gaseous phase. The superficial velocities for all these flow rates were 0.008 – 0.025 m/s in the liquid phase and 0.013 – 0.042 m/s for the gaseous phase. The liquid plug length, pressure drop, gas bubble length, and film thickness over the range of superficial velocities were comprehensively examined.

Fries et al. (2008) lastly reported that during analysis of the liquid plug lengths, a full channel length was observed as having a constant plug length, excluding ethanol. It was also found that the plug length increases with an increasing superficial liquid velocity at a continuous gas flow rate. When the length of the gas bubble was examined, the bubbles elongated because of the pressure drop. The length of the gas bubble was graphically plotted versus the length of the reactor for ethanol-nitrogen. It was found that the length of the gas bubble was dependent on the pressure and for a constant superficial gas velocity of 0.042 m/s, an increase was seen in the overall liquid flow rate, which resulted in a decrease in the length of the gas bubble.

The Kreutzer et al. (2005) model initially under-predicted the obtained data. The main reason was Kreutzer et al. (2005) initially examined circular channels, but Fries et al. (2008) worked on rectangular channels. Fries et al. (2008) compared the pressure drop data to three already existing models that were based on the theory of Lockhart and Martinelli (1949). The three models were the Chisholm (1967) model, Lee and Lee (2001) model, and Mishima (1996) model. It was found that good agreements were made with models that were based on micro-channels, but models that were developed for a macro-scale over-predicted the pressure drop measurements.

Fries et al. (2008) then measured the film thickness with LSM. The results for these film thickness measurements were graphically compared with correlations that were derived from past literature and included those proposed by Kreutzer et al (2005), Bretherton (1961) and Kolb and Cerro (1991). It was reported that for a higher capillary number, the gas bubbles would elongate and the related measurements became more comparable to past literature. For much smaller capillary numbers ($Ca < 0.001$), the corner film thickness was almost independent from the Capillary number. It was confirmed that if $Ca < 0.01$, no significant changes could be observed in the film thickness that reduced the capillary number. This also agreed with the initial measurements of Kolb and Cerro (1991).

Narayanan and Lakehal (2008) analyzed both the Nusselt number and pressure drop for bubble and plug flow via simulations that were conducted with a CMFD code TransAT^c, which was established at the ASCOMP. The simulations were performed under axisymmetric conditions for single and two-phase flows with zero-gravity down-flow and up-flow configurations. Furthermore, the simulations were compared to experimental data of Chen et al. (2002).

Narayanan and Lakehal (2008) reported that for overall bubbly flow, an average Nusselt number of 10.7 was obtained for all three cases with different orientations with respect to gravity. For plug flows, an average Nusselt number of 15 was obtained, but a discernible trend was present with respect to gravity orientation. In addition, the down-flow case had a 4% higher average Nusselt number when compared to the case of zero-gravity. The results were graphically presented by plotting the local Nusselt number with the dimensionless channel length. For overall bubbly flow, the local Nusselt number changed smoothly with a maximum at the gas bubble center, where the liquid layer was squeezed. For overall plug flow, the local Nusselt number's maximum value occurred at the rear end, where the gap between the interfaces and wall was very small. Orientation with respect to gravity is also played an important role in shifting the location of breakup upstream for up-flow and resulted in a much larger breakup frequency. Nusselt numbers were obtained of similar magnitudes as those from Monde and Mitsutake (1995) and Ua-Arayaporn et al. (2005). The average Nusselt numbers from the experiments of Narayanan and Lakehal's (2008) simulations transported 3 to

4 times more heat than single phase flows. Narayanan and Lakehal (2008) also proposed a simplified model for Nusselt number that can be used for practical applications:

$$Nu \approx Nu_w CPr^{0.4} Pe_{LS}^{\frac{4}{5}} \quad (2.31)$$

Where Nu_w is the Nusselt number for completely developed single phase flow, with a value of 3.67 for uniform wall temperature and 4.36 for uniform wall flux. The constant C is 0.022.

Muzychka and Awad (2008) presented three different methods for two-phase flow modeling in both mini-channels and micro-channels. The first method was a series of effective property models that were used for homogenous flows and consisted of various models for density, viscosity, fanning friction factor and Reynolds number. The second method was a new asymptotic model that was used for two-phase frictional multipliers. It was developed by using an initial asymptotic analysis method introduced by Churchill and Usagi (1972). The asymptotic model is:

$$\phi_l^2 = \left[1 + \left(\frac{1}{X^2} \right)^P \right]^{\frac{1}{P}} \quad (2.32)$$

$$\phi_g^2 = \left[1 + (X^2)^P \right]^{\frac{1}{P}} \quad (2.33)$$

Where P has a value minimizing the root mean square (RMS) error between the model predictions and the published data. The third method presented by Muzychka and Awad (2008) to model two-phase flow in mini-channels and micro-channels, was a rational bounds model used for the two-phase frictional pressure gradient. The model was established by Awad and Muzychka (2007) and was previously detailed in this literature review. The effective and efficient property models for viscosity were compared to published data of Ungar and Cornwell (1992), Tran et al. (2000), Cavallini et al. (2005), and Field and Hrujak (2007). The effective viscosity model that best predicted the experimental data was the Maxwell Eucken II model, which had the lowest RMS error of only (16.7%):

$$\mu_m = \mu_g \frac{2\mu_g + \mu_l - 2(\mu_g - \mu_l)(1-x)}{2\mu_g + \mu_l + (\mu_g - \mu_l)(1-x)} \quad (2.34)$$

Both the asymptotic models and the mean bounds model developed by Muzychka and Awad (2008) (Eqs. (2.32), (2.33) and (2.30)) were compared to published data by plotting two-phase flow multipliers against the Martinelli parameter X .

Muzychka et al. (2009) in the following years reviewed the problems of classic Graetz flow, as well as heat transfer characteristics. Two different models were developed using the asymptotic characteristics associated with plug and Poiseuille flows that could be used for constant wall boundary conditions. The models were created using the asymptotic correlation method of Churchill-Usagi for developing thermal Graetz flow. For the slug flow, a dimensionless heat transfer model was given by Eq. (2.35). The Poiseuille flow model mainly for dimensionless heat transfer was given by Eq. (2.36):

$$q^* = \left[\left(\frac{1.128}{\sqrt{L^*}} \right)^2 + \left(\frac{1}{4L^*} \right)^2 \right]^{\frac{1}{2}} \quad (2.35)$$

$$q^* = \left[\left(\frac{1.614}{\sqrt{L^{*\frac{1}{3}}}} \right)^{\frac{3}{2}} + \left(\frac{1}{4L^*} \right)^{\frac{3}{2}} \right]^{\frac{-2}{3}} \quad (2.36)$$

In both Eqs. (2.35) and (2.36), q^* represents dimensionless heat transfer and L^* the dimensionless length. Muzychka et al. (2009) used Eqs. (2.35) and (2.36), as well as heat transfer theory to prove that the best and only way in which thermal enhancement could be achieved is if a desired change is made in the local velocity profile through segmentation. It showed that the circulations in liquid plugs were the only mechanism that causes heat transfer enhancement:

$$q^* = \frac{q/(\alpha_1 A) D_h}{K(T_w - T_i)} \quad (2.37)$$

$$L^* = \frac{(L_s/D)}{Pe_D} \quad (2.38)$$

Muzychka et al. (2009) compared the Eqs. (2.37) and (2.38) to the already published data. A comparison was graphically developed by plotting dimensionless heat transfer against the dimensionless length. The data was initially produced by Oliver and Young Hoom (1968), Horvath (1973), Narayanan and Lakehal (2008) and Prothero and Burton (1961). The plots indicated that a much better scaling of the dimensionless data was

obtained whenever the true wetted surface area and plug lengths were considered. Muzychka et al. (2009) proposed a definite model to predict heat transfer for segmented flow of laminar gas-liquid on wetted surface areas:

$$q^* = \left[\left(\frac{1.614}{\sqrt{L_s^*}} \right)^{\frac{3}{2}} + \left(\frac{1}{4L_s^*} \right)^{\frac{3}{2}} \right]^{-\frac{2}{3}} \quad (2.39)$$

Where L_s^* denotes the dimensionless plug length:

$$L_s^* = \frac{\pi \alpha_l L_s K}{4 \dot{m}_l c_p} \quad (2.40)$$

Walsh et al. (2009) investigated segmented flow under uniform wall heat flux conditions. They conducted several experiments to test segmented flow, in a heated section of a different stainless steel tube (2 m in length and 1.5 mm internal diameter). The temperature measurements were taken with four k-type thermocouples and a FLIR systems (IR) camera. Walsh et al. (2009) also presented a plot of time that averaged the mean wall temperature rise with the overall distance from the tube's entrance, for single phase flow and three segmented flows with ratios of slug length to a diameter of 1.6, 5.7, and 14.3. The generalized trends for shorter slugs provided augmented heat transfer over the entire testing section. Moderate length slugs could also result in the degradation of overall heat transfer rates within entrance regions, and improve heat transfer in fully developed regions. Longer length slugs could result in degrading heat transfer rates throughout the entire system. The study was on heat transfer rates for segmented flows with entrance region details.

Walsh et al. (2009) presented a plot for the local Nusselt number that was normalized by the liquid wetted region against the inverse of the Graetz parameter Gz . The final plot showed the slug flow could eventually degrade heat transfer within the entire entrance region, however, it would typically augment heat transfer within the completely developed region. Walsh et al. (2009) established a model for predicting the local Nusselt number in segmented flows that already consisted of various deriving expressions for the developing and completely developed regions. The entrance region asymptote was derived by taking exact mean values between both plug and Poiseuille flow limits:

$$\text{Nu}_{x(s,\text{Ent})} = \text{Nu}_{x(p,\text{Ent})} + \frac{D}{L_s} \left[\text{Nu}_{(pl,\text{Ent})} - \text{Nu}_{(p,\text{Ent})} \right] \quad (2.41)$$

A completely developed flow limit was derived by adding the enhancement because of slug flow to the Poiseuille flow limit:

$$\text{Nu}_{x(s,\text{Dev})} = \text{Nu}_{x(p,\text{Dev})} + 31.5 \left(\frac{D}{L_s} \right)^{\frac{1}{2}} \quad (2.42)$$

Walsh et al. (2009) combined two different asymptotic limits in Eq. (2.41) and (2.42) by utilizing the asymptotic correlation method of Churchill-Usagi. The model developed is:

$$\text{Nu}_{x(s)} = \left\{ \left(\text{Nu}_{x(s,\text{Ent})} \right)^{\frac{1}{n}} + \left(\text{Nu}_{x(s,\text{Dev})} \right)^{\frac{1}{n}} \right\}^n \quad (2.43)$$

Where the parameter n had a value of 10 and the model was in excellent agreement experimental data. Walsh et al.'s (2009) findings help in providing a much greater understanding of the overall physics associated with segmented flow.

Chapter 3

Methodology

3.1 Introduction

This chapter presents the mechanism of heat transfer enhancement and heat transfer coefficients in internal flow. The pressure drop that occurs in the pipe and basic relations in two-phase flow are illustrated. The system configuration and apparatus is used to set up the experiment are presented as well.

3.2 Mechanism of Heat Transfer Enhancement

The factors that enhance heat transfer rate in the two-phase flows of non-boiling are: internal circulations present in the slugs that increase radial heat transfer rate, and an increased slug velocity. Muzychka et al. (2011) demonstrated the first one to be valid, and argued that by increasing the main convective heat transfer coefficient, (denoted as h), greater heat transfer cannot be achieved due to the segmented flow having a considerably smaller contact area than the single phase flow. Fig. 3.1 illustrates the internal circulations that are caused by the shear forces in moving plugs.

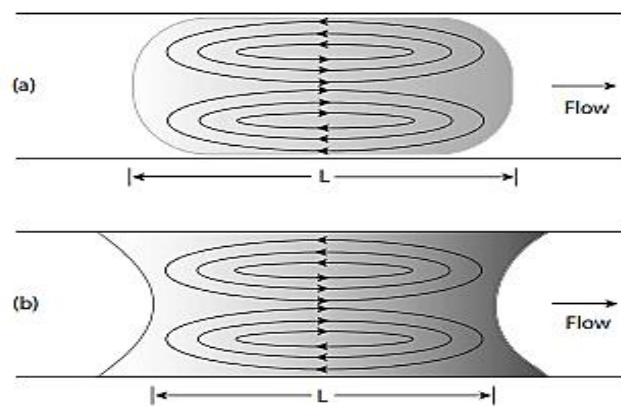


Figure 3.1: Internal Liquid Plug Circulation (a) Hydrophobic Surface (b) Hydrophilic Surface (Muzychka, 2011)

The internal circulations caused inside liquid slugs circulate liquid from the center to the upper wall, where heat transfer can occur. This provides an efficient renewal mechanism to the thermal boundary layer and causes an increased heat transfer rate. Diffusion, however, is not important to the entire process; hence, the boundary layer

continues to grow until and unless the circulation eye receives the generated heat. Examples of uniformly segmented two-phase flows are shown in Fig. 3.2

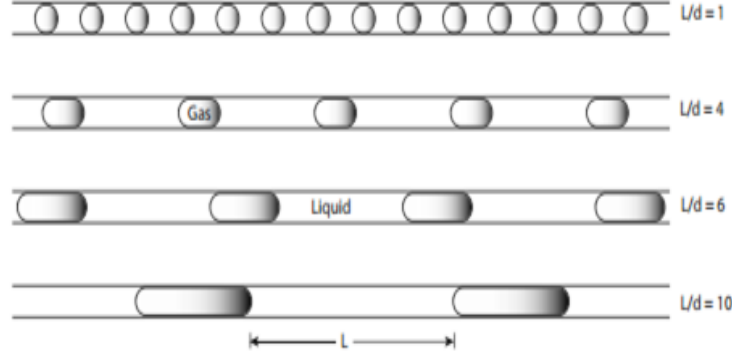


Figure 3.2: Gas-Liquid Slug Flows for Different Slug Lengths (Muzychka, 2011)

3.3 Heat Transfer Coefficients in Internal Flow

Similar to both externally forced and natural convection, the coefficient of heat transfer can also be defined for internal flow. Unlike various external flows in which the temperature of free stream remains constant (T_∞), the main temperature difference between both the moving stream and wall does not stay constant over the entire length of either the duct or channel. In duct or channel flow, the temperature difference between walls and fluid can be characterized in several ways, such as

- Wall to Bulk Mean, $T_w - T_m$
- Wall to inlet, $T_w - T_i$
- Mean wall to inlet, $\bar{T}_w - T_i$

The most accurate characterization should depend on the application. In single fluid system like heat sinks, one of the best and simplest approaches is using the temperature difference of wall to inlet. However, in two fluid systems, such as heat exchangers, one of the better choices is employing the temperature difference of wall to bulk. The most commonly used reference temperature for defining the coefficient of heat transfer in internal flow can traditionally be explained in the context of bulk temperature:

$$T_m = \frac{\iint \rho c_p w T dA}{\iint \rho c_p w dA} \quad (3.1)$$

However, for both constant specific heat as well as density, the equation takes the following form:

$$T_m = \frac{1}{wA} \iint wT dA \quad (3.2)$$

Total heat flux q_z , can be directly related to the coefficient of local heat transfer (denoted by h_z) by of a definite characteristic temperature difference existing in the overall local flow:

$$q_z = h_z (T_w - T_m) \quad (3.3)$$

Where $T_w - T_m$ is used for the temperature difference between the local wall and bulk. In cases where a duct has a prescribed wall has a constant temperature, the overall heat flux differs because of the changes occurring in the entire bulk temperature. In cases where the duct has a prescribed wall flux remaining constant, the overall wall temperature also varies. Hence, in these different applications, the following equation applies:

$$q_w = h_z (T_{w,z} - T_m) \quad (3.4)$$

In integrated analysis, employing the mean wall temperature in flux-related problems and mean flux for specified temperature. One can also define a dimensionless local and mean heat transfer coefficient or Nusselt number for constant wall temperature and the constant heat flux of wall. The overall heat transfer rate is non-dimensionalized with the Nusselt number and can be defined as:

$$Nu_\ell = \frac{q\ell}{K(T_w - T_m)} = \frac{h\ell}{K} \quad (3.5)$$

Where ℓ is used to represent a length scale that is related to the entire duct geometry. The heat transfer coefficient is an important variable for heat transfer. Furthermore, it is also unfortunate that many overuse and misuse this highly significant parameter. The above equation shows a highly unnatural approach to non-dimensionalizing the associated heat flux, since the temperature scale of wall to bulk fails in naturally appearing in the main solution for either the temperature field or the heat flux. Both the local as well as averaged heat fluxes can be simply obtained in this particular manner. The temperature difference of wall to bulk undoubtedly holds a strong place in those problems that are involved with the heat exchangers; however, single fluid devices

including heat sinks and many other microfluidic devices where heat transfer typically occurs from a single fluid are not necessary.

3.3.1 Constant Wall Temperature ($T_w = \text{Constant}$)

When the entire wall of the duct is uniformly maintained to have a constant wall temperature T_w , the following equations can be derived based on the mean fluid temperature of wall to bulk:

$$\text{Nu}_\ell = \frac{q_z \ell}{K(T_w - T_m)} \quad (3.6)$$

$$\text{Nu}_\ell = \frac{q_z \ell}{K(T_w - T_i)} \quad (3.7)$$

This definition is useful in the entire boundary layer region, for developing asymptotic solutions. To calculate the Nusselt number, we integrate along the duct length:

$$\overline{\text{Nu}}_\ell = \frac{1}{L} \int_0^L \text{Nu}_\ell dz \quad (3.8)$$

It is often easier to employ heat exchanger theory for an isothermal wall to obtain the mean Nusselt number, defined in terms of temperature difference of wall to bulk:

$$\frac{T_m - T_i}{T_i - T_w} = 1 - \exp\left(-\frac{\bar{h}PL}{\dot{m}C_p}\right) \quad (3.9)$$

The left side of the equation can further be written in terms of significant dimensionless mean temperature of bulk:

$$\theta_m = \frac{T_m - T_i}{T_i - T_w} \quad (3.10)$$

Or

$$1 - \theta_m = 1 - \exp\left(-\frac{\bar{h}PL}{\dot{m}C_p}\right) \quad (3.11)$$

By introducing the thermal duct length, $L^* = \frac{L}{\ell Re_D h Pr}$, that is dimensionless and ℓ being an arbitrary length scale, we get:

$$\overline{\text{Nu}}_\ell = \frac{1}{(P_\ell/A)L^*} \ln\left(\frac{1}{\theta_m}\right) \quad (3.12)$$

If h is defined on the basis of temperature difference of wall to bulk fluid, then this requires the log mean of temperature difference:

$$\Delta T_{\ln} = \frac{(T_w - T_i) - (T_w - T_o)}{\ln \left(\frac{T_w - T_i}{T_w - T_o} \right)} \quad (3.13)$$

Where T_o represents the outlet bulk temperature:

$$Q = \bar{h} A \Delta T_{\ln} \quad (3.14)$$

The mean Nusselt number becomes equivalent to:

$$\overline{Nu}_\ell = \frac{\bar{q}\ell}{K \Delta T_{\ln}} \quad (3.15)$$

Where $\bar{q} = \frac{Q}{A}$ represents the average heat flux. For a Nusselt that is defined on the basis of the temperature difference of wall to inlet, we still use $(T_w - T_i)$, i.e.,

$$\overline{Nu}_\ell = \frac{\bar{q}\ell}{K(T_w - T_i)} \quad (3.16)$$

Equation (3.6) can be expressed dimensionlessly:

$$q^* = \frac{\bar{q}\ell}{K(T_w - T_i)} \quad (3.17)$$

and

$$q^* = \frac{A/(P\ell)}{L^*} \left[1 - \exp \left(- \frac{\overline{Nu}_\ell L^*}{A/(P\ell)} \right) \right] \quad (3.18)$$

Equation (3.18) can be used in different applications to calculate the overall heat transfer rate on the basis of wall to inlet temperature differences.

3.3.2 Constant Heat Flux ($q_w = \text{constant}$)

In many applications, especially when involving electric resistance heating, it might be more practical to employ a constant boundary condition for heat flux. By maintaining a constant flux at the wall, q_w , the Nusselt number can be defined as:

$$Nu_\ell = \frac{q_w \ell}{K(T_{w,z} - T_m)} \quad (3.19)$$

Or

$$Nu_\ell = \frac{q_w \ell}{K(T_{w,z} - T_i)} \quad (3.20)$$

In the thermal boundary region, using a uniform and constant heat flux, the local Nusselt number can be used to assume the wall to bulk fluid temperature increase and the entire wall temperature distribution:

$$T_{w,z} = T_m + \frac{qw\ell}{KNu_\ell} \quad (3.21)$$

Where T_m is found by a enthalpy balance:

$$T_m = T_i + \frac{q_w Pz}{\dot{m}C_p} = T_i + z^* \left(\frac{q_w/K}{A/P\ell^2} \right) \quad (3.22)$$

Where, by considering the overall expression mainly for the relationship with Nu the local wall or the wall to bulk temperature difference can be determined. In case of single fluid heat exchanger, the dimensionless wall temperature:

$$\Delta T_w = \frac{(T_{w,z} - T_i)K}{qw\ell} \quad (3.23)$$

3.4 Basic Relations in Two-Phase Flows

In this section, common equations to analyses the experimental data of two phase flows are presented:

3.4.1 Mass Flow Rate

Mass flow rate (\dot{m}) is the mass of a substance passing per unit of time. In the experiment, the two phases flow are water, glycol, and air. The mass flow of two phases is:

$$\dot{m}_{total} = \dot{m}_l + \dot{m}_g \quad (3.24)$$

Where \dot{m} is the total mass flow rate for water and gas, \dot{m}_l is the mass flow rate of liquid, and \dot{m}_g is for gas. The mass flow rate can also be defined as:

$$\dot{m}_{total} = \rho \dot{Q} = \rho UA \quad (3.25)$$

Where \dot{Q} is the volume flow rate, ρ is the mass density of the flowing fluid, U is denotes the flow velocity of various mass elements, and a denotes the cross-sectional vector area.

3.4.2 Mass Flux

The mass flux (G) is the rate of mass flow per unit area. Mass flux can be defined as:

$$G = \frac{\dot{m}}{A} = \frac{\rho U A}{A} = \rho U \quad (3.26)$$

The combined mass flux of two-phase flow can now be defined as:

$$G_{total} = G_l + G_g \quad (3.27)$$

3.4.3 Mass Fraction

The mass fraction (x) is the ratio of one fluids mass flow rate to the total mass flow rate of the entire mixture (m_{total}). The mass fraction can be defined as:

$$x = \frac{\dot{m}_l}{\dot{m}_{total}} = \frac{\dot{m}_l}{\dot{m}_l + \dot{m}_g} \quad (3.28)$$

Thus, when x is 0, only \dot{m}_g is present. However, when x equals 1, \dot{m}_l is present.

3.4.4 Void Fraction

The void fraction (α) is parameter for characterizing two-phase flow. It is important to determine several important parameters, including two-phase density and two-phase viscosity. It is also used in several models to predict flow pattern transitions, heat transfer, and pressure drop. There are three different expressions used for determining void fraction, shown below:

$$\alpha_{Chordal} = \frac{L_g}{L_g + L_l} \quad (3.29)$$

Where L_g is the length of air phase, and L_l is length of liquid phase. Also,

$$\alpha_{c-s} = \frac{A_g}{A_g + A_l} \quad (3.30)$$


Where A_g the cross-sectional area of the air is phase and A_l is the cross-sectional area of the channel in liquid phase. Also,

$$\alpha_{vol} = \frac{V_g}{V_g + V_l} \quad (3.31)$$

Where V_g is the volume of the channel with air and V_l is the channel volume with liquid.


Three cases for void fraction are presented in Fig. 3.3

1. Chordal Void Fraction



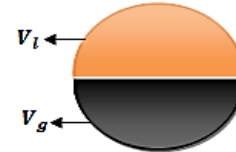
$$\alpha_{chordal} = \frac{L_g}{L_g + L_l}$$

2. Cross- Sectional Void Fraction



$$\alpha_{c-s} = \frac{A_g}{A_g + A_l}$$

3. Volumetric Void Fraction



$$\alpha_{vol} = \frac{V_g}{V_g + V_l}$$

Figure 3.3: Geometry of Void Fraction

The volume of fractions for each of phase is employed for finding the phase velocities:

$$u_1 = \frac{U_1}{1-\alpha} = \frac{\dot{Q}_1/A}{1-\alpha} = \frac{G_1}{\rho_1(1-\alpha)} \quad (3.32)$$

$$u_2 = \frac{U_2}{\alpha} = \frac{\dot{Q}/A}{\alpha} = \frac{G_2}{\alpha} \quad (3.33)$$

The definition for the slip ratio can be represented by:

$$S = \frac{u_2}{u_1} = \frac{\dot{Q}_2(1-\alpha)}{\dot{Q}_1\alpha} \quad (3.34)$$

The slip ratio considering both mass fluxes and mass quality is:

$$S = \frac{u_2}{u_1} = \frac{\rho_1 x (1-\alpha)}{\rho_2 (1-x)} \quad (3.35)$$

The expressions for the volume fraction as a function of slip ratio is:

$$\alpha = \frac{1}{1+S(\dot{Q}_1/\dot{Q}_2)} \quad (3.36)$$

$$\alpha = \frac{1}{1+S\left(\frac{1-x}{x}\right)\frac{\rho_2}{\rho_1}} \quad (3.37)$$

3.4.5 Volumetric Flux

The volumetric flux (represented by j) is the total rate of volume flowing across a unit area and the volumetric flux is:

$$j = \frac{\dot{Q}}{A} = \frac{UA}{A} = U \quad (3.38)$$

The total volumetric flux of both liquid and air becomes is:

$$j_{\text{total}} = \frac{\dot{Q}_l + \dot{Q}_g}{A} = U_l + U_g \quad (3.39)$$

The volumetric quality (β) is defined in a similar manner to that of the mass quality, however, it uses the specific component of volumetric flow rates instead of mass flow rates and can be represented numerically by:

$$\beta = \frac{\dot{Q}_g}{\dot{Q}_l + \dot{Q}_g} \quad (3.40)$$

3.5 Pressure Drop

The pressure drop for any fluid is caused by variation in potential energy and kinetic energy, as well as friction present on the walls of the flow channel. Two-phase pressure drops for flows inside tubes are the sum of three different contributions including the static pressure drop, ΔP_{static} , frictional pressure drop, $\Delta P_{\text{friction}}$, and momentum pressure drop, $\Delta P_{\text{momentum}}$:

$$\Delta P_{\text{total}} = \Delta P_{\text{friction}} + \Delta P_{\text{static}} + \Delta P_{\text{momentum}} \quad (3.41)$$

or

$$-\frac{dP}{dz} = \frac{P}{A} \tau_w + \rho_m g \sin(\theta) + G^2 \frac{d}{dz} \left(\frac{1}{\rho_m} \right) \quad (3.42)$$

Static pressure drop for a homogenous two-phase fluid is:

$$\Delta P_{\text{static}} = \rho_m g H \sin(\theta) \quad (3.43)$$

Where H shows vertical height, θ is angle with respect to horizontal position, g is gravitational force, and ρ_m is mean density of both phases. The mean density for both phases can be calculated by either void fraction, solid fraction or liquid fraction of the dispersed phase. The mean density of the two-phases (both liquid and air) is:

$$\rho_m = (1-\alpha)\rho_l + \alpha\rho_g \quad (3.44)$$

The mean density for liquid and air depends on the mass fraction:

$$\rho_m = \left[\frac{1-x}{\rho_l} + \frac{x}{\rho_g} \right]^{-1} \quad (3.45)$$

Where ρ_l is for density of liquid and ρ_g is density of air. The momentum pressure gradient per unit length of tube is:

$$\Delta P_{\text{momentum}} = G^2 \frac{d}{dz} \left(\frac{1}{\rho_m} \right) \quad (3.46)$$

The problematic term is the frictional pressure drop, which is expressed as an function two-phase (liquid and air) friction factor (f) and for steady flow a channel with a cross-sectional area expressed as:

$$\Delta P_{\text{friction}} = \frac{PL}{A} \tau_w = \frac{2f\rho_m U_m}{D_i} \quad (3.47)$$

Where L represents the length of the channel, and D_i represents the internal diameter of the tube. The friction factor can be expressed as:

$$f = \frac{0.079}{\text{Re}^{0.25}} \quad (3.48)$$

Where

$$\text{Re} = \frac{\rho_m U_m D_i}{\mu_m} \quad (3.49)$$

Where μ_m represents the total mixture viscosity for both phases. It has different formulas which are dependent on the application, i.e. liquid-liquid, gas-liquid and solid-liquid mixtures. Common formulas in gas-liquid are the Cicchitti, McAdams and the Dukler models.

- McAdams Model:

$$\mu_m = \left[\frac{1-x}{\mu_l} + \frac{x}{\mu_g} \right]^{-1} \quad (3.50)$$

- Cicchitti Model:

$$\mu_m = (1-x)\mu_l + x\mu_g \quad (3.51)$$

- Dukler Model:

$$\frac{\mu_m}{\rho_m} = \left[(1-x) \frac{\mu_l}{\rho_l} + x \frac{\mu_g}{\rho_g} \right] \quad (3.52)$$

For horizontal tube, no change is observed in static head, i.e. $\theta = 0$ and $H = 0$; hence, Δp_{static} is equal to zero. For adiabatic flow, if $x = \text{constant}$, then, $\Delta p_{momentum}$ is equal to zero. The two-phase pressure drop for a horizontal tube can be defined as:

$$\Delta P_{total} = \Delta P_{friction} = \frac{PL}{A} \tau_w = \frac{2f \rho_m U_m^2}{D_i} \quad (3.53)$$

Where $\sin(\theta)$ is equal to 1, suggesting the tube is present in a vertical position; hence, the drop in momentum pressure is the change in kinetic energy of flow and can be expressed as:

$$\Delta P_{momentum} = G_{total}^2 \left[\left(\frac{(1-x_o)^2}{\rho_l (1-\alpha_o)} + \frac{x_o^2}{\rho_g \alpha_o} \right) - \left(\frac{(1-x_i)^2}{\rho_l (1-\alpha_i)} + \frac{x_i^2}{\rho_g \alpha_i} \right) \right] \quad (3.54)$$

Where G_{total} is the total mass flux, both x_o and x_i represent the outlet and inlet of mass friction, and α_o and α_i represent the outlet and inlet of volume friction.

3.6 Dimensionless Parameters

Dimensionless numbers are commonly employed for placing two-phase flow data into efficient and convenient forms. These include Laplace, Reynolds, Capillary, Eötvös, Bond, Weber, Nusselt, Froude and Prandtl numbers.

3.6.1 Reynolds Number

Reynolds number (Re) is basically a dimensionless quantity for predicting similar flow patterns but in different fluid flow conditions. The Reynolds number is the total ratio of inertial forces to viscous forces and, is useful for quantifying the relative significance of these two forces. Reynolds number can be expressed as:

$$Re = \frac{\rho U D}{\mu} \quad (3.55)$$

Where U represents the velocity of the object relative to flowing fluid, D is diameter of the tube, μ is dynamic viscosity and ρ is fluid density.

3.6.2 Capillary Number

The capillary number (Ca) represents the relative effect of various viscous forces and the surface tension that acts across an interface between a liquid and gas, or between two immiscible liquids:

$$Ca = \frac{\mu_l U}{\sigma} \quad (3.56)$$

Where μ represents the dynamic viscosity of flowing liquid, U represents the characteristic velocity and σ represents either surface or interfacial tension between two different phases.

3.6.3 Eötvös Number

Eötvös number (Eo) is a dimensionless number used for characterizing the overall shape of bubbles and drops moving in a fluid. The Eötvös number can be expressed as:

$$Eo = \frac{\Delta \rho g L^2}{\sigma} = \frac{g L^2 (\rho_l - \rho_g)}{\sigma} \quad (3.57)$$

Where $\Delta \rho$ is the difference in density of two-phase flow ($\rho_l - \rho_g$), L represents the characteristic length, σ is the surface tension and g is gravity.

3.6.4 Bond Number

The Bond number is a measure of surface tension forces compared to body forces. A higher Bond number shows that the entire system is unaffected by surface tension effects and a lower number shows that surface tension greatly dominates. The Bond number can be expressed as:

$$Bo = \frac{\Delta \rho a L^2}{\sigma} = \frac{a L^2 (\rho_l - \rho_g)}{\sigma} = \frac{g L^2 (\rho_l - \rho_g)}{\sigma} \quad (3.58)$$

3.6.5 Laplace Number

The Laplace number (La) represents a ratio of surface tension to momentum-transport inside a fluid and can be represented by:

$$La = \sqrt{\frac{\sigma}{g L^2 (\rho_l - \rho_g)}} \quad (3.59)$$

Where $\Delta\rho$ represents the difference in density of two-phase flow ($\rho_l - \rho_g$), g represents gravitational force, L is the characteristic length, and σ is the surface tension.

3.6.6 Weber Number

The Weber number can be expressed as:

$$We = \frac{\rho U^2 L}{\sigma} \quad (3.60)$$

Where ρ is fluid density, U is fluid velocity, L represents the characteristic length, and σ represents surface tension.

3.6.7 Froude Number

The Froude number (Fr) represents the ratio of velocity to the gravitational wave velocity. The Froude number can be used to determine the resistance of a submerged object (partially) that moves through water, and also permits the comparison of various other objects of various sizes. The Froude number can be expressed as:

$$Fr = \frac{\rho U^2}{\rho g D} = \frac{U^2}{g D} \quad (3.61)$$

3.6.8 Prandtl Number

The Prandtl number (Pr) is the ratio of momentum diffusivity to thermal diffusivity:

$$Pr = \frac{\vartheta}{\alpha} = \frac{\mu C_p}{K} \quad (3.62)$$

Where

$$\alpha = \frac{K}{\rho C_p} \quad (3.63)$$

Where ϑ represents the kinematic viscosity, μ is dynamic viscosity, α is thermal diffusivity, k is thermal conductivity, c_p is specific heat, and ρ is density.

3.7 System Configuration

The system contains several different types of subsystems used for obtaining segmented two-phase plug flow. The system configuration is illustrated in Fig 3.4.

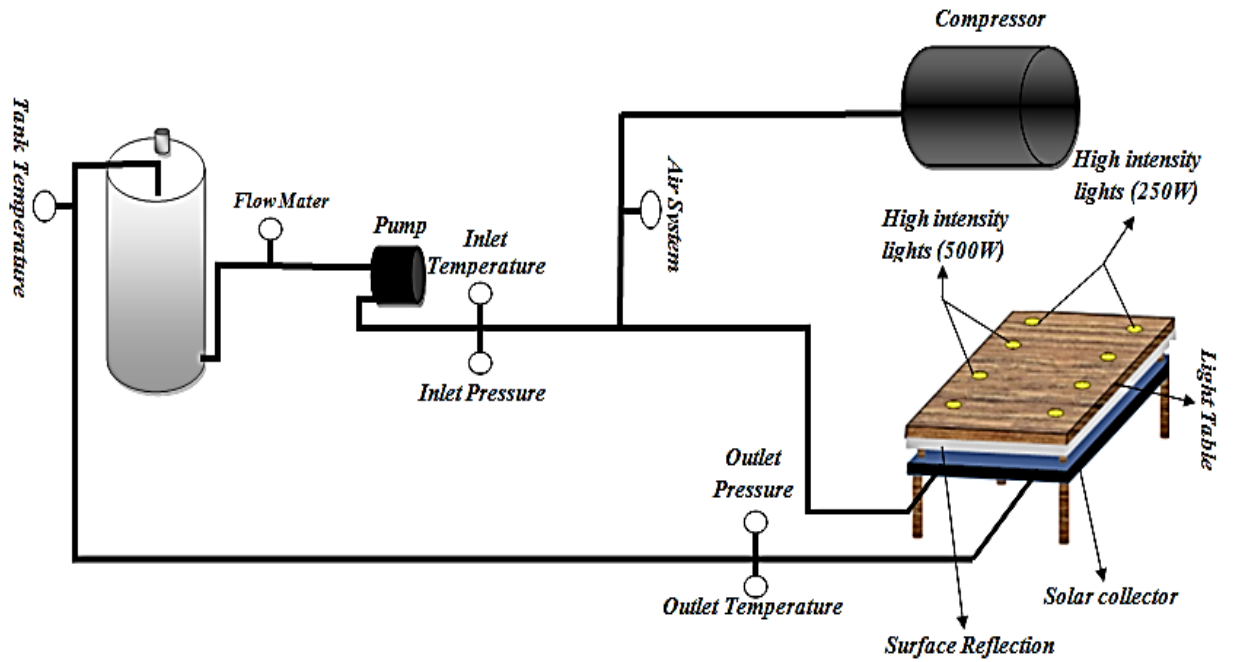


Figure 3.4: System Configuration

3.7.1 Flat Plate Collector (Residential Serpentine) and Light Table

A flat plate collector absorbs heat simply by absorbing solar radiation. The components of a flat plate collector include solar glass, powder-coated aluminum frame, Al-absorber sheet, mineral wool insulation, collector pipe, highly-selective absorber coating, secure glass fixing, meander tube (series type), and revolving groove for assembly. (The flat plate collector specifications can be found in Appendix A).

The flat plate collector used in this thesis had a specific cross sectional area and absorber area of 2.15 m^2 and 2 m^2 , respectively. The Fig. 3.4 illustrates the solar collector that used in research



Figure 3.5: Serpentine Design of Flat Plate

A halogen light (2500 w) is attached at the top of the flat plate collector, with a table, to supply a constant heat flux. The components of the light table include:

- A wooden frame structure, with dimensions of $1.82 \times 1.09 \times 0.11 \text{ m}$ and nine legs. The dimensions of each of table leg are $0.23 \times 0.04 \times 0.04 \text{ m}$.
- A reflectix is placed inside the wooden frame to reflect the light that reflects from the flat plate collector surface.
- Eight halogen lights simulate the sun in the laboratory. The total supplied power is 2500 watts. The light table is illustrated in Fig.3.6

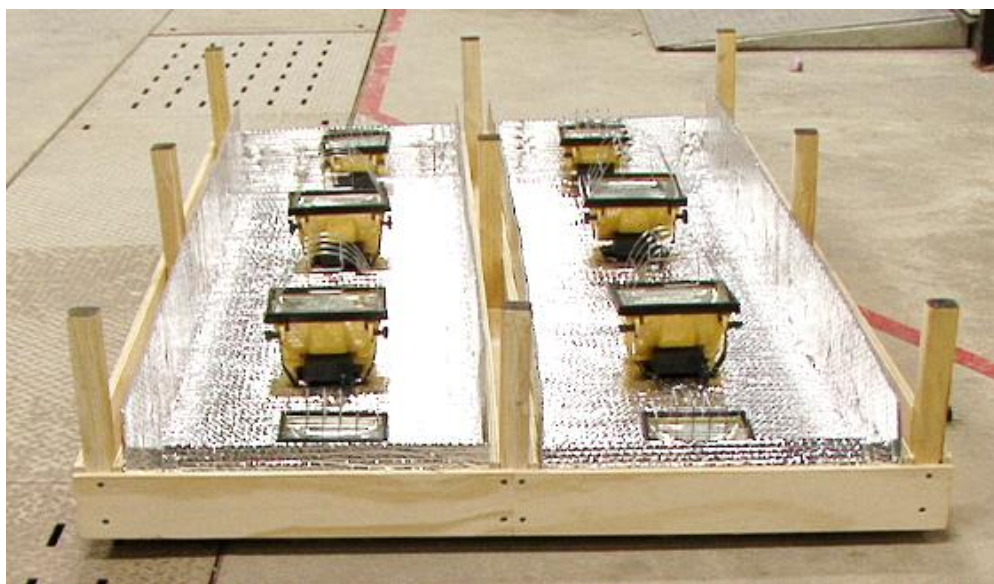


Figure 3.6: Light Table

3.7.2 Turbine Flow Meter and Principle of Operation

Turbine flow meters measure the specific velocity of liquids, gases and vapors in the pipes, including chemicals, hydrocarbons, cryogenic liquids, water, air, and industrial gases. The sensor consists of rotor assembly supported on a shaft that is held in place by triple tube clusters and by locking nuts within the flowmeter housing. The rotor spins on a ceramic ball bearing that is self-lubricated. A magnetic pickup coil is attached to the outside of flow meter housing.

A lower mass rotor design allows a highly rapid dynamic response. The deflector cones are used for eliminating the downstream thrust on the rotor. It also allows the dynamic positioning and orientation of the rotor to be between the deflector cones. The dynamic positioning of the lower mass rotor helps in providing a wide range of capabilities, as well as long bearing life compared to traditional turbine flowmeters. Straightening tubes of integral flow aim to minimize the overall effects of the upstream flow turbulence. Every rotor blade that passes the pickup coil actively generates a strong electrical pulse. The overall frequency of these electrical pulses is directly proportional to the overall flow rate. Summation of the pulses measures the total liquid volume that passes the meter. The total number of electric pulses per unit of the volume is known as the calibration factor. The calibration factor is used to calculate the flow rate and the total amount of flow.

3.7.3 Centrifugal Pump

Major applications of centrifugal pumps include booster service, water circulation, general purpose pumping, spraying systems, and liquid transfer. Centrifugal pumps are used for transporting fluids by converting rotational kinetic energy into hydrodynamic energy. Rotational energy typically is from an engine or electric motor. The fluid enters the pump impeller along or near the built in rotating axis and is then accelerated by an impeller and flows radially into a diffuser (volute chamber).

Both the inlet and outlet of the pump is reduced with 0.5 inch barbed hose connections. The barbed hose connections connect the outlet of pump with the inlet of 4-way connections, and to connect the outlet of the flow meter with the inlet of the pump. A XFC2002-0B Micro-Inverter is used to control the pump speed.

3.7.4 Fluid Reservoir

The reservoir is a domestic water tank. The reservoir has three connections on the top and one on the bottom side. One of the three top connections is used for filling the tank, the second connection is used for the return line from the solar heating system. A temperature sensor and pressure relief valve is also installed at the top. This valve is used to protect the tank from explosions that can be caused by reductions in the temperature and pressure in the tank. The bottom connection is used for joining the main line feeding the pump. The main outlet of the quick connection is connected to the flowmeter inlet and the outlet of the flowmeter is connected to pump inlet.

3.7.5 Intermediate Tubing

PVC tubing is providing the required flexibility and clarity. The dense bore helps to maximize the flow rate and reduce sediment build-up. There were two types of intermediate tubing used in this experiment, black plastic tubing and clear PVC tubing. Black plastic tubing (0.0127 m) is used to connect the reservoir inlet to the pump inlet. Clear PVC tubing (0.0127 m) is used to connect the outlet of the pump to the 4-way connection inlet (i), the 4-way connection outlet (i) is connected to ball valve inlet (i), ball valve outlet (i) is connected to the flowmeter inlet, the flowmeter outlet is connect to the air injection manifold inlet. Clear PVC tubing (0.0097 m) connects the air injection manifold outlet to the solar collector inlet, the solar collector outlet is connected to the 4-way connection inlet (ii), the 4-way connection outlet (ii) is connected to the ball valve inlet (ii), and the ball valve outlet (ii) is connected to the reservoir outlet.

3.7.6 Air Injection System

The air injection system used in the experiment includes that a compressor, microcontroller and air injection manifold. Component configuration of the air injection system is illustrated in Fig.3.7.

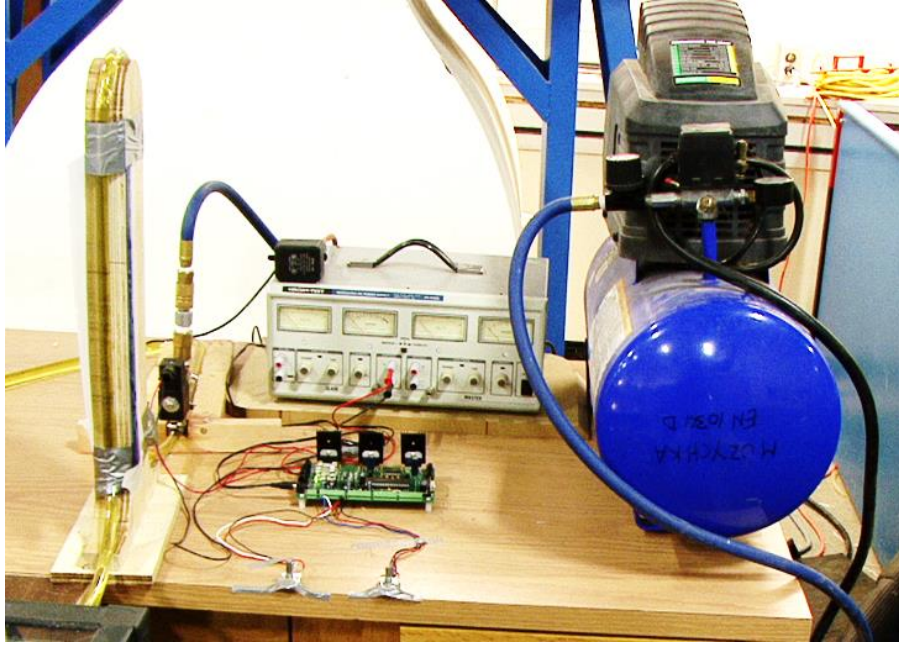


Figure 3.7: Configuration of Air Injection System

3.7.6.1 Compressor and Air Hose

The compressor used in air injection system is a Campbell-Hausfeld 8 Gallon compressor, and has a 125 psi maximum rating with a power of 120v. The air hose has two universal quick connections to join the compressor and air injection manifold. The diameter of the air hose is 0.0095 m. The compressor specifications are presented in Appendix B.

3.7.6.2 Injection Manifold

The air injection manifold used in the experiment consists of several components. The component configuration is illustrated in Fig. 3.8

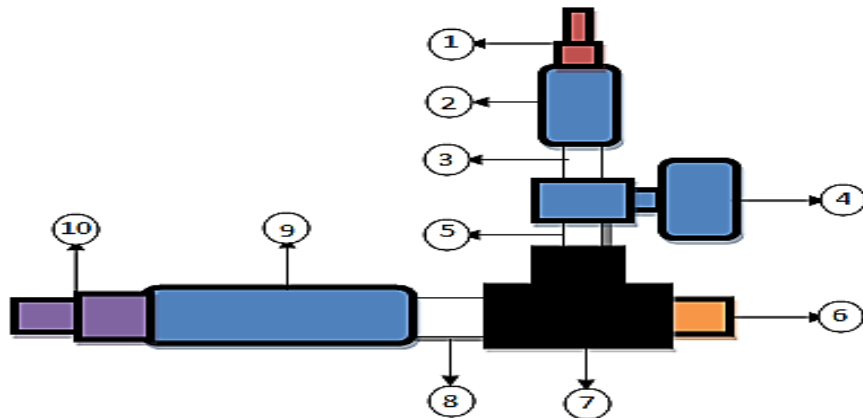


Figure 3.8: Injection Manifold

Table 3.1: Components of the injection manifold

Item No.	The name of the item (Unit)Inch)
1	1/2" Pneumatic Quick-Connect
2	1/2" NPT Check Valve
3	1/2" Male-1/4" Female-Inch - BSP-Bushing length 15mm Brass Pipe Fitting
4	1/4" NPT Solenoid Valve
5	1/4" Brass Male and Male Coupling-NPT
6	3/8" Hose Barb
7	1/4" NPT-T-Junction
8	1/2" Female PipeThread- 1/4" Male Pipe Thread Brass Coupling
9	1/2" NPT Check Valve
10	1/2" Hose Barb

3.7.6.3 Solenoid valve

The solenoid valve used in this thesis is an Omega-Flo 2-Way General Purpose Solenoid. The basic components of the solenoid valve are presented in Fig. 3.9.

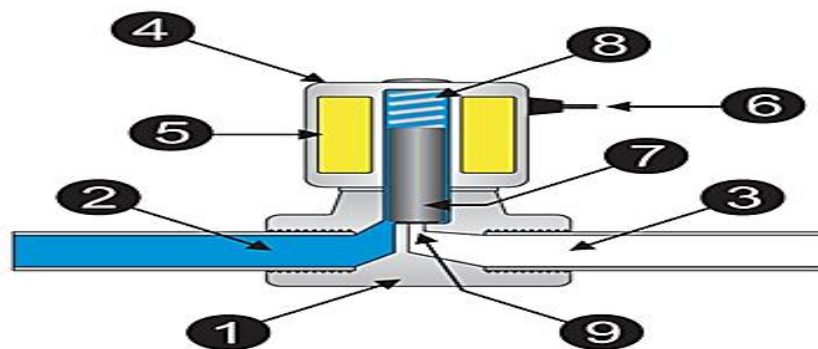


Figure 3.9: Solenoid Valve Components

Table 3.2 Components of the Solenoid Valve

Number of Item	Name of Item
1	Valve Body
2	Inlet Port
3	Outlet Port
4	Coil/Solenoid
5	Coil Windings
6	Lead Wires
7	Plunger
8	Spring
9	Orifice

3.7.6.4 PIC Controller

A PIC Microcontroller controls the solenoid valve in the air injection manifold. The PIC Microcontroller is considered the most important and most efficient component since it can control the total amount of air entering into the Flow-conducted. The PIC Microcontroller was connected with two potentiometers control the liquid length, and length of air bubbles.

3.7.7 Data Collection Subsystem

A Keithley 2700 Multimeter is used for data acquisition of pressure, temperature and flow rates at several locations in system. T-type probes for temperature are installed in three positions throughout the system. One of the T-type probes is installed close to the entrance of the solar collector to measure inlet temperature, one is installed at the exit of the solar collector to measure outlet temperature, and one is installed inside of tank to measure liquid temperature inside the tank. Two Amplified Voltage Output Pressure transducers (PX176) measure the inlet and outlet liquid pressure. A EXTECH 382200 series power supply was used for providing excitation to Keithley 2700 Multimeter .

3.7.8 Setup and Operation of Experiment

The domestic water tank has three connections on the top and one on the bottom side. One of the three top connections was used for filling the tank, the second connection is used for the return line from the solar heating system. A temperature sensor and pressure relief valve was also installed at the top. This valve was used to protect the tank from explosions that can be caused by reductions in the temperature and pressure in the tank. The bottom connection is used for joining the main line feeding the centrifugal pump. The main outlet of domestic water tank was connected to inlet of the centrifugal pump by using black plastic tubing (0.0127 m) and outlet of the centrifugal pump was connected to inlet of ball valve (i) by using clear PVC tubing (0.0127 m). The outlet of ball valve (i) was connected to inlet of the flowrate by using PVC tubing (0.0127 m). The two 4-way connections were used to install two T-type probes for temperature for measuring inlet and outlet temperature from solar thermal collector and two Amplified Voltage Output Pressure transducers (PX176) for measuring inlet and outlet pressure from solar thermal collector. These sensors were connected to a Keithley 2700

Multimeter. The outlet of flowrate was connected to the inlet of 4-way connections (i) by using PVC tubing (0.0127 m). The outlet of 4-way connections (i) was connected to inlet of ball valve (ii) by using PVC tubing (0.0127 m) and outlet of valve (ii) was connected to inlet of T-junction by using PVC tubing (0.0127m). The outlet of t-junction connected to entrance of solar thermal collector by using PVC tubing (0.0097 m). The purpose of using t-junction was that connecting the air injection system with the Flow-conducted. The air injection system used in the experiment includes that a compressor, microcontroller and air injection manifold. The type of compressor used in air injection system is a Campbell-Hausfeld 8 Gallon compressor, and had a 125 psi maximum rating with a power of 120v. The compressor used to provide the system with air. The air hose had two universal quick connections to join the compressor and air injection manifold. The diameter of the air hose was 0.0095 m. The air injection manifold used in the experiment consists of several components. The component configuration is illustrated in Fig. 3.8. The type of solenoid valve used in air injection manifold was an Omega-Flo 2-Way General Purpose Solenoid. This valve was controlled by using a PIC Microcontroller. The PIC Microcontroller is considered the most important and most efficient component since it can control the total amount of air entering into the Flow-conducted. The PIC Microcontroller was connected to two potentiometers control the liquid length, and length of air bubbles. During the single-phase experiments, the solenoid valve remained close while the experiment was running. However, for the two-phase flow, the solenoid valve was opening and closing at certain time intervals during the experiment. Water and glycol have been used in these experiments for both single and two-phase flow. Each experiment ran for 30 minutes, the mass flow rate, inlet and outlet pressure and temperature readings were recorded in specified time intervals.

In the Single-Phase experiment, the liquid (water or Glycol) was pumped to the system using the centrifugal pump from the domestic water tank, the liquid then transferred to the Ball Valve that was used to switch the liquid on and off. After that, the liquid transferred through Flowmeter that recorded the readings of the mass flow rate. In the next step, the liquid reached Four-way connection (i) that included two sensors, pressure sensor and temperature sensor. These sensors are used to measure and record the readings of the Inlet pressure and temperature of the liquid and transfer it to the Data Acquisition system. The liquid then passed through the solar thermal collector that was

used to heat the liquid using Light Lamps, after that, the liquid outlet from the solar thermal collector and went through four-ways connections (ii) that is used to measure and record the readings of the outlet pressure and temperature and transfer it to the Data Acquisition system. The liquid then return to the domestic water tank to start new cycle in the system.

In the Two-Phase, the liquid was (water or Glycol) pumped to the system using the centrifugal pump from the domestic water tank, the liquid then transferred to the Ball Valve that was used to switch the liquid on and off. After that, the liquid transferred through Flowmeter that recorded the readings of the liquid velocity. In the next step, the liquid reached Four-way connection (i) that included two sensors, pressure sensor and temperature sensor. These sensors are used to measure and record the readings of the Inlet pressure and temperature of the liquid and transfer it to the Data Acquisition system. In the next step the liquid reached T-junction that is used to mix the liquid with the air that is generated from Air Injection System. Then, the segmented flow passed through the solar thermal collector that was used to heat the liquid using Light Lamps, after that, the liquid outlet from the thermal collector and went through four-ways connections (ii) that is used to measure and record the readings of the outlet pressure and temperature and transfer it to the Data Acquisition system. The liquid then return to the domestic water tank to start new cycle in the system.

3.7.9 Fluids

The working fluids used in all experiments were water, glycol, and air.

Table 3.3. The properties for water, glycol and air

Parameter (Unit)	Value	Parameter (Unit)	Value
C_p [Water] (J/kg. K)	4130	C_p [Glycol] (J/kg. K)	2428.46
K [Water] (W/m. K)	0.59	K [Glycol] (W/m. K)	0.258
ρ [Water] (Kg/m ³)	1000	ρ [Glyco] (Kg/m ³)	1115
σ [Water] (N/m)	0.073	σ [Glycol] (N/m)	0.048
μ [Water] (Pa. s)	0.001	μ [Glycol] (Pa. s)	0.0169
ρ [Air] (Kg/m ³)	1.18	μ [Air] (Pa. s)	$1.81e^{-5}$
D_T [Collector] (m)	0.010922	L_T [Collector] (m)	18.88

Chapter 4

4.1 Introduction

In this chapter, the experimental data for single and two-phase flow is presented. There are two sets of data for single and two-phase flow. For single-phase flow, the working fluid used for the first set was water and glycol for the second set. For two-phase flow, the working fluid was water-air for the first set and glycol-air for the second set. In the first set of data, three experiments are conducted for single and two-phase flow with a constant flow rate. The experiments conducted in the second set are four experiments for single and two-phase flow with a constant flow rate as well and six experiments conducted with different types of liquid void fraction (α_l).

4.2. Data analysis

After the experimental setup was completed several experiments were conducted at different flow rates, and experimental data was collected at each flow rate. The experimental data was used to calculate several variables, such as the rate of heat transfer (Q), tank temperature slope, average bulk temperature, time required for raising the tank temperature from $T_{Minimum}$ to $T_{maximum}$, energy gained by the tank (\dot{E}), and enhancement ratio.

The rate of heat transfer in the collector is calculated by Eq. (4.1):

$$Q = \dot{m}c_p (T_o - T_i) \quad (4.1)$$

Where \dot{m} is the mass flow rate of the working fluid, c_p is the specific heat of the working fluid, T_o is the outlet temperature of the working fluid from the solar thermal collector, and T_i is the inlet temperature of the working fluid to the solar collector.

The slope of the tank temperature is calculated by using Eq. (4.2):

$$S_{Tank} = \frac{\Delta T}{\Delta t} = \frac{T_f - T_s}{t_f - t_s} \quad (4.2)$$

Where T_f is the tank temperature at the final point in the experimental data, T_s is the tank temperature at the starting point of the experiment, t_f is time at the final point in the experimental data, and t_s is time at the starting point of the experiment.

The average bulk temperature of the solar thermal collector is given as Eq. (4.3):

$$\bar{T}_{Bulk} = \frac{T_o + T_i}{2} \quad (4.3)$$

Where T_o is the outlet temperature of the working fluid from the solar thermal collector, and T_i is the inlet temperature to the solar thermal collector.

The time required for heating the temperature of the tank from T_{min} to T_{max} can be calculated by using Eq. (4.4):

$$T_R = \frac{T_{max} - T_{min}}{S_{Tank}} \quad (4.4)$$

The average heat transfer rate into the tank during each experiment is calculated by using Eq. (4.5):

$$\dot{E} = \rho c_p V \frac{\Delta T}{\Delta t} \quad (4.5)$$

Where ρ is the density of the working fluid, c_p is the specific heat of the working fluid, V is the volume of the working fluid inside the tank, and $\frac{\Delta T}{\Delta t}$ is the slope of the tank temperature rise.

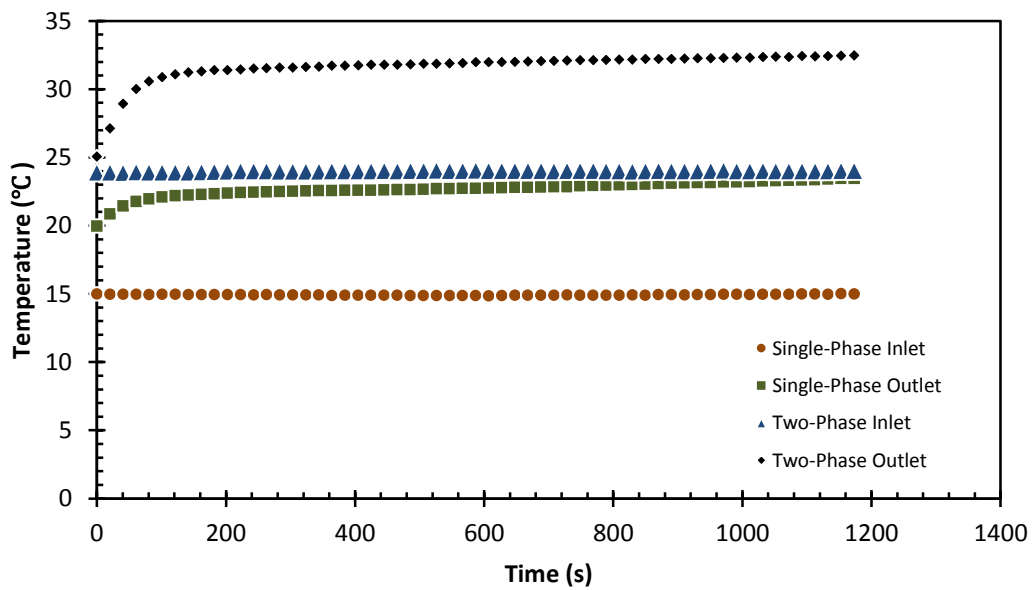
Also, the enhancement ratio of two-phase flow is defined as the ratio between the rate of heat transfer for two-phase flow and the rate of heat transfer for single-phase flow at a constant flow rate. The enhancement ratio of two-phase flow is calculated by Eq. (4.6):

$$\text{Enhancement}_{\text{Two-Phase}} = \frac{Q_{\text{Two-Phase}}}{Q_{\text{Single-Phase}}} \quad (4.6)$$

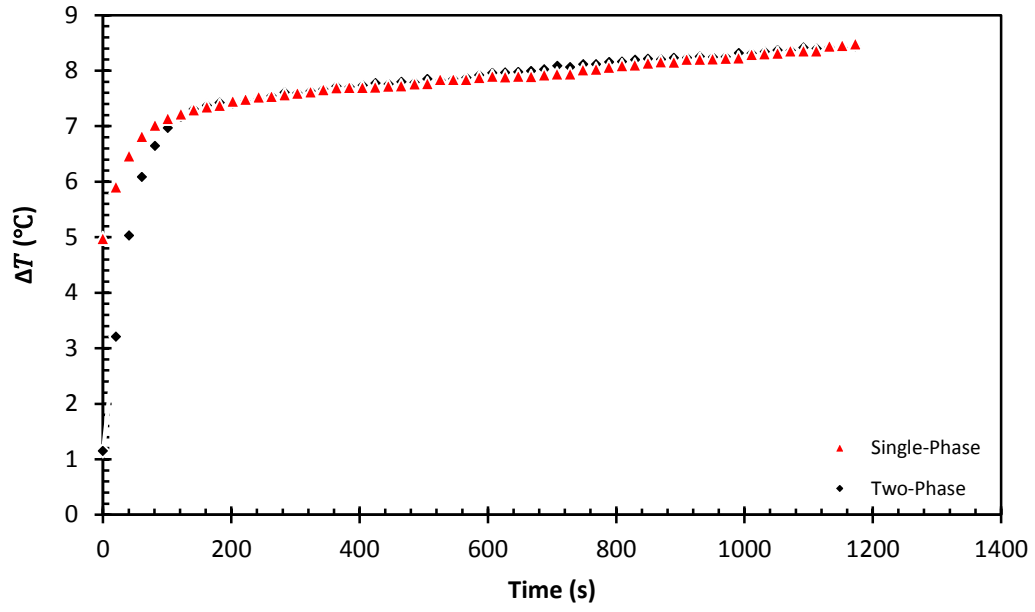
4.3 Single and Two-Phase Flow in a Solar Collector with Water

The first experiment is conducted with a flow rate of 1.562 L/min. As illustrated in Fig. 4.1-a, the outlet temperature increases considerably from 25°C to 30°C between 0 s to 101 s and between 101 s to 1152 s the outlet temperature rises slowly from 30°C to 32°C for two-phase flow. For single-phase flow, the outlet temperature increases suddenly, from 19.9°C to 21.9°C between 0 s and 80 s, and from 80 s to 1152 s the outlet temperature increases slightly from 21.9°C to 24.0°C. The sudden increase in outlet temperature that occurs in both cases, single and two-phase flow, at the beginning of

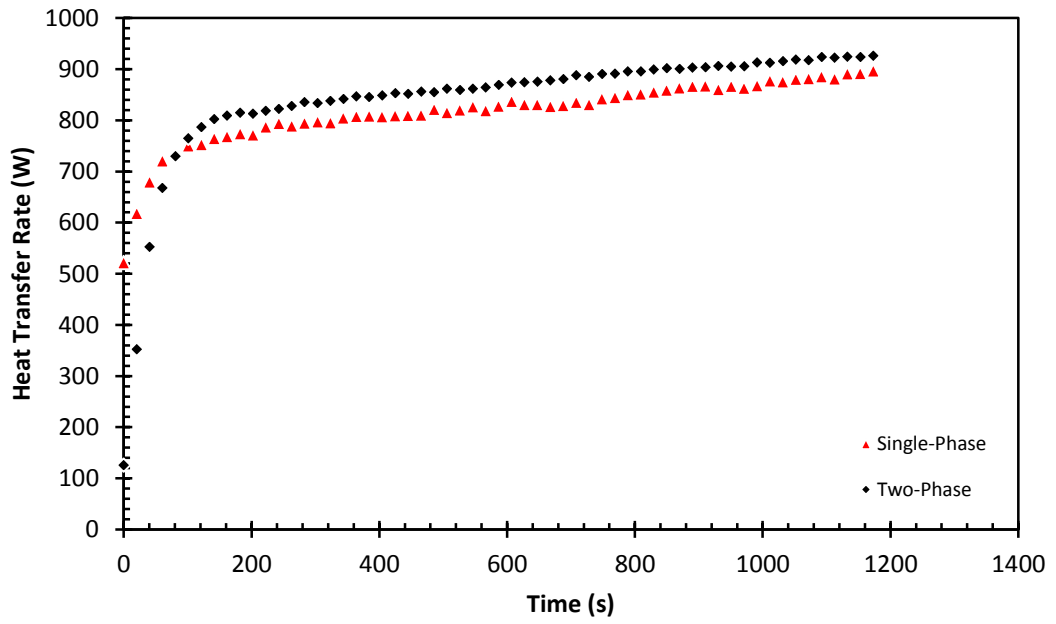
the experiment was due to the experiment stabilization. The inlet temperature in both cases remains constant. The difference between outlet and inlet temperature (ΔT) in both cases also remains constant during the experiment, except at the beginning when the experiment is not stable. The reason is that the amount of heat transmitted from the surface of absorption to the fluid during the flat plate collector is constant. Fig 4.1-b shows that the temperature difference for two-phase flow (ΔT_{TP}) is higher than the temperature difference for single-phase (ΔT_{SP}), with an average value of 8.38°C and 8.36°C for two and single-phase flow, respectively. The difference between temperature in both single and two phase-flow (ΔT_{total}) is approximately 0.02°C. Fig. 4.1-c illustrates that the heat transfer rate (Q_{TP}) increases dramatically, from 126.0 W to 786.8 W between 0 s to 121 s, and from 121 s to 1152 s the heat transfer rate increases from 786.8 W to 924.2 W for two-phase flow. For single-phase flow, there is a substantial increase in the heat transfer rate (Q_{SP}) from 521.9 W to 753.2 W between 0 s to 80 s, while between 80 s to 1152 s the heat transfer rate rises slightly, from 753.2 W to 896.7 W. As illustrated in Fig 4.1-c, the heat transfer rate (Q_{TP}) for two-phase flow is higher than the heat transfer rate (Q_{SP}) for single-phase flow, with an average value of 920.02 W and 883.17 W for two-phase and single-phase, respectively. The difference between the heat transfer rate (ΔQ) in both single and two-phase flow is approximately 36.85 W. The heat transfer enhancement of two-phase flow is approxia.



(a)



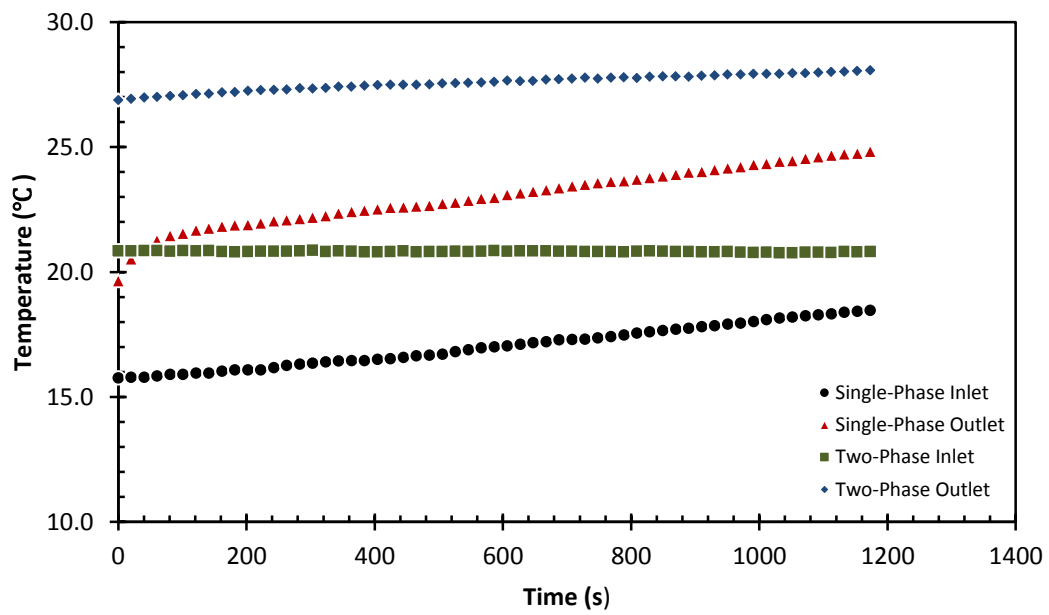
(b)



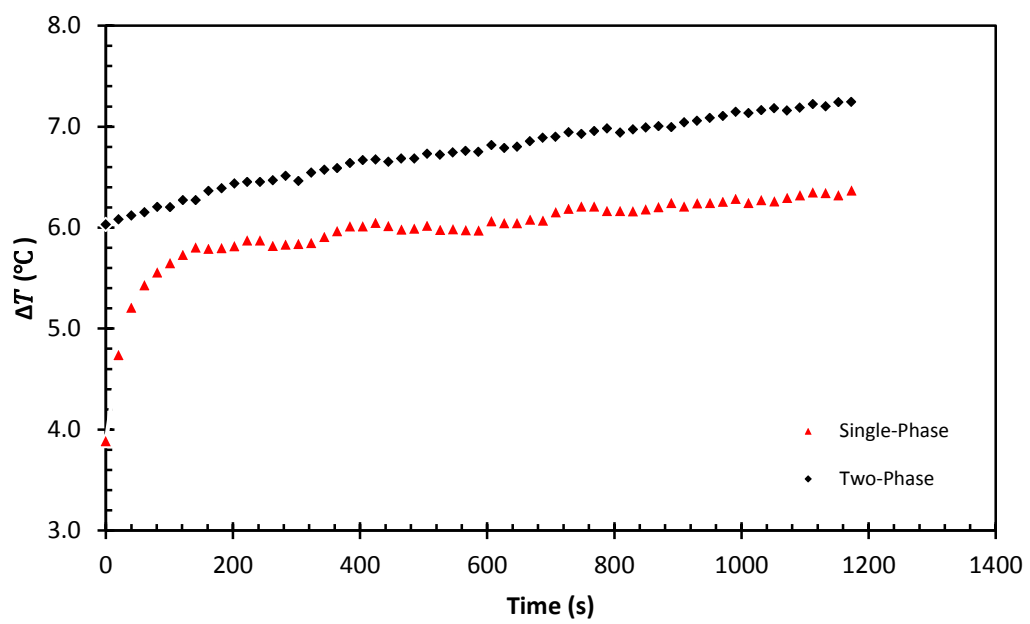
(c)

Fig.4.1. Thermal effectiveness at 1.552(L/min) for (a) inlet and outlet temperature, (b) temperature difference, and (c) heat transfer rate

The flow rate used in the second experiment is 2.062 L/min. Fig. 4.2-a shows the relationship between the inlet and outlet temperature. The outlet temperature increases gently from 26°C to 28.1°C between 0 s to 1173.0 s for two-phase flow. For single-phase flow, there is a sudden increase in outlet temperature at the start the experiment, from 19.6°C to 20.8°C, between 0 s to 40.4 s. From 40.4 s to 1173.0 s the outlet temperature increases gradually from 20.8°C to 24.8°C. Between 0 s to 1173.0 s, the inlet temperature is relatively stable during the experiment for two-phase flow, with a value of 20.8°C, while there is a gradual increase in inlet temperature, from 15.8°C to 18.5°C, between 0 s to 1173.0 s, for single-phase flow. Part (a) also shows that the difference between inlet and outlet temperature remains approximately unchanged in both cases of single and two-phase flow during the experiment, with average values of 7.19°C and 6.311°C for two and single-phase flow, respectively. The cause is the heat transferred from the flat plate collector to the fluid that is passing through the collector at a constant rate. The relationship between the temperature differences in single and two-phase flow, with the time when the flow rate is 2.062 L/min is shown in Fig. 4.2-b. During the period between 0 s to 1173.0 s there is a gradual increase in temperature difference from 6°C to 7.2°C for two-phase flow. For single-phase, the temperature difference increases considerably, from 3.4°C to 5.7°C, between 0 s and 121 s while there is a small increase in the temperature difference from 5.7°C to 6.4°C over the period between 121 s and 1173.0 s. Furthermore, the temperature difference for two-phase flow is higher than the temperature difference for single-phase flow, with an average value of 7.19°C and 6.31°C for two and single-phase flow and the difference between temperature difference in both cases (ΔT_{total}) is approximately 0.88°C. As can be noted from the relationship with the heat transfer rate, there is a gradual increase in the heat transfer rate from 854 W to 1030 W between 0 s to 1173.0 s for two-phase flow. For single-phase flow, there is a significant increase in the heat transfer rate, from 546 W to 807.3 W between 0 s and 121 s and from 121 s to 1173 s, the heat transfer rate rises slightly from 807.3 W to 903.4 W, although the heat transfer rate for two-phase flow is higher than in single-phase flow, with an average value of 1020.0 W and 898.24 W for two and single-phase flow, respectively. Also, Fig. 4.2-c shows that the difference between the heat transfer rate (ΔQ) in both cases, single and two-phase flow, is approximately 121.8 W. The heat transfer enhancement of two-phase flow is 1.14.



(a)



(b)

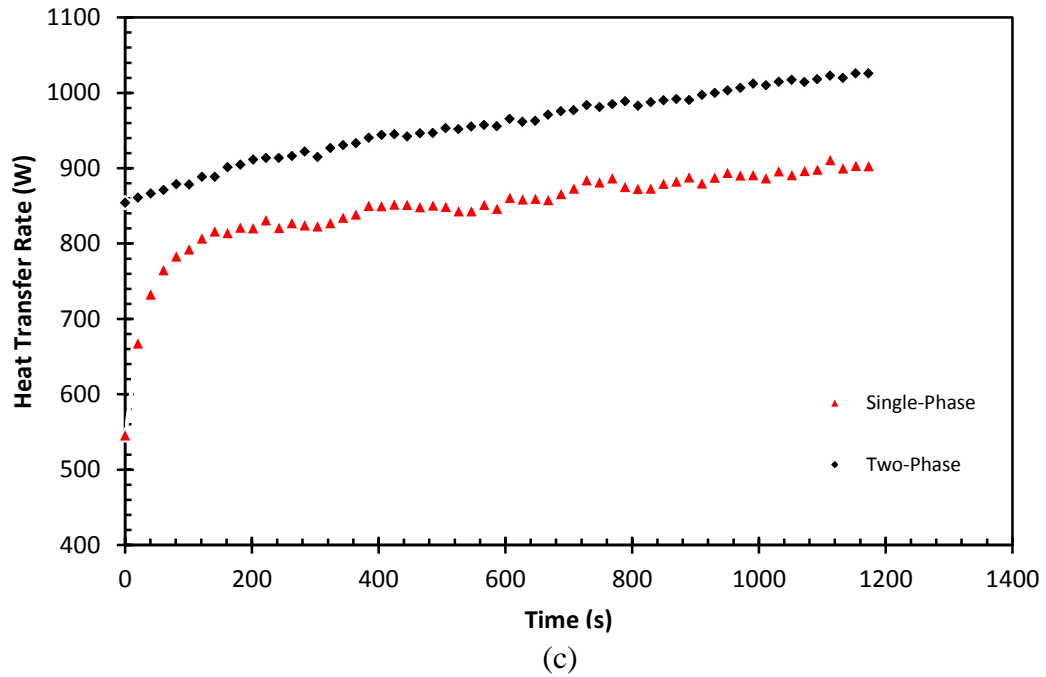
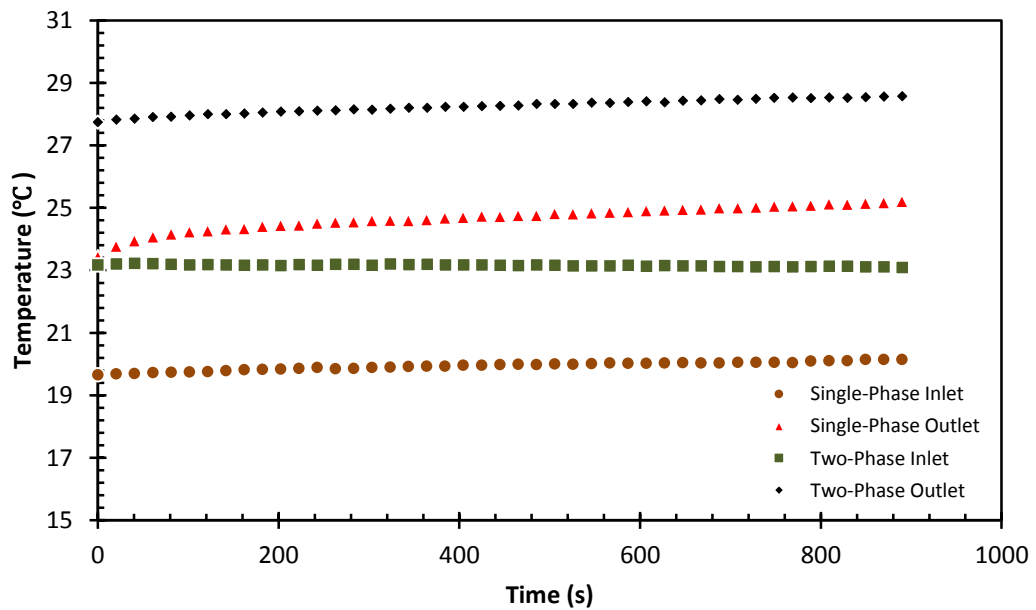


Fig.4.2. Thermal effectiveness at 2.062 (L/min) for (a) inlet and outlet temperature, (b) temperature difference, and (c) heat transfer rate

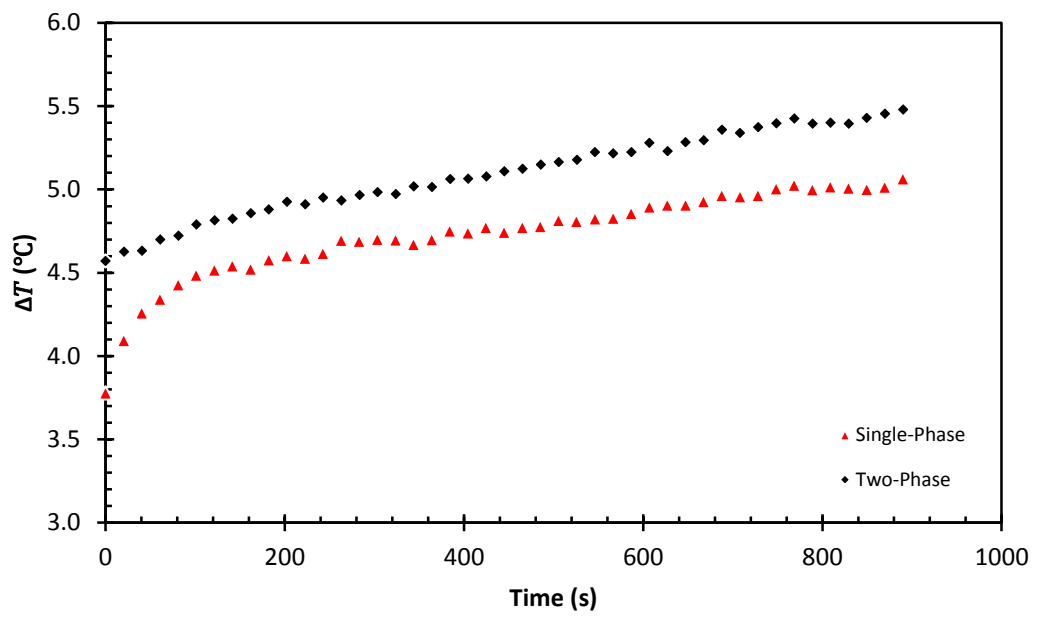
Fig. 4.3-a in the third experiment, when the flow rate is 2.516 (L/min), illustrates the transient relationship between inlet and outlet temperature for single and two-phase flow. The outlet temperature increases slowly from 27.7°C to 28.7°C for two-phase flow between 0 s and 890 s and the inlet temperature is relatively stable during the experiment, with an average of 23.15°C. The outlet temperature for single-phase shows the same behavior for two-phase flow, and there is a small increase in outlet temperature, from 23.4°C to 25.2°C between 0 s to 890 s, while the inlet temperature for single-phase flow remains approximately unchanged during the experiment, with a value of 19.9°C. Furthermore, as can be seen from Part (a), the difference between inlet and outlet temperature (ΔT) in single and two-phase flow is relatively constant during the experiment, with a value of 5.4 and 5°C for two-phase and single-phase, respectively. The heat transferred from absorber to fluid with a constant rate during the solar collector and the difference between temperature difference in single and two-phase flow (ΔT_{total}) is approximately 0.4°C. Fig. 4.3-b shows that from 0 s to 890 s there is a gradual increase in the temperature difference for two-phase flow from 4.6°C to 5.5°C. There is a sudden increase in the temperature difference for single-phase from 3.8°C to 4.5°C, between 0 s and 101 s, while from 101 s to 889.7 s the temperature

difference rises gradually from 4.5°C to 5.1°C. Also, Part (b) illustrates that the temperature difference for two-phase flow is higher than that the temperature difference for single-phase flow, with a value of 5.4°C and 5.0°C for two-phase and single-phase flow, respectively. Fig. 4.3-c shows the relationship between the heat transfer rate in both cases, single and two-phase flow, and time when the flow rate is 2.516 L/min. From 0 s to 890 s, the heat transfer rate increases from 791.8 W to 949.5 W for two-phase flow. For single-phase flow, there is a significant increase in the heat transfer rate from 662.4 W to 798.6 W between 0 s to 121 s and from 121 s to 889.7 s the heat transfer rate rises slightly from 798.6 W to 889.4 W. Part (c) also shows that the heat transfer rate for two-phase flow is higher than the heat transfer rate for single-phase flow, with an average value of 937.16 W and 881.63 W for two-phase flow and single-phase flow, respectively. Also, the difference between the heat transfer rate in both cases (ΔQ), single and two-phase flow, is approximately constant during the experiment, with a value of 55.52 W. The heat transfer enhancement of two-phase flow is 1.06.

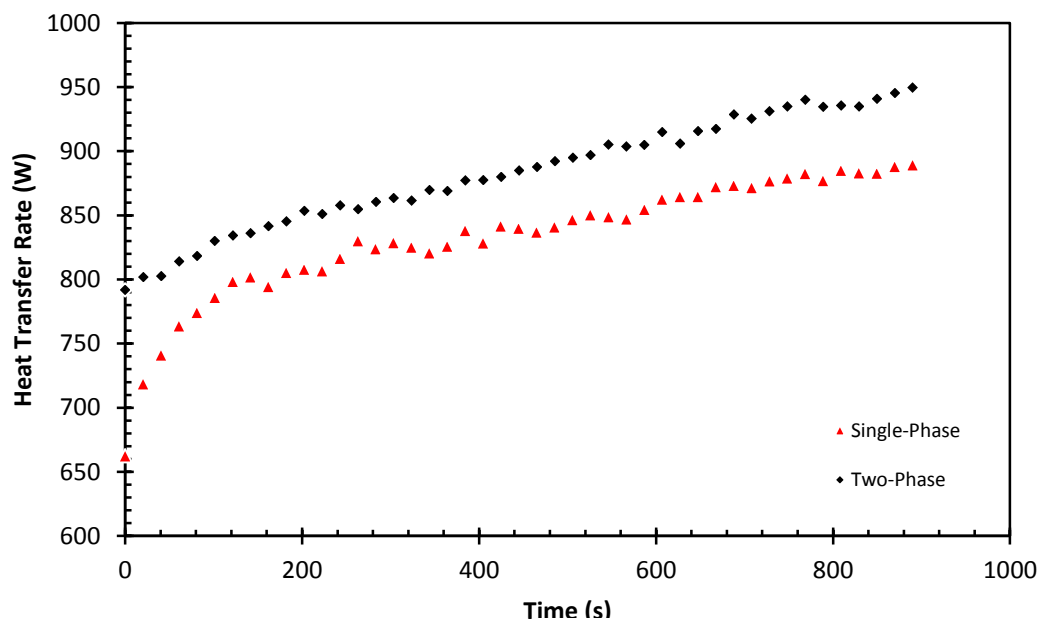
As illustrated in Figs. 4.1-4.3 the two-phase flow system is better than the single-phase flow system. This is because of the two major effects in the further enhancement of the heat transfer rate in the two-phase flows of non-boiling: the internal circulations present in the slugs that eventually lead towards a much greater radial rate of heat transfer, as well as an increased slug velocity.



(a)



(b)



(c)

Fig.4.3. Thermal effectiveness at 2.516 (L/min) for (a) inlet and outlet temperature, (b) temperature difference, and (c) heat transfer rate

Table 4.1: Summary of results for single-phase (water) and two-phase flow (water-air) experiments.

Test	Type of Experiment	\dot{Q} (L/min)	\dot{m} (kg/s)	ΔT_c (°C)	Q_c (W)	$Enh_{Two-Phase}$	$Enh_{Two-Phase}\%$
1 _a	Single-Phase	1.527	0.0255	8.36	883.17	1.04	4.2
1 _b	Two-Phase	1.595	0.0266	8.38	920.02		
2 _a	Single-Phase	2.068	0.0344	6.31	898.24	1.14	13.6
2 _b	Two-Phase	2.057	0.0343	7.19	1020.01		
3 _a	Single-Phase	2.559	0.0426	5.01	881.63	1.06	6.3
3 _b	Two-Phase	2.473	0.0411	5.41	937.16		

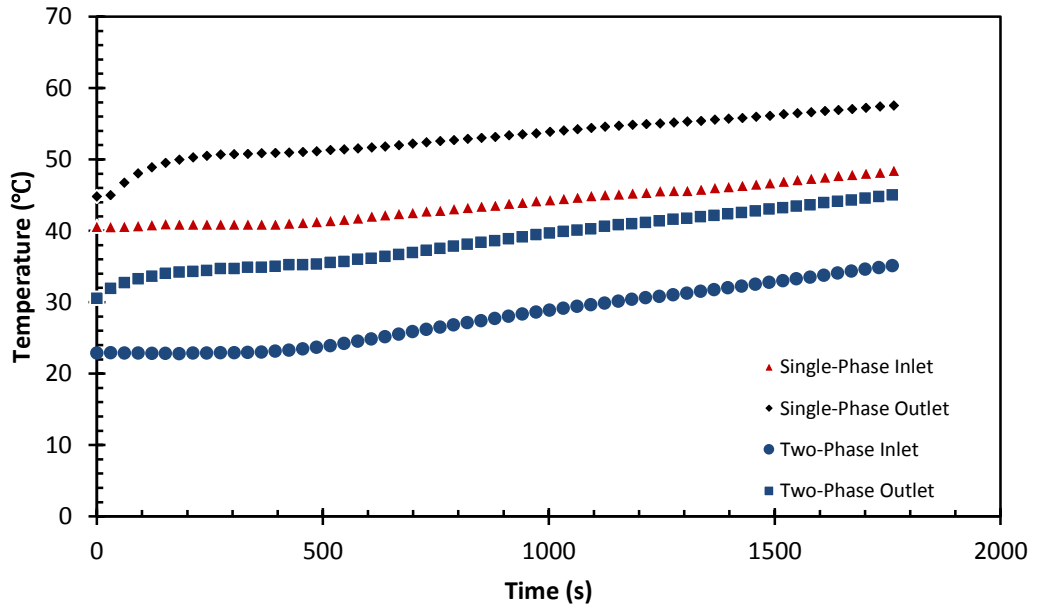
4.4 Single and Two-phase Flow in a Solar Collector with Glycol

Four experiments are conducted by using glycol for single-phase and glycol-air for two-phase flow with a constant flow rate in each case, single and two-phase flow, with an average flow rate of 0.6, 1.7, 2.1, and 3 L/min.

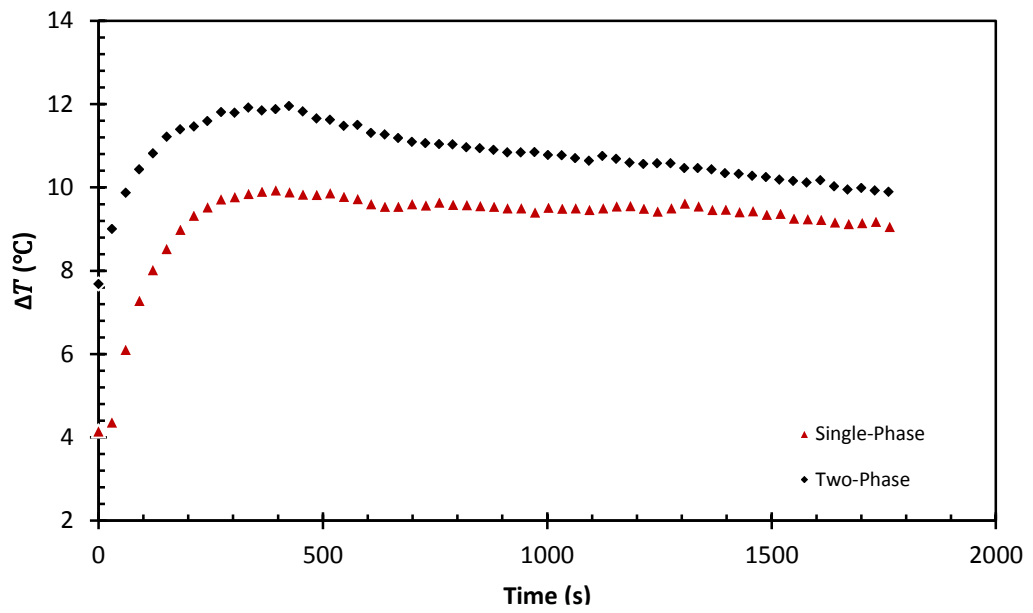
The first experiment is conducted when the flow rate is 0.653 (L/min) and Fig. 4.4-a illustrates the relationship between the inlet and outlet temperature in both cases with time. The outlet temperature increases considerably from 44.8°C to 49.5°C for single-phase flow between 0 s and 152 s and from 152 s to 1763 s the outlet temperature rises slightly, from 49.5°C to 57°C. For two-phase flow, the outlet temperature increases suddenly from 30.5°C to 33.6°C between 0 s to 121.3 s and there is a gradual increase in outlet temperature from 33.6°C to 45°C, between 121 s to 1760 s. The inlet temperature for single-phase remains constant between 0 s to 395.3 s, with a value of 40.9°C and there is a small increase in the inlet temperature from 40.9°C to 48.5°C between 395.3 s and 1763 s. For two-phase flow, the inlet temperature remains approximately constant from 0 s to 395.3 s, with a value of 23.1°C, while from 395.3 s to 1760 s there is a slight increase in inlet temperature from 23.1°C to 35.1°C. Part (a) shows that the difference between inlet and outlet temperature in both cases, single and two-phase, is approximately constant, with a value of 10.06°C and 9.22°C for two-phase and single-phase, respectively. Therefore, the heat is transferred from the absorber to the fluid with a constant rate when the fluid is passing through the solar collector. Fig. 4.4-b illustrates the relationship between the temperature difference (ΔT) in single and

two-phase flow and time when the flow rate is 0.653 L/min. There are three regions that can be seen in Part (b). The first region shows that from 0 s to 394 s the temperature difference increases considerably from 7.7°C to 11.9°C for two-phase flow and from 4.1°C to 9.9°C for single-phase flow. The temperature difference is at its highest level, with a value of 11.95°C at 424 s for two-phase flow and 9.94°C at 395 s for single-phase flow. From 455 s to 1760 s, there is a gradual decrease in the temperature difference from 11.82°C to 9.89°C for two-phase flow and from 425 s to 1763 s, the temperature difference decreases slowly from 9.89°C to 9.06°C for single-phase flow. The decline that occurred in the third region is due to the loss that occurred in the non-insulated pipe. Part (b) shows that the temperature difference for two-phase flow is higher than the temperature difference for single-phase flow, with a value of 10.06°C and 9.22°C for two-phase and single-phase flow, respectively. Also, the difference between temperature difference for two and single-phase flow (ΔT_{toata}) is approximately 1.09°C. The relationship between the heat transfer rate in single and two-phase with time can be seen in Fig. 4.4-c. It shows that there is a sudden increase in the heat transfer rate from 225.2 W to 348.1 W between 0 s and 394.5 s for two-phase flow. The same behavior can be seen in the case of single-phase flow, a sudden increase in the heat transfer rate from 121.80 W to 290.4 W, between 0 s and 364 s due to the fact that the experiment is taking time to become stable. The heat transfer rate reaches a peak of 350.5 W at 424 s for two-phase flow and 291 W at 359 s for single-phase flow. After this point, the heat transfer rate decreases gradually in both cases, from 346.6 W to 290.0 W between 455 s and 1760 s for two-phase flow and from 289.9 W to 265.7 W between 425 s and 1763 s for single-phase flow. The reason for this is the loss that occurred in the non-insulated pipe. Fig. 4.4-c illustrates that the heat transfer rate for the two-phase flow is higher than for the single-phase flow, with an average of 295.04 W and 270.25 W for two-phase and single-phase flow, respectively. The difference between the heat transfer rate in single and two-phase flow is approximately 24.79 watts. Also, the heat transfer enhancement of two-phase flow is 1.10. The temperature of the tank (T_{Tank}) increases gently with time in both cases, but the temperature of the tank is increased more quickly for two-phase flow than single-phase flow, which leads to the tank temperature slope for two-phase flow $\left(\frac{\Delta T}{\Delta t}\right)_{TP}$ being higher than the tank

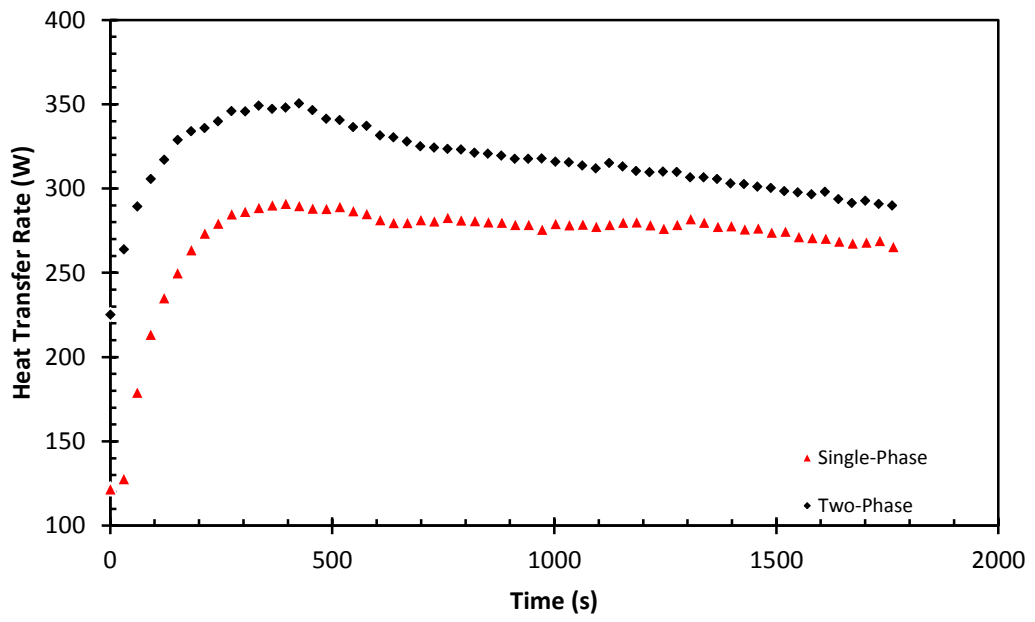
temperature slope for the single-phase flow $\left(\frac{\Delta T}{\Delta t}\right)_{SP}$, with a value of $34.7 \frac{^{\circ}\text{C}}{\text{h}}$ and $23.1 \frac{^{\circ}\text{C}}{\text{h}}$ for two-phase flow and single-phase flow, respectively. Thus, the number of hours required for raising the tank temperature from 25°C to 70°C for two-phase flow is approximately one hour and eighteen minutes and for single-phase flow it is two hours. The energy gained from the tank for two-phase flow (\dot{E}_{TP}) is higher than for single-phase flow (\dot{E}_{SP}) , with a value of 782.9 W and 512.24 W for two-phase and single-phase flow, and the difference in energy between single and two-phase flow $(\Delta \dot{E})$ is approximately 261.66 watts . Fig. 4.4-d shows that the two-phase flow system is better than the single-phase flow system. Fig. 4.4-e illustrates the relationship between the average bulk temperature (\overline{T}_b) and tank temperature with time in single and two-phase flow. In this experiment, it can be seen in Part (e) that the amount of change in average bulk temperature is close to the amount of change in temperature inside the tank in both cases, single and two-phase flow, except at the beginning period, when the experiment is not stable.



(a)



(b)



(c)

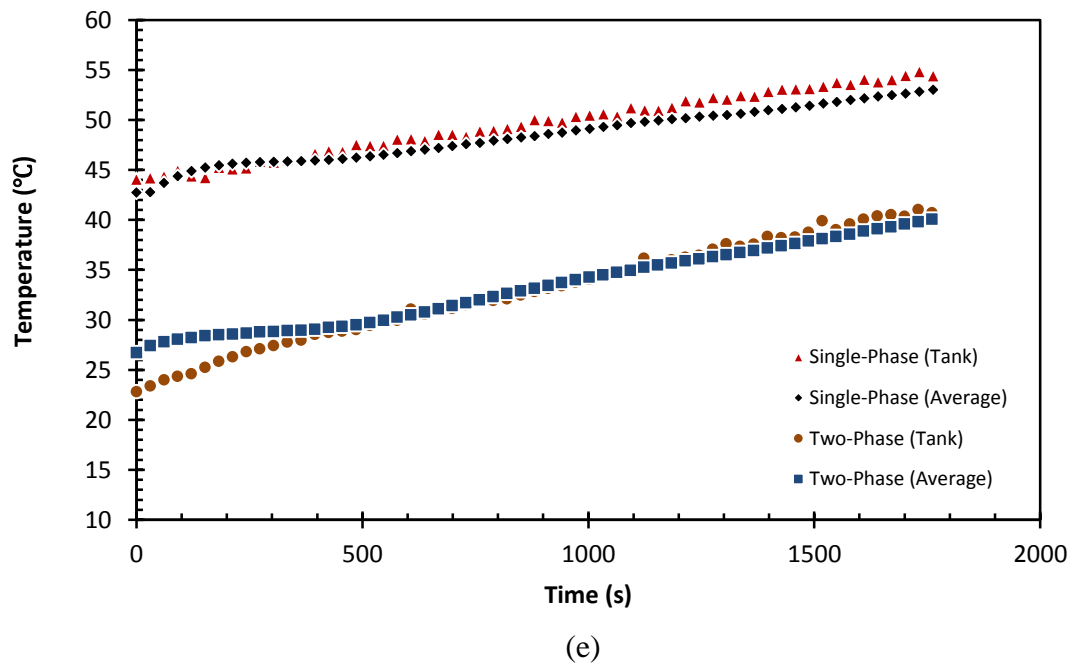
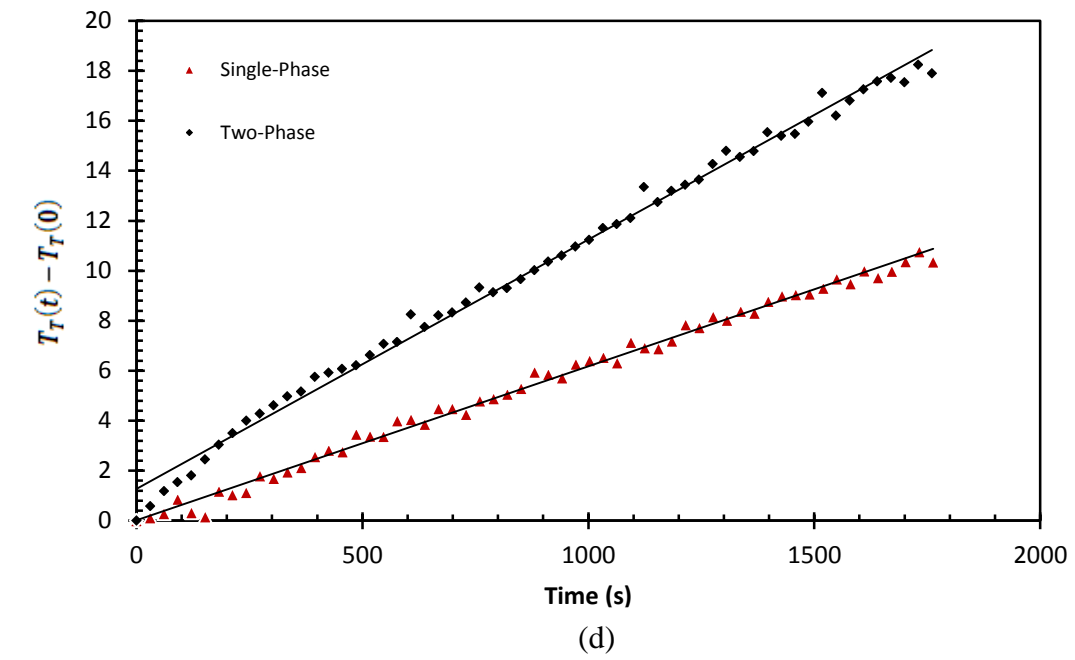
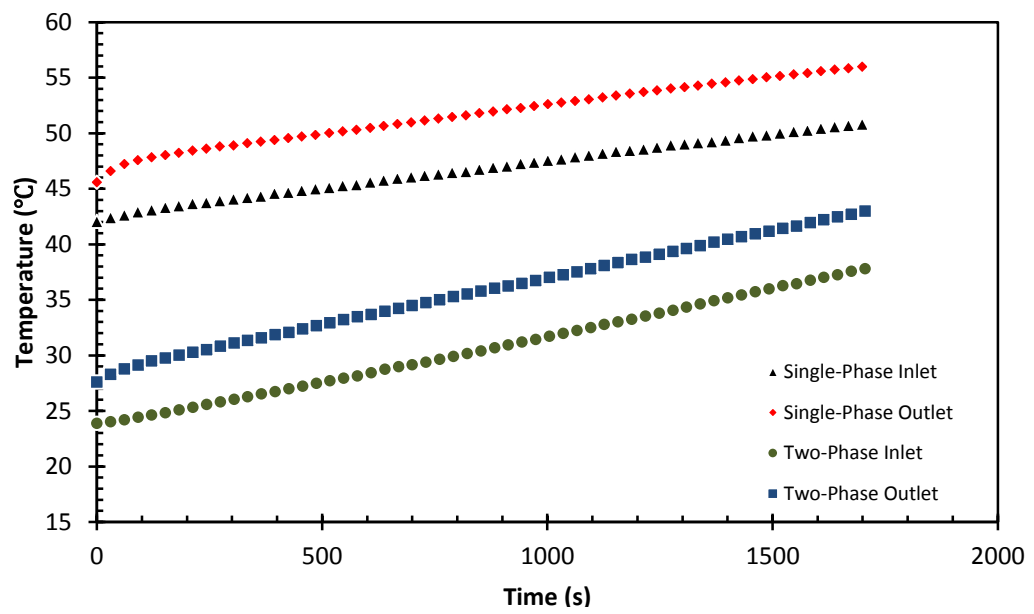


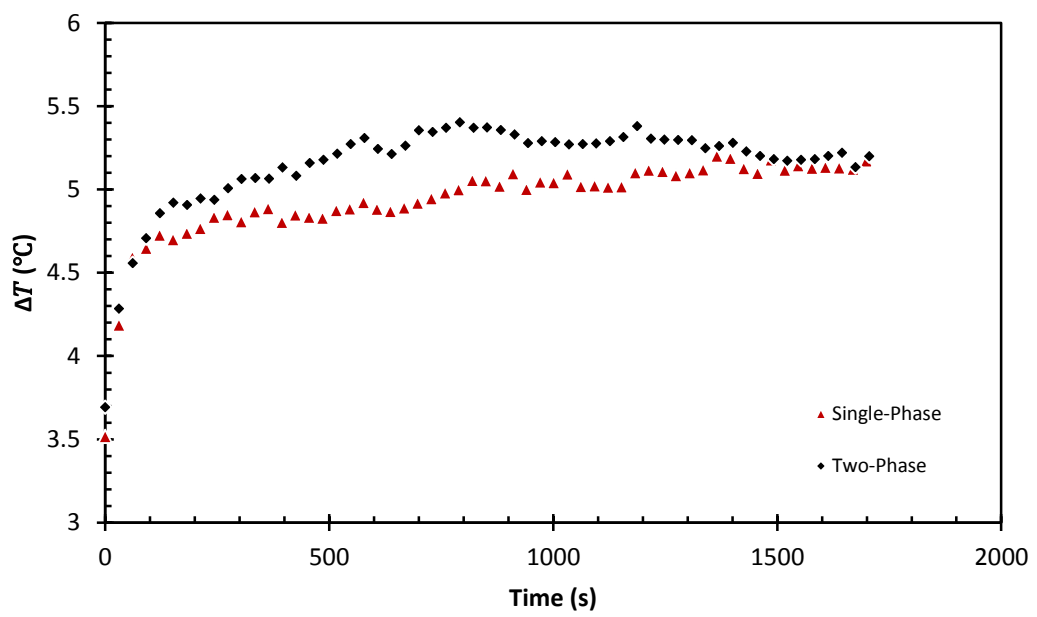
Fig.4.4. Transient thermal effectiveness at 0.653 (L/min) for (a) inlet and outlet temperature, (b) temperature difference, (c) heat transfer rate, (d) temperature difference in the tank, and (e) average bulk and tank temperature.

Fig. 4.5-a shows the results of the inlet and outlet temperature in single and two-phase flow for the experiment conducted when the flow rate is approximately 1.7071 (L/min). The outlet temperature for the single-phase flow increases suddenly from 45.6°C to 47.6°C between 0 s to 90 s and between 90 s and 1698 s the outlet temperature increases gradually from 47.7°C to 56°C. For two-phase flow, from 0 s to 1705 s, the outlet temperature rises slowly from 27.6°C to 43°C. The inlet temperature for both cases increases gradually from 42.1°C to 50.8°C between 0 s and 1698 s for single-phase flow and from 23.9°C to 37.8 °C between 0 s to 1705 s. As can be noted from Part (a) the difference between the inlet and outlet in both cases remains constant over the experiment, with an average value of 5.19°C and 5.13°C for two-phase and single-phase flow, respectively. As can be noted from Fig. 4.5-b, between 0 s and 121 s, the temperature difference increases from 3.7°C to 4.9°C for the two-phase flow and between 121 s and 761 s the temperature difference increases gradually from 4.9°C to 5.4°C. Also, the temperature difference reaches a peak of 5.4°C at approximately 791 s. After that, from 791 s to 1705 s, there is a drop of 0.3°C in the temperature difference, due to the loss that occurs in the non-insulated pipe. For single-phase flow, there is also an increase in temperature difference from 3.5°C to 4.7°C between 0 s and 91 s and there is a slight increase in the temperature difference from 4.7°C to 5.1°C between 91 s to 1674.8 s. Furthermore, the temperature difference for two-phase flow is higher than the temperature difference for single-phase flow, with an average value of 5.19°C and 5.13°C for two-phase and single-phase, respectively. Part (b) shows that the difference between temperature difference in single and two-phase flow is approximately 0.25°C. Illustrated in Fig. 4.5-c is the relationship between the heat transfer rate with time when the flow rate is 1.7071 (L/min). Between 0 s and 121 s there is a significant increase in the heat transfer rate from 283.7 W to 361.6 W for two-phase flow and gradually from 361.6 W to 412 W between 121 s and 761 s. Also, the heat transfer rate is at its highest level at approximately 791s, with a value of 415 W. After that, between 791s and 1705s, there is a slight decrease in the heat transfer rate from 415.1 W to 399.4 W, with a value of 21 W. For single-phase flow, there is also a sudden increase in the heat transfer rate from 270.3 W to 361.6 W between 0 s and 91 s and between 91 s and 1674.8 s the heat transfer rate increases slowly, from 361 W to 397.4 W. Thus, Part (c) shows that the heat transfer rate for two-phase flow is higher than the heat transfer rate for single-phase

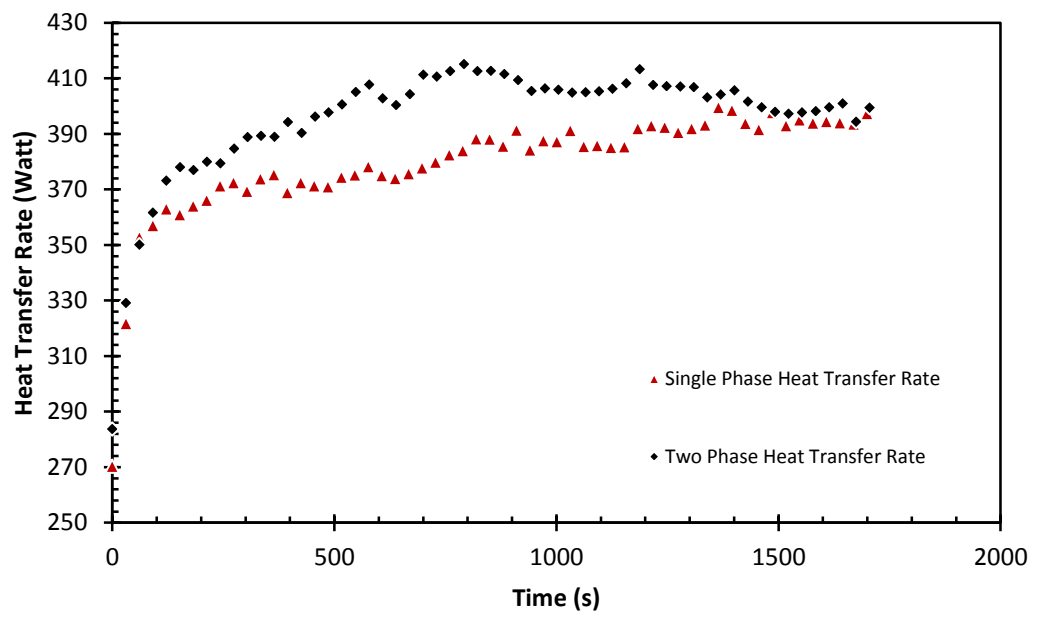
flow, with an average value of 401.06 W and 394.48 W for two-phase and single-phase, respectively. The difference between the heat transfer rate in single and two-phase flow is approximately 6.58 W. The heat transfer enhancement of two-phase flow is 1.01. The relationship between the tank temperature (T_{Tank}) and time when the flow rate was 1.7071 L/min for both cases, single and two-phase flow, can be seen in Fig. 4.4-d. The temperature inside the tank increases gradually with time in both cases. Furthermore, the tank temperature for two-phase flow is higher than the tank temperature for single-phase flow and the tank temperature slope for two-phase flow is higher than the tank temperature slope for single-phase flow, with a value of $37.6 \frac{^{\circ}\text{C}}{\text{h}}$ and $19.1 \frac{^{\circ}\text{C}}{\text{h}}$ for two-phase flow and single-phase flow, respectively. Thus, the time required for raising the tank temperature from 25°C to 70°C when using two-phase flow is approximately one hour and eleven minutes, while the time required for raising the tank temperature from 25°C to 70°C when using single-phase flow is two hours and twenty-four minutes. Also, the gained energy from the tank is 848.42 W for two-phase flow 430.98 W for single-phase flow. The difference between the gained energy in both cases is approximately 417.44 W. This shows that two-phase flow is better than single-phase flow. Fig. 4.5-e illustrates the relationship between the average bulk temperature and tank temperature with time for single and two-phase flow. For single-phase flow, Part (e) shows that the temperature inside the tank is very close to the average bulk temperature. For two-phase flow, between 0 s to 1705 s, the average bulk temperature increases gradually with time, from 25.7°C to 40.4°C, while the tank temperature also increases gradually with time, from 22.9°C to 40.4°C, between 0 s to 1674.8 s.



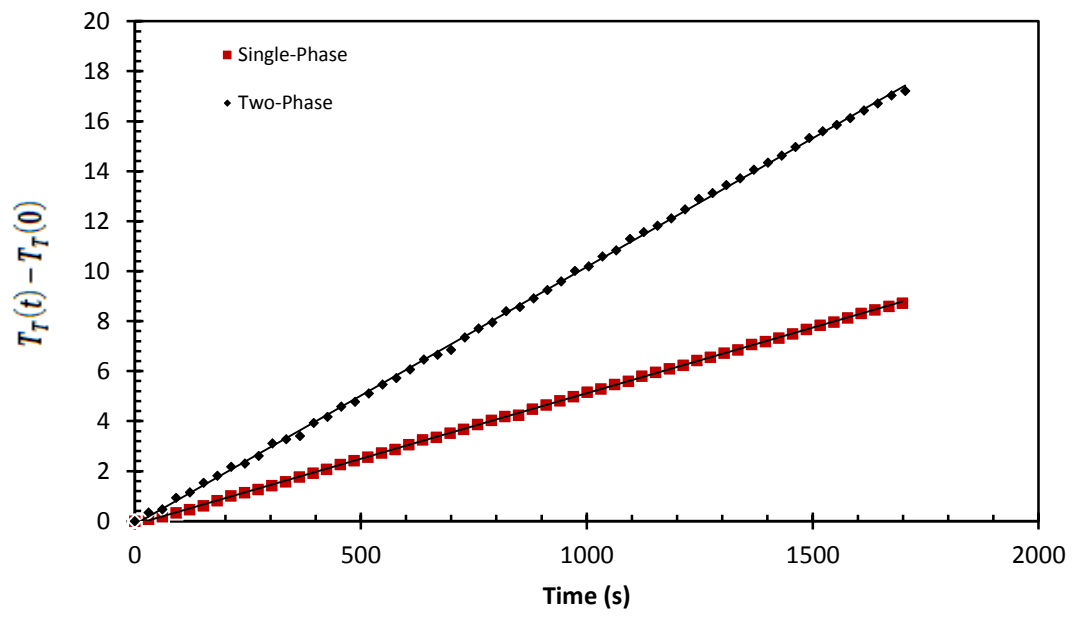
(a)



(b)



(c)



(d)

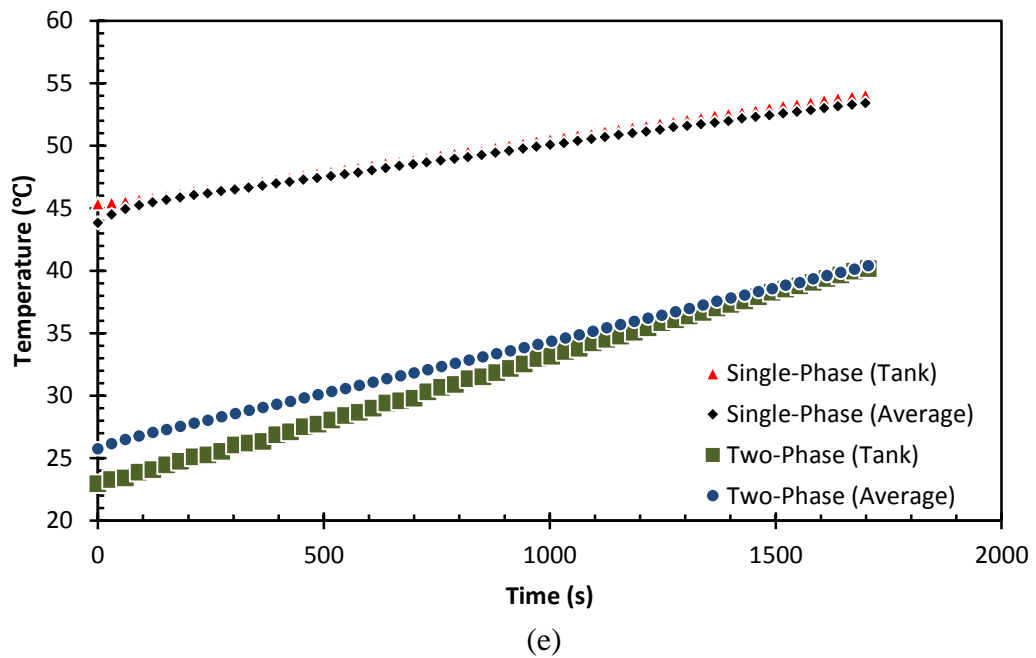
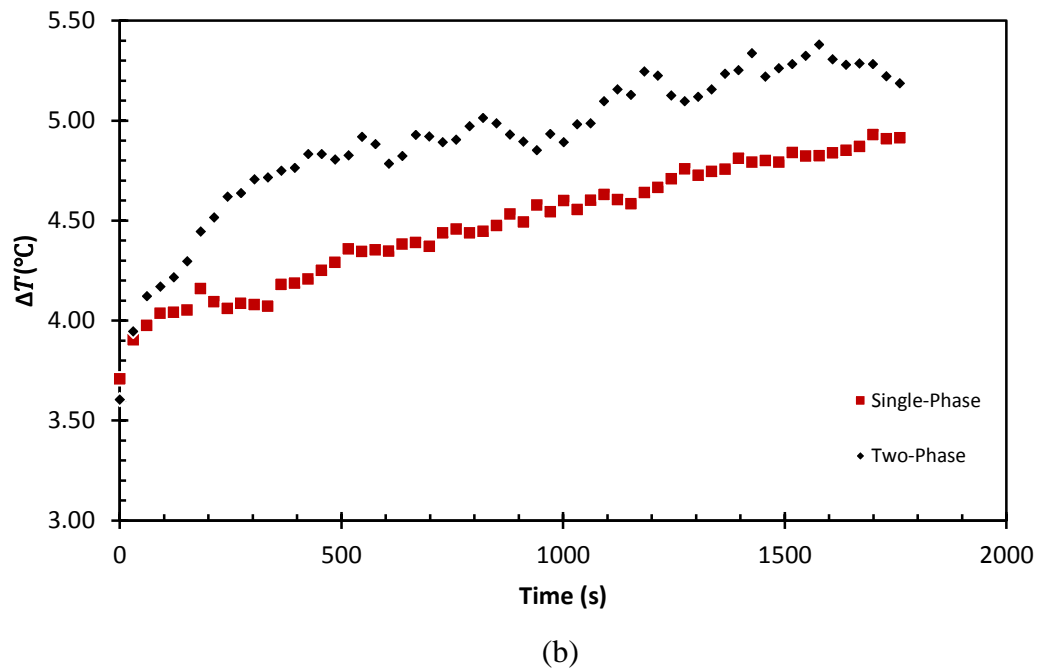
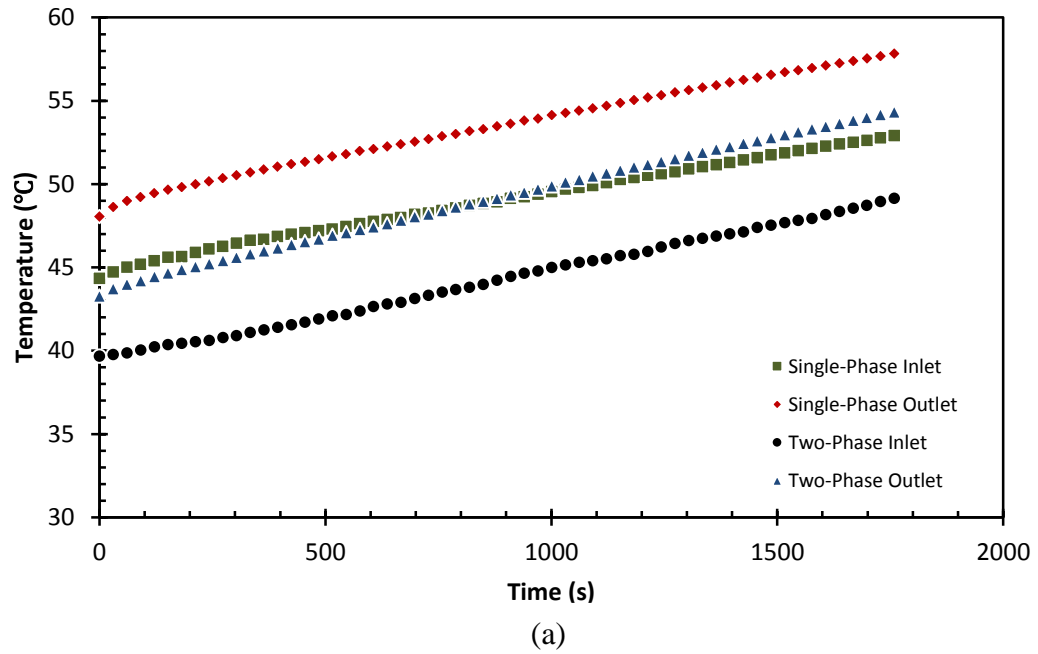


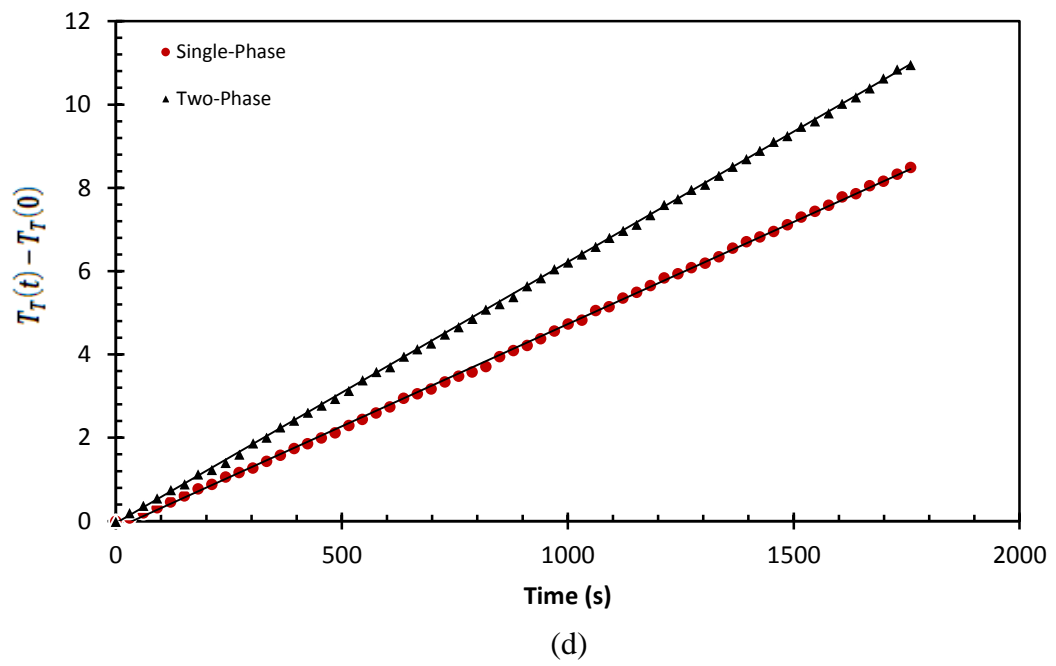
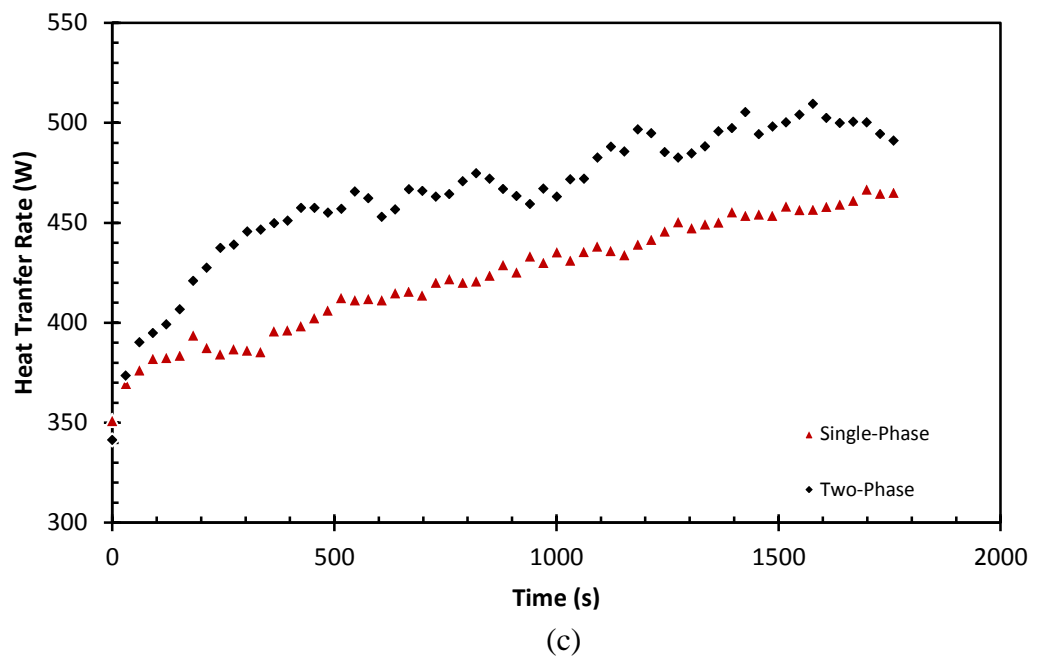
Fig.4.5. Transient thermal effectiveness at 1.7071 (L/min) for (a) inlet and outlet temperature, (b) temperature difference, (c) heat transfer rate, (d) temperature difference in the tank, and (e) average bulk and tank temperature.

The third experiment is also conducted with a constant flow rate, which is at 2.148 L/min. As can be noted from Fig. 4.6-a, the outlet temperature increases gradually from 48.1°C to 57.8°C for single-phase flow between 0 s and 1759 s and from 0s to 1759s the outlet temperature increases gradually with time, from 43.3 °C to 54.3°C, for two-phase flow. Also, from 0 s to 1759 s the inlet temperature rises gradually from 43.3°C to 52.9°C for single-phase flow and there is a slight increase in inlet temperature from 39.7°C to 49.2°C for two-phase flow between 0 s to 1759 s. Furthermore, it should be noted that the difference between the inlet and outlet temperature (ΔT) in both cases, single and two-phase, is fairly constant during the experiment, with an average value of 5.28°C and 4.85°C for two-phase and single-phase flow, respectively. Also, there is a significant increase in temperature difference from 3.6°C to 4.9°C for two-phase flow between 0 s to 546 s. Between 546 s and 1759 s the temperature difference increases with time and the temperature difference for two-phase flow fluctuates widely during the experiment. For single-phase flow, from 0 s to 181 s there is a sudden increase in temperature difference from 3.7°C to 4.15°C and the temperature difference increases gradually with time from 4.2°C to 4.9°C between 181s and 1759s. Thus, Fig. 4.6-b

shows that the temperature difference for two-phase flow is higher than the temperature difference for single-phase flow, with an average value of 5.28°C and 4.85°C for two-phase and single-phase flow, respectively. Also, the difference between temperature difference for both cases (ΔT_{total}) is approximately 1.09°C. Fig. 4.6-c shows the relationship between the heat transfer rate with time for single and two-phase flow, and that there is a significant increase in the heat transfer rate from 341.3 W and 457.5 W for two-phase flow between 0 s and 455 s. From 455 s to 1759 s, the rate of heat transfer rises gradually with time and the heat transfer rate went up and down widely during the experiment. For single-phase flow, there are dramatic increases in the heat transfer rate from 351.2 W to 406.72 W between 0 s and 151, while there is a gradual increase in the heat transfer rate from 406.72 W to 465.3 W between 151s and 1759s. Thus, Part (c) illustrates that the heat transfer rate for two-phase flow is higher than the heat transfer rate for single-phase flow, with an average value of 523.27 W and 459.09 W for two-phase and single-phase flow, respectively. The difference between the heat transfer rate for two and single-phase flow is approximately 64.18 watts. The heat transfer enhancement of two-phase flow is 1.14. Also, Fig. 4.6-d illustrates the relationship between the tank temperatures in both cases when the flow rate is 2.148 L/min. The tank temperature increases gradually with time for single and two-phase flow. The tank temperature for two-phase flow is higher than the tank temperature for single-phase flow, which causes the tank temperature slope for two-phase flow to be greater than the tank temperature slope for single-phase flow, with a value of $22.7 \frac{^{\circ}\text{C}}{\text{h}}$ and $17.8 \frac{^{\circ}\text{C}}{\text{h}}$ for two-phase and single-phase flow, respectively. Furthermore, the time required for heating the tank temperature from 25°C to 70°C for two-phase flow is approximately one hour and fifty-four minutes, while the time required for raising the temperature from 25°C to 70°C for single-phase flow is also approximately two hours and thirty minutes. Thus, the obtained energy from the tank for two-phase flow is approximately 512.21 W and for single-phase flow is approximately 401.65 W. The difference between the obtained energy in both cases is 110.56 w. This shows that the two-phase system is better than the single-phase system. Fig. 4.6-e illustrates the relationship between the average bulk temperature and tank temperature with time for single and two-phase flow. In this experiment, it can be seen in Part (e) that the amount of change in average bulk

temperature is close to the amount of change in the temperature inside the tank for single and two-phase flow.





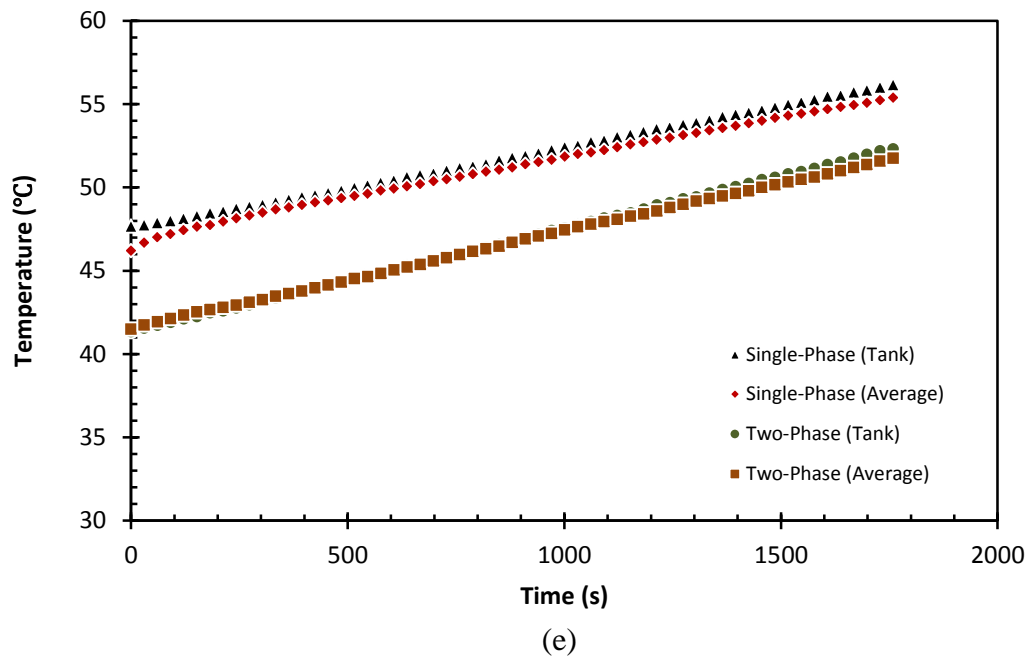


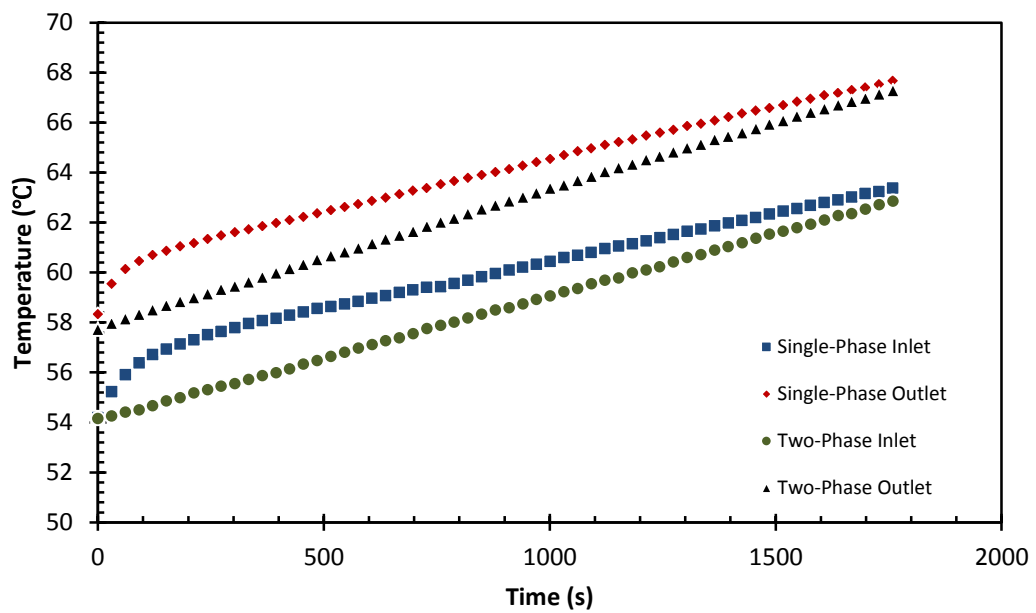
Fig.4.6. Transient thermal effectiveness at 1.7071 (L/min) for (a) inlet and outlet temperature, (b) temperature difference, (c) heat transfer rate, (d) temperature difference in the tank, and (e) average bulk and tank temperature.

The flow rate in the fourth experiment is 2.987 L/min. Fig. 4.7-a illustrates that there is a sudden increase in the outlet temperature for single-phase flow from 57.7°C to 60.1°C between 0 s and 60 s. From 60 s to 1759 s there is a gradual increase in outlet temperature from 60.1°C to 67.3°C. Between 0 s and 121 s the inlet temperature rises significantly from 54.2°C to 56.7°C and between 121 s and 1759 s the inlet temperature increases gradually from 56.7°C to 62.9°C. For two-phase flow, there is a gradual increase in the outlet temperature from 57.7°C to 67.3°C between 0 s and 1759 s and from 0 s to 1759.5 s there is a significant increase in inlet temperature from 54.2°C to 62.9°C. Part (a) shows that the difference between inlet and outlet temperature (ΔT) is relatively stable over the experiment, with a value of 4.45°C and 4.27°C for two-phase and single-phase flow, respectively. Furthermore, Fig. 4.7-b shows that there is a strange relationship between temperature difference and time at the beginning of the experiment for single-phase flow because the experiment took time to stabilize. This period is identified between 0 s and 333 s and after the period the temperature difference for single-phase flow increases gradually from 3.8°C to 4.3°C between 333 s and 1758 s. For two-phase flow, from 0 s to 1759 s there is also a gradual increase in temperature

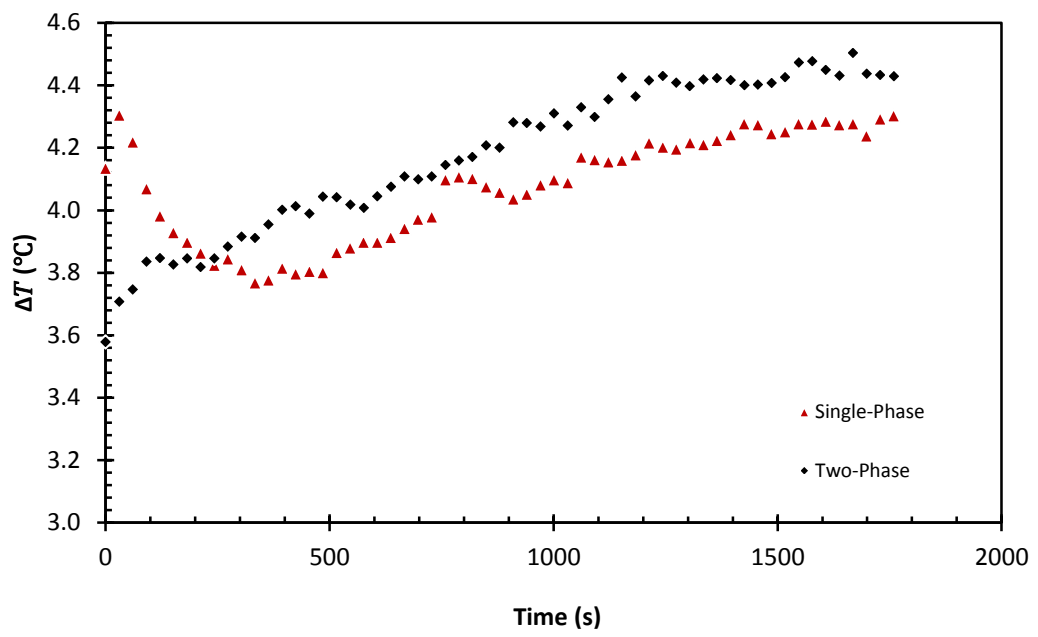
difference from 3.6°C to 4.4°C for two-phase flow. Thus, the temperature difference for two-phase flow is higher than the temperature difference for single-phase flow, with an average value of 4.45°C and 4.27°C for two-phase flow and single-phase flow, respectively. The difference between temperature difference in both cases is approximately 1.04°C. Fig.4.7-c shows the relationship between the rate of heat transfer with the time for single and two-phase flow. Between 0 s and 30 s, the heat transfer rate for single-phase flow increases with time and from 30 s to 333 s there is a drop of 72 W in the heat transfer rate due to a stabilization period. Between 333 s and 1758 s, there is a gradual increase in the heat transfer rate from 503.8 W to 575.3 W. For two-phase flow, the heat transfer rate increases gradually from 478.5 W to 592.1 W between 0 s to 1759 s. Thus, Part (c) illustrates that the heat transfer rate for two-phase flow is higher than the heat transfer rate for single-phase flow, with an average value of 604.4 W and 571.19 W for two-phase and single-phase flow, respectively. The difference between the heat transfer rate for single and two-phase is approximately 33.21 W. The heat transfer enhancement of two-phase flow is 1.06. Fig. 4.7-d shows the relationship between the tank temperature with time for single and two-phase flow. In the period between 0 s and 1759 s there is a gradual increase in tank temperature with time in for single and two-phase flow. The tank temperature slope for two-phase flow is greater than the tank temperature slope for single-phase flow, with a value of $20.5 \frac{^{\circ}\text{C}}{\text{h}}$ and $14.3 \frac{^{\circ}\text{C}}{\text{h}}$ for two-phase and single-phase flow, respectively. The likely cause is that the tank temperature for two-phase flow is higher than the tank temperature for single-phase flow. Thus, the time required for raising the tank temperature from 25°C to 70°C for two-phase flow is approximately two hours and eleven minutes and for single-phase flow it is also approximately three hours and six minutes. Also, Part (b) shows that the obtained energy from the tank for two-phase flow (\dot{E}_{TP}) is higher than the obtained energy from the tank for single-phase flow, with a value of 462.57 W and 322.67 W for two-phase and single-phase flow, respectively. This shows that the two-phase flow system is better than the single-phase flow system. Fig. 4.7-e illustrates the relationship between the average bulk temperature and tank temperature with time for single and two-phase flow. For single-phase flow, the temperature inside the tank increases gradually from 56.3°C to 66.6°C from 0 s to 1758.9 s, while the average bulk temperature

also rises gradually from 56.3°C to 65.5°C between 0 s to 1758.9 s. The temperature inside the tank is higher than the average bulk temperature, with an average value of 63.1°C and 61.9°C for the tank and average bulk temperature, respectively. For two-phase flow, there is a gradual increase in the temperature inside the tank from 56.6°C to 66.5°C between 0 s and 1759.4 s, while the average temperature also increases gradually from 55.9°C to 65.1°C between 0 s to 1759.4 s. The tank temperature is higher than the average bulk temperature, with an average value of 61.6°C and 60.5°C for the tank and average bulk temperature, respectively.

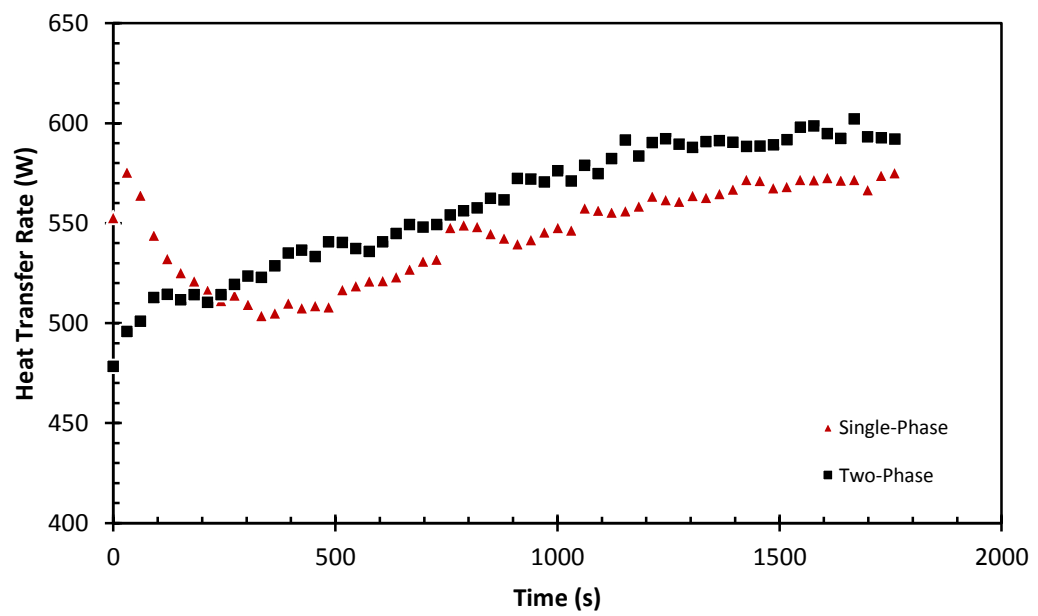
As illustrated in Figs. 4.4, 4.5, 4.6, and 4.7 the heat transfer rate enhancement of two-phase flow is better than single-phase flow due to the various internal circulations present in the slugs that eventually led towards a much greater radial rate of heat transfer, as well as an increased slug velocity.



(a)



(b)



(c)

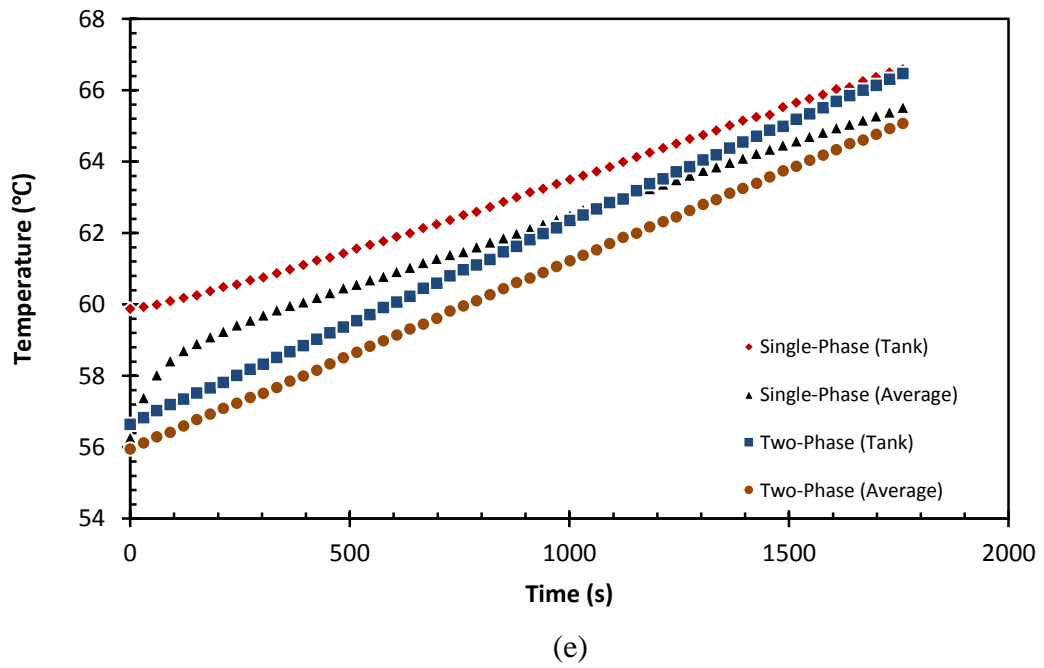
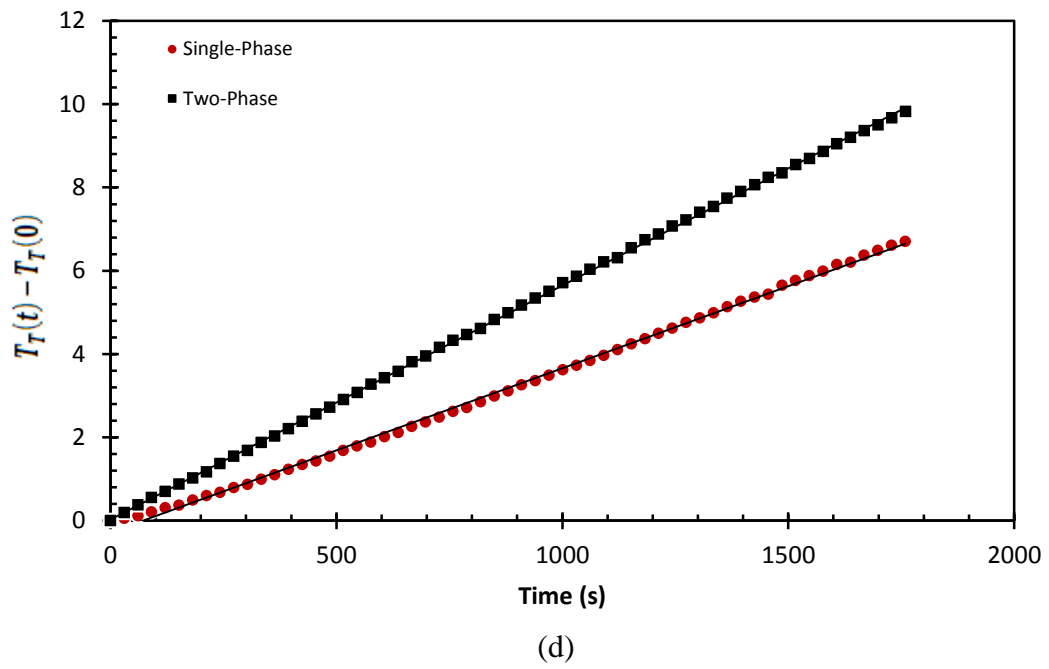


Fig.4.7. Transient thermal effectiveness at 2.987 (L/min) for (a) inlet and outlet temperature, (b) temperature difference, (c) heat transfer rate, (d) temperature difference in the tank, and (e) average bulk and tank temperature.

Table 4.2. Summary of single-phase (glycol) and two-phase flow (glycol-air) experiments.

Test	Type of Experiment	\dot{Q} (L/min)	\dot{m} (kg/s)	ΔT_c (°C)	$\frac{\Delta T}{\Delta t}$ ($\frac{^\circ\text{C}}{\text{h}}$)	Q_c (W)	\dot{E}_t (W)	Time to Heat Tank (25°C to 70°C)
1 _a	Single-Phase	0.649	0.0121	9.22	23.1	270.96	512.24	2
1 _b	Two-Phase	0.657	0.0122	10.06	34.7	298.23	782.9	1:18
2 _a	Single-Phase	1.702	0.0316	5.13	19.1	394.48	430.98	2:24
2 _b	Two-Phase	1.712	0.0318	5.19	37.6	401.06	848.42	1:12
3 _a	Single-Phase	2.068	0.0389	4.86	17.8	459.09	401.65	2:30
3 _b	Two-Phase	2.198	0.0408	5.28	22.7	523.27	512.21	1:54
4 _a	Single-Phase	2.963	0.0550	4.27	14.3	571.19	322.67	3:06
4 _b	Two-Phase	3.012	0.0559	4.45	20.5	604.57	462.57	2:12

Table 4.3. Experimental heat transfer enhancement of a two-phase flow solar collector

Test	Type of Experiment	\dot{Q} (L/min)	\dot{m} (kg/s)	ΔT_c (°C)	$\frac{\Delta T}{\Delta t}$ ($\frac{^\circ\text{C}}{\text{h}}$)	Q_c (W)	$Enh_{Two-Phase}$	% $Enh_{Two-Phase}$
1 _a	Single-Phase	0.649	0.0121	9.22	23.1	270.96	1.10	10
1 _b	Two-Phase	0.657	0.0122	10.06	34.7	298.23		
2 _a	Single-Phase	1.702	0.0316	5.13	19.1	394.48	1.01	1.67
2 _b	Two-Phase	1.712	0.0318	5.19	37.6	401.06		
3 _a	Single-Phase	2.068	0.0389	4.86	17.8	459.09	1.14	14
3 _b	Two-Phase	2.198	0.0408	5.28	22.7	523.27		
4 _a	Single-Phase	2.963	0.0550	4.27	14.3	571.19	1.06	5.8
4 _b	Two-Phase	3.012	0.0559	4.45	20.5	604.57		

4.5 Experiments at Variable Liquid Void Fraction

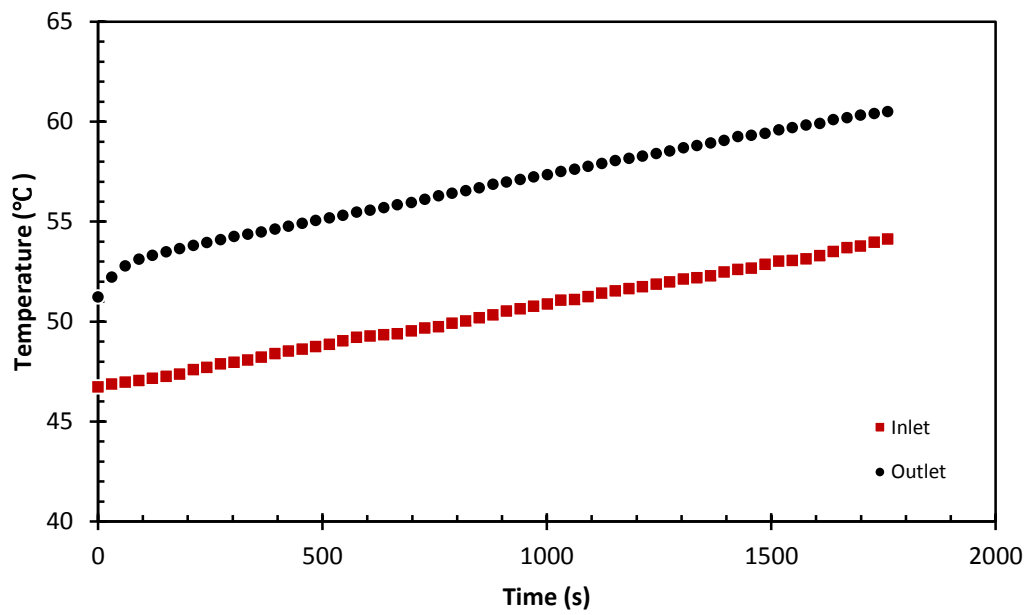
The four experiments for two-phase flow are conducted with different liquid length (L_l) and air plug length (L_g), as well as one experiment for single-phase. All these experiments are also conducted with the same flow rate, which is approximately 1.3 L/min.

Table 4.4. Summary of Experiments at Variable Liquid Void Fraction.

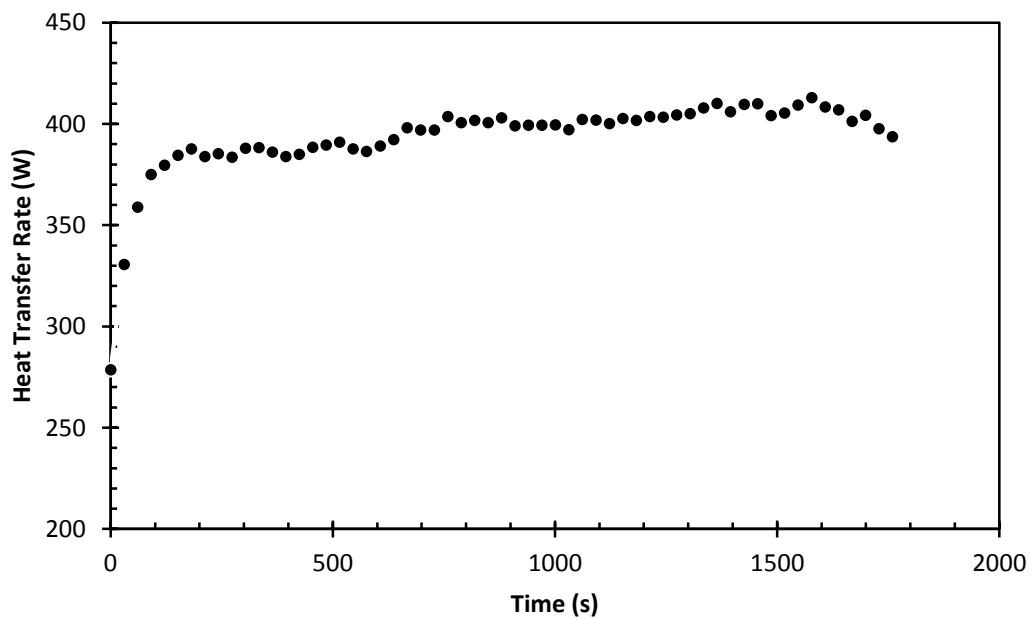
Test	Type of Experiment	\dot{Q} (L/min)	\dot{m} (kg/s)	L_l (cm)	L_g (cm)	α_l	ΔT_c (°C)	Q_c (W)
1	Two-Phase	1.368	0.02542	9.7	2.5	0.79	6.38	393.72
2	Two-Phase	1.306	0.02426	4.7	4.5	0.51	6.96	410.20
3	Two-Phase	1.369	0.02543	9.7	4.9	0.66	6.68	412.87
4	Two-Phase	1.331	0.02473	5	5.2	0.5	7.09	425.50
5	Single-Phase	1.302	0.0242	0	1	5.91	347.55

The liquid void friction (α_l) for the first experiment is 0.79 and the flow rate (\dot{Q}) is 1.368 (L/min). Fig. 4.8-a shows the relationship between inlet and outlet temperature with time. From 0 s to 60 s, the outlet temperature for two-phase flow increases from 51.2°C to 52.8°C, and between 60 s to 1759.6 s there is a gradual increase in outlet temperature from 52.8°C to 60.5°C. Between 0 s and 1759.6 s the inlet temperature rises gradually from 46.7°C to 54.1 °C. As can be seen from Part (a), the outlet temperature is higher than the inlet temperature, with average values of 60.50°C and 54.12°C for the outlet and inlet temperature, respectively. The difference between inlet and outlet (ΔT) temperature remains constant during the experiment, with an average value of 6.38°C. Fig. 4.8-b illustrates the relationship between the heat transfer rate (Q) and the time when the liquid void friction is 0.79, with a flow rate of 1.368 L/min. The heat transfer rate increases from 278.6 W to 384.6 W between 0 s and 151.6 s. Between 151.6 s to 1577.7 s, the heat transfer rate rises slowly from 384.6 W to 413 W. Between 1577.7 s to 1759.6 s the heat transfer rate goes down, due to the fact that thermal loss occurs in the insulated pipe. The rate of heat transfer (Q) during the experiment is approximately 393.72 W. Fig.4.8-c illustrates the transient relationship between average bulk temperature ($\overline{T_b}$) and tank temperature (T_{Tank}) for two-phase flow, when the liquid

void fraction is 0.79 and flow rate is 1.368 L/min. In this experiment, it can be seen in Part (c) that the temperature inside the tank rises gradually from 50.2°C to 57.9°C between 0 s to 1759.6 s, while there is a gradual increase in average bulk temperature from 48.9 °C to 57.3°C between 0 s to 1759.6 s. Part (c) illustrates that the tank temperature is higher than the average bulk temperature, with an average value of 54.04°C and 53.54°C for the tank and average bulk temperature, respectively. The difference between the tank and average bulk temperature is approximately 0.5°C.



(a)



(b)

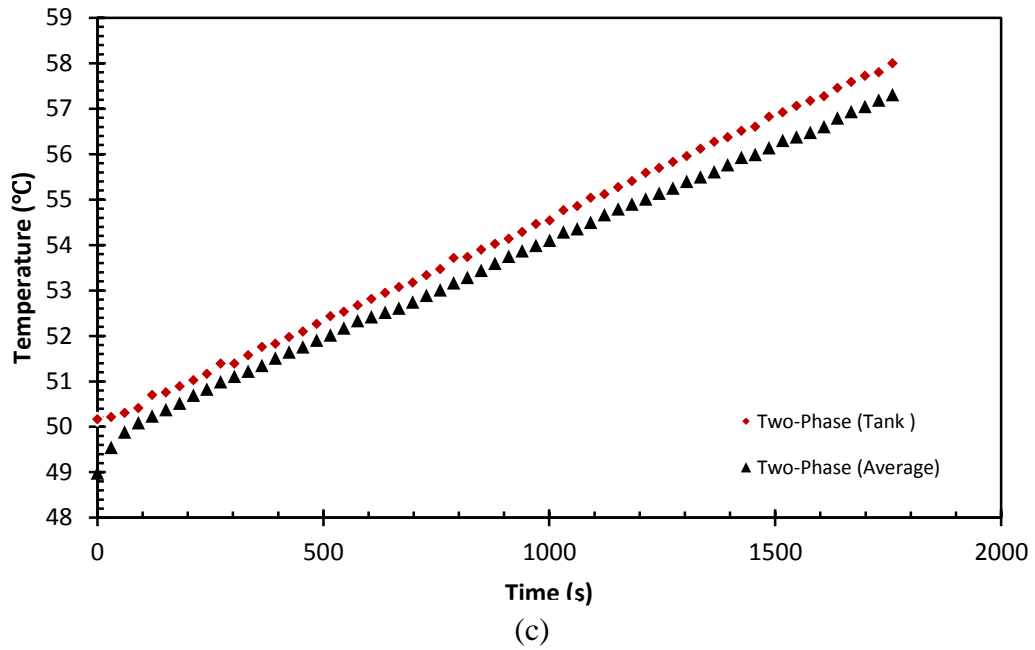
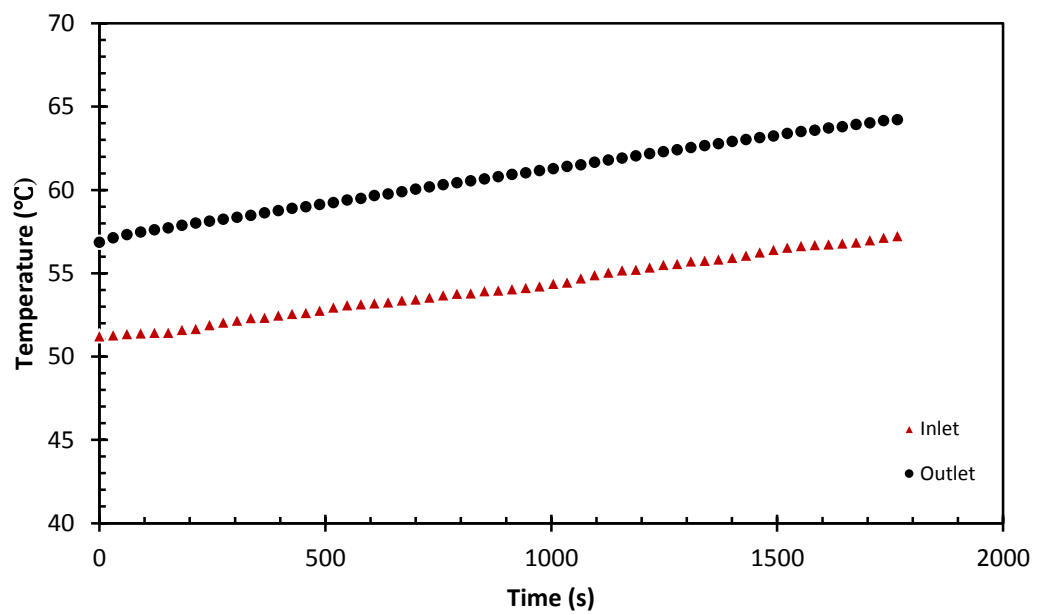


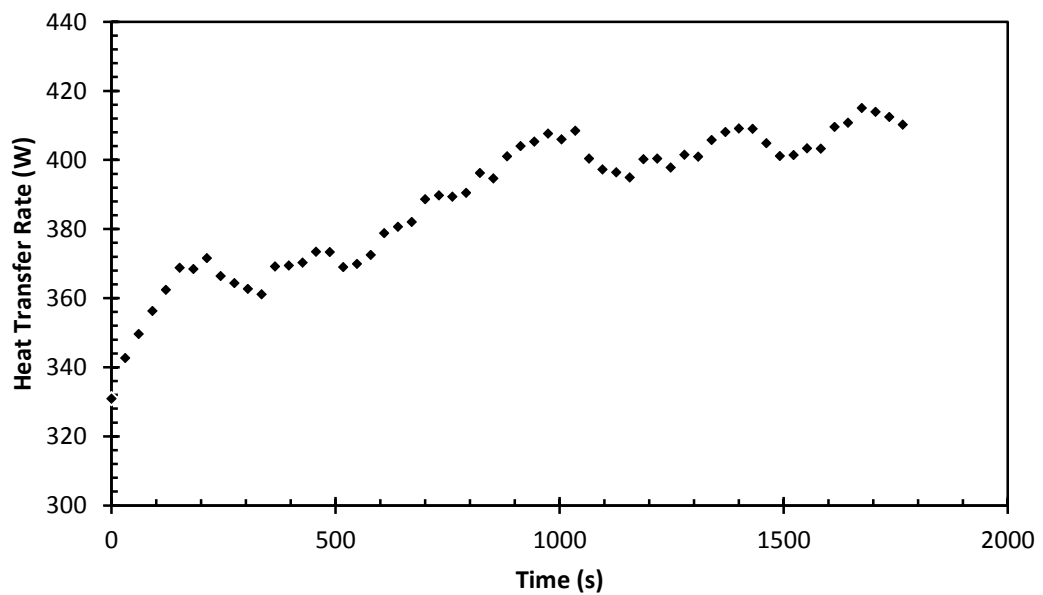
Fig.4.8. Transient thermal effectiveness for two-phase flow at 1.368 (L/min) and liquid void fraction of 0.79 for (a) inlet and outlet temperature, (b) heat transfer rate, and (c) average bulk and tank temperature.

The flow rate in the second experiment (\dot{Q}) is 1.306 L/min and the liquid void fraction (α_l) is 0.51. Fig. 4.9-a illustrates the transient relationship between inlet and outlet temperature. There is a gradual increase in outlet temperature from 56.9°C to 64.2°C between 0 s to 1766.1 s, and the outlet temperature for two-phase flow increases from 51.2°C to 52.8°C between 60 s to 1759.6 s. The inlet temperature for this experiment increases slowly from 51.2°C to 57.3°C between 0 s to 17766.1 s. Also, Part (a) shows that the outlet temperature is greater than the inlet temperature, with an average value of 64.23°C and 57.27°C for outlet and inlet temperature, respectively. The temperature difference (ΔT_2) for this experiment is higher than the temperature difference for the first experiment (ΔT_1), with an average value of 6.96°C and 6.38°C for the second and first experiment, respectively. The temperature difference between the first and second experiment is 1.09°C. Fig.4.9-b shows the relationship between the heat transfer rate and time when the liquid void fraction is 0.51 and flow rate is 1.306 L/min. There is a gradual increase in the rate of heat transfer from 330.9 W to 410.257 W between 0 s and 1766.1 s. The heat transfer rate for this experiment is higher than the heat transfer rate for the first experiment, with average values of 410.25 W and 393.72 W for the second and first experiment, respectively. Part (b) illustrates the transient relationship

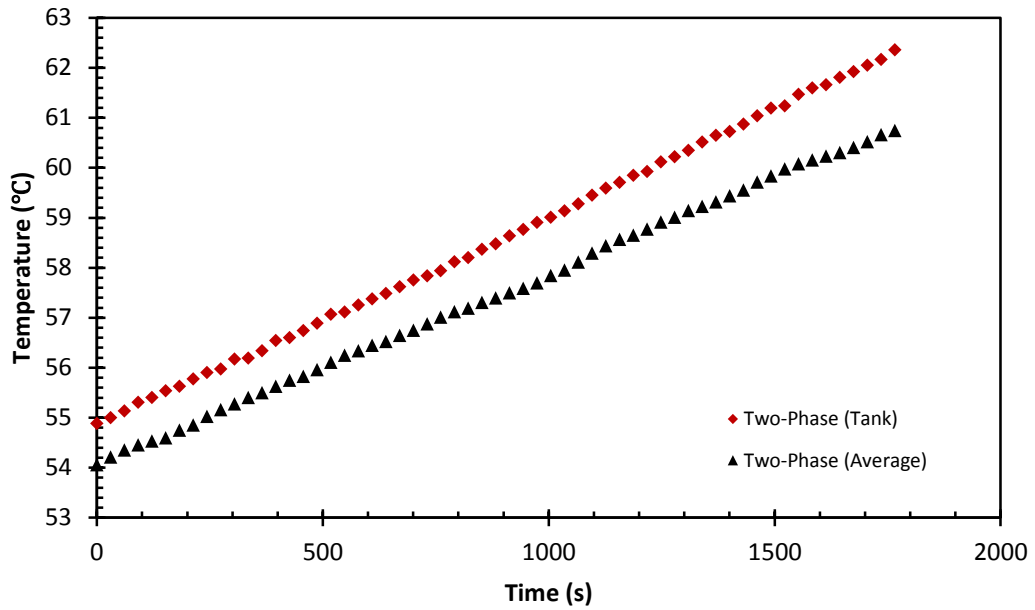
between the average bulk temperature and tank temperature when the liquid void friction is 0.51 and flow rate is 1.306 L/min. It can be seen in Fig.4.9-c that the temperature inside the tank increases gradually from 54.8°C to 62.4°C between 0 s to 1766.1 s. Also, there is a gradual increase in average bulk temperature from 54.1°C to 60°C between 0 s to 1766.1 s. Part (c) illustrates that the tank temperature is higher than the average bulk temperature, with an average value of 58.56°C and 57.46 °C for the tank and average bulk temperature, respectively. The difference between the tank and average bulk temperature is approximately 1.1°C.



(a)



(b)

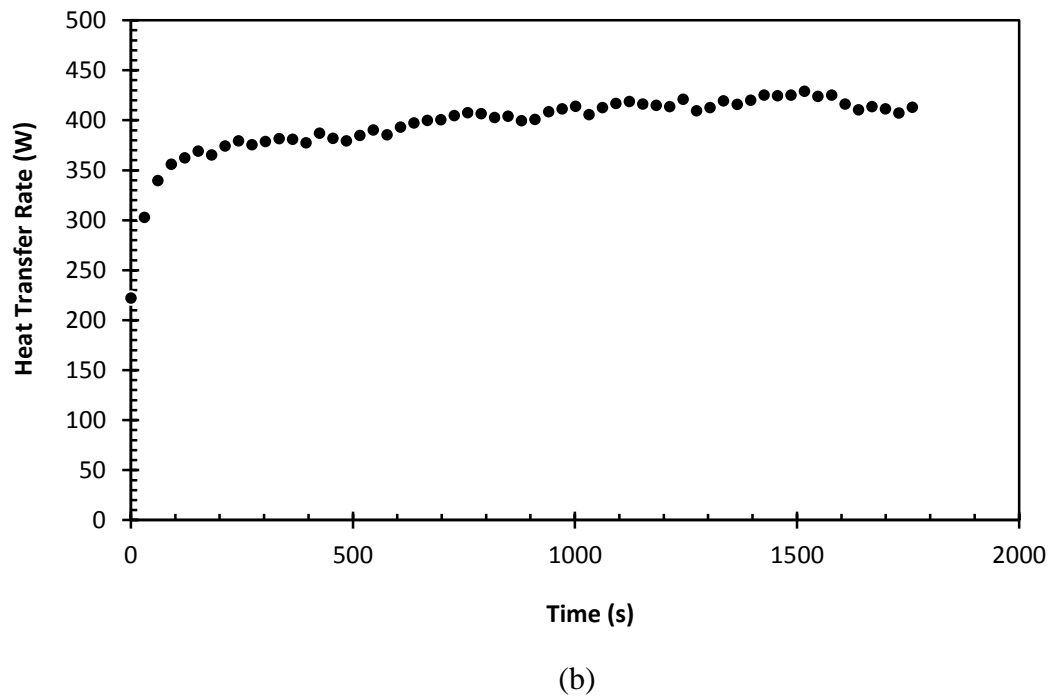
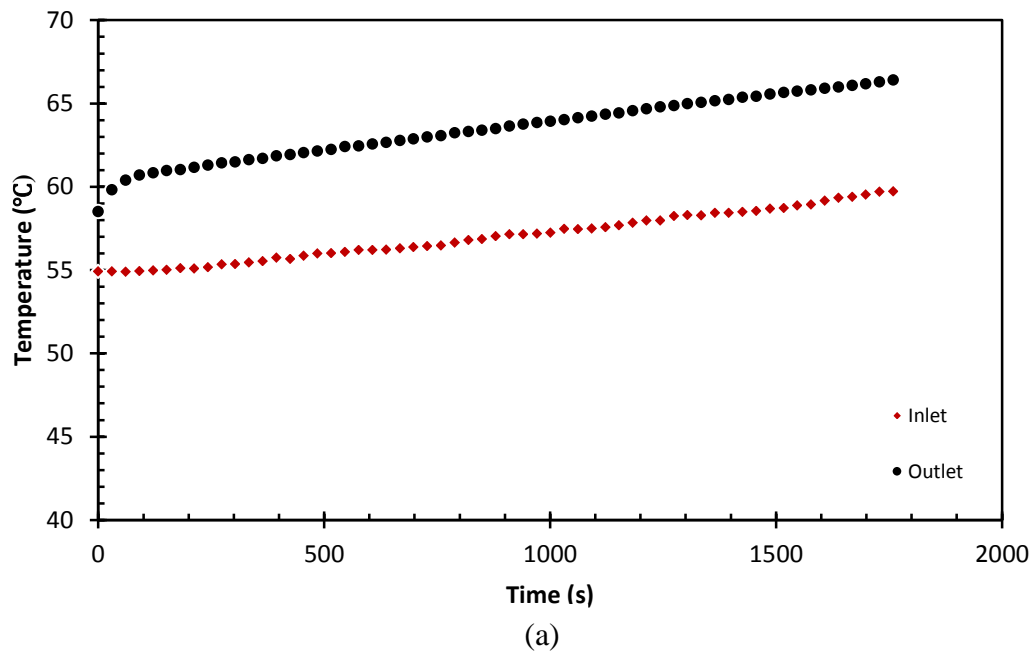


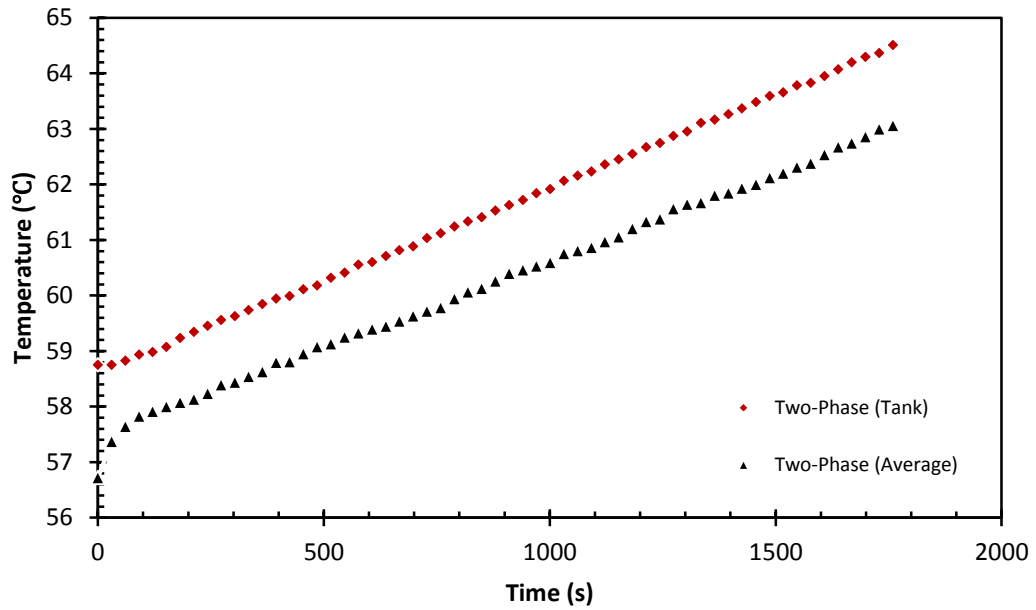
(c)

Fig.4.9. Transient thermal effectiveness for two-phase flow at 1.306 (L/min) and liquid void fraction of 0.51 for (a) inlet and outlet temperature, (b) heat transfer rate, and (c) average bulk and tank temperature.

The third experiment is conducted when the liquid void fraction (α_l) is 0.66 and flow rate is 1.369 L/min. Fig.4.10-a shows the transient relationship between inlet and outlet temperature. From 0 s to 30 s, the outlet temperature increases from 58.5°C to 59.8°C and between 30 s to 1759.5 s there is a gradual increase in outlet temperature from 59.8°C to 66.4°C. Between 0 s and 1759.6 s the inlet temperature rises slowly from 54.9°C to 59.7°C. As can be seen from Part (a) the difference between inlet and outlet (ΔT) temperature remains constant during the experiment, with a value of 6.68°C. Fig. 4.10-b illustrates the relationship between the heat transfer rate and time when the liquid void fraction is 0.66 and flow rate is 1.369 L/min. The heat transfer rate increases from 222.1 W to 339.8 W between 0 s and 60 s and between 60 s to 1516.8 s the heat transfer rate rises slowly from 339.7 W to 428 W. Between 1516.8 s to 1759.4 s the heat transfer rate decreases due to the fact that the loss occurs in an insulated pipe. The heat transfer rate during the experiment is approximately 412.87 W. Part (b) illustrates the transient relationship between average bulk temperature and tank temperature when the liquid void fraction is 0.66 and flow rate is 1.369 L/min. It can be seen in Fig. 4.10-c that there is a gradual increase in the temperature inside the tank, from 58.7°C to 64.5°C, between 0 s to 1759.5 s. Also, there is an increase in average bulk temperature from 56.7 °C to

57.6°C between 0 s to 60 s and between 60 s to 1759.5 s the average bulk temperature increases gradually from 57.6°C to 63.1°C. Part (c) illustrates that the tank temperature is higher than the average bulk temperature, with an average value of 61.54°C and 60.24 °C for the tank and average bulk temperature, respectively. The difference between the tank and average bulk temperature is approximately 1.3°C.



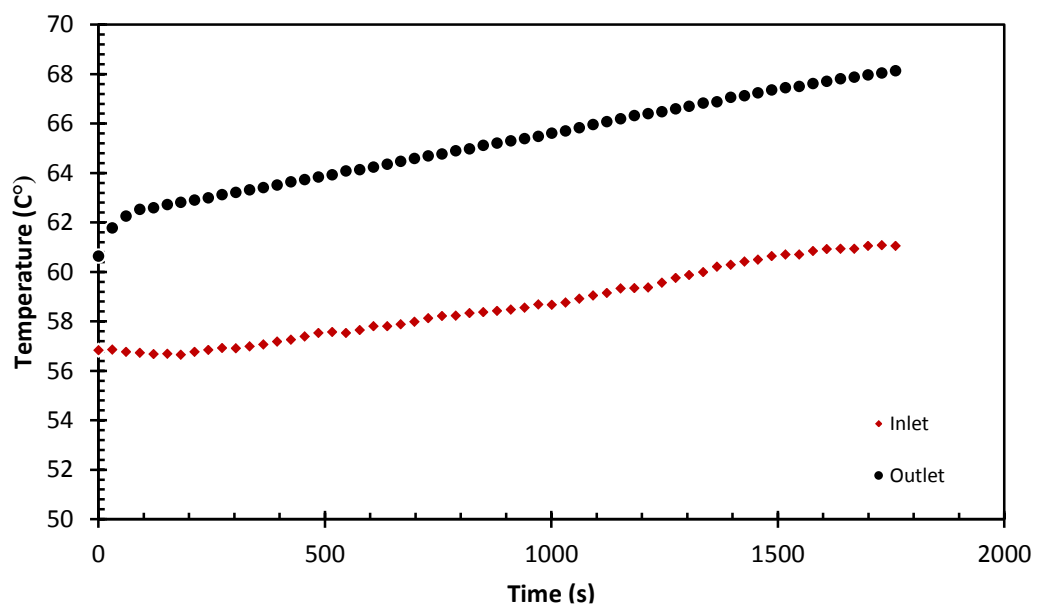


(c)

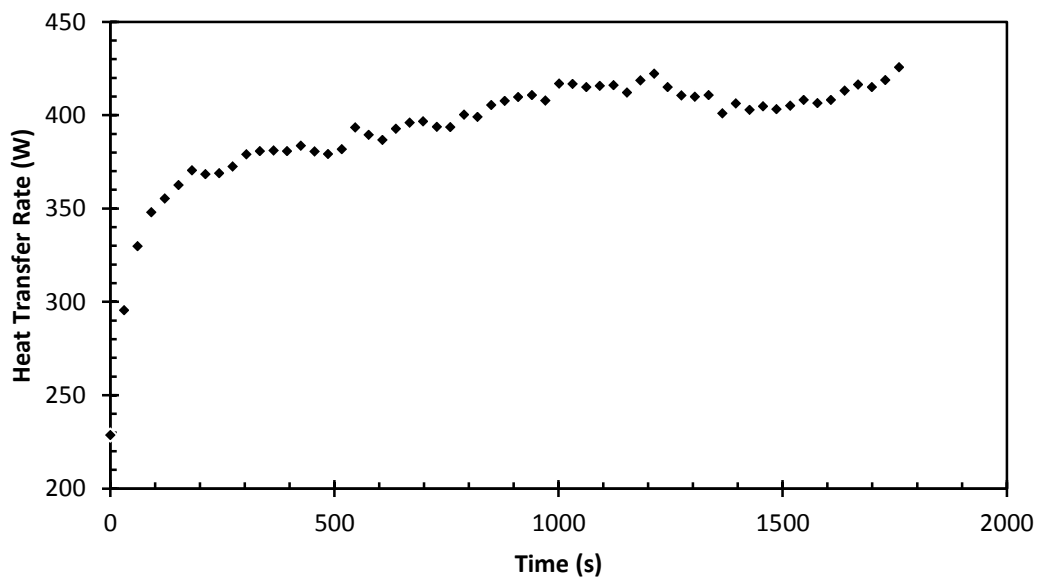
Fig.4.10. Transient thermal effectiveness for two-phase flow at 1.369 (L/min) and liquid void fraction of 0.66 for (a) inlet and outlet temperature, (b) heat transfer rate, and (c) average bulk and tank temperature.

The liquid void fraction (α_l) for the fourth experiment is 0.5 and the flow rate is 1.331 L/min. Fig. 4.11-a shows the transient relationship between inlet and outlet temperature. From 0 s to 60 s, the outlet temperature for two-phase flow increases from 60.6°C to 62.3°C and between 60 s to 1759.4 s there is a gradual increase in outlet temperature from 62.3°C to 68.1°C. Between 0 s and 1759.4 s the inlet temperature rises gradually from 56.8°C to 61.1°C. As can be seen from Part (a), the difference between inlet and outlet (ΔT) temperature remains constant during the experiment, with an average value of 7.09°C. Fig. 4.11-b illustrates the relationship between the heat transfer rate and time when the liquid void fraction is 0.5 and flow rate is 1.331 L/min. The heat transfer rate increases from 228.6 W to 370.3 W between 0 s and 181.9 s and between 181.9 s to 1182.9 s the heat transfer rate rises slowly from 370.3 W to 418.54 W. Between 1182.9 s to 1486.4 s the heat transfer rate decreases from 418.5 W to 403.0 W due to the fact that the loss occurs in an insulated pipe. The heat transfer rate starts to increase gradually from 403 W to 425.5 W between 1486.4 s to 1759.4 s. Part (b) illustrates that the heat transfer rate during the experiment is approximately 425.49 W. Fig. 4.11-c illustrates the transient relationship between average bulk temperature and tank temperature when the liquid void fraction is 0.5 and flow rate is 1.331 L/min. It can be seen in Part (c) that

the temperature inside the tank increases gradually from 60.8°C to 66.7°C between 0 s to 1759.5 s. Also, there is an increase in average bulk temperature from 58.7 °C to 59.5°C between 0 s to 60, and from 60 s to 1759.5 s the average bulk temperature increases gradually from 59.5°C to 64.6°C. Part (c) illustrates that the tank temperature is higher than the average bulk temperature, with an average value of 63.60°C and 61.91 °C for the tank and average bulk temperature, respectively. The difference between tank and average bulk temperature is approximately 1.69°C.



(a)



(b)

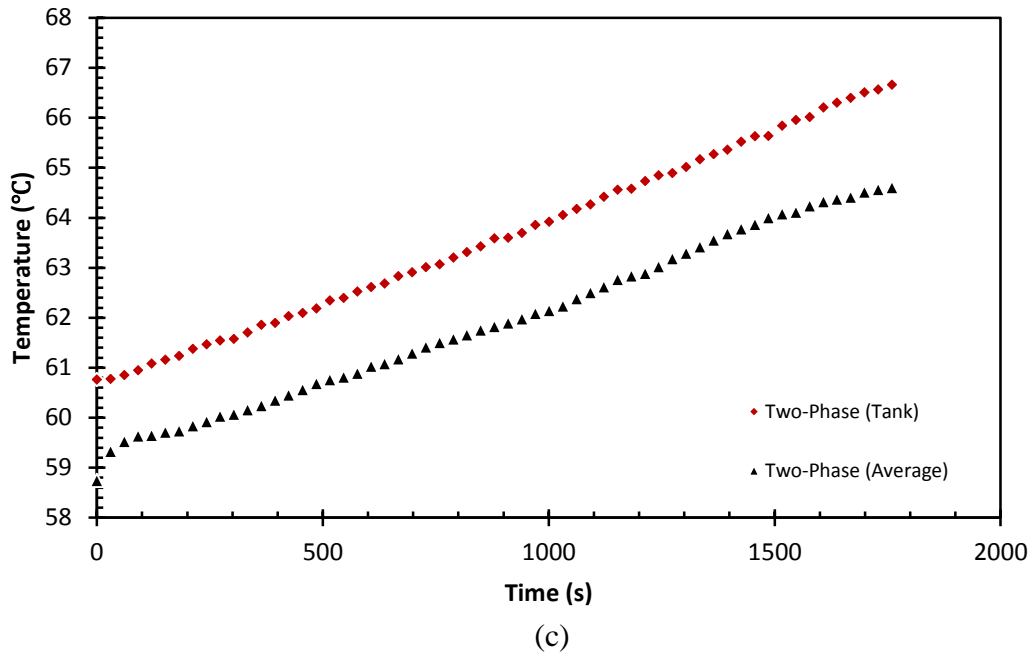


Fig.4.11. Transient thermal effectiveness for two-phase flow at 1.331 (L/min) and liquid void fraction of 0.5 for (a) inlet and outlet temperature, (b) heat transfer rate, and (c) average bulk and tank temperature.

The sixth experiment is single-phase used to compare with the results of the two-phase experiments. The flow rate is 1.302 L/min and the liquid void fraction (α_l) is 1 unit. As can be seen from Table 4.5, the difference between inlet and outlet (ΔT) temperature remains constant during the experiment, with a value of 5.91°C. As presented in Table 4.5, the heat transfer rate during the experiment is approximately 347.55 Watts. This shows that the two-phase flow system is better than the single-phase flow system.

Fig. 4.12 and Fig. 4.13 show the transient relationship between two-phase tank temperature at a different flow rate and different liquid void fraction(α_l). The tank temperature in all experiments increases gradually. The tank temperature increases more quickly when the flow rate is 0.657 L/min and slower when the flow rate is 3.012 L/min. As illustrated in Fig. 4.13, the largest increase in temperature inside the tank occurs when the liquid void fraction is 0.79, while the lowest increase in temperature occurs when the liquid void fraction is 0.66.

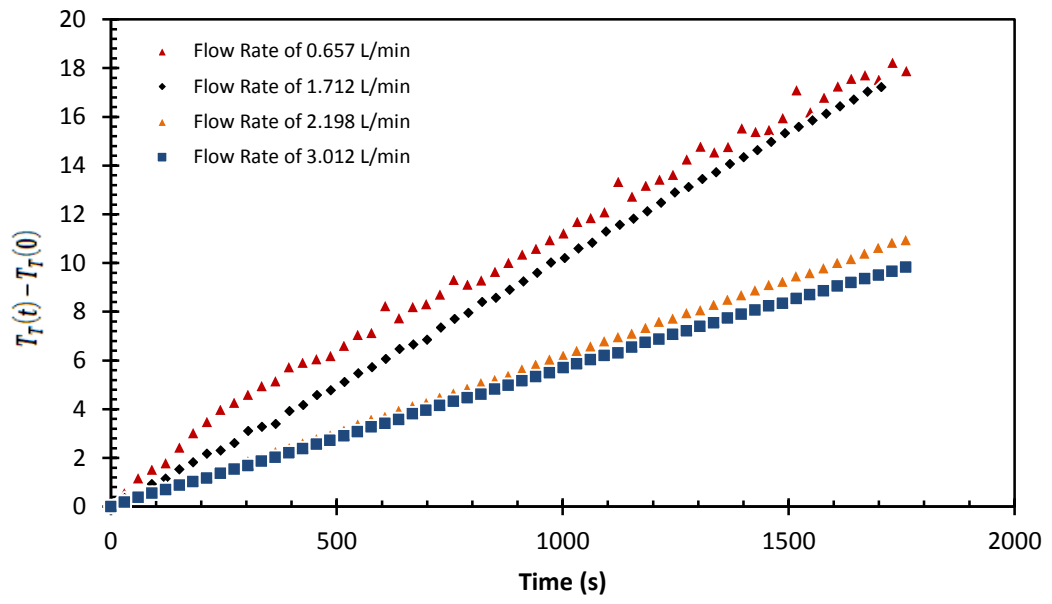


Fig.4.12. Transient tank temperature at different two-phase flow rate

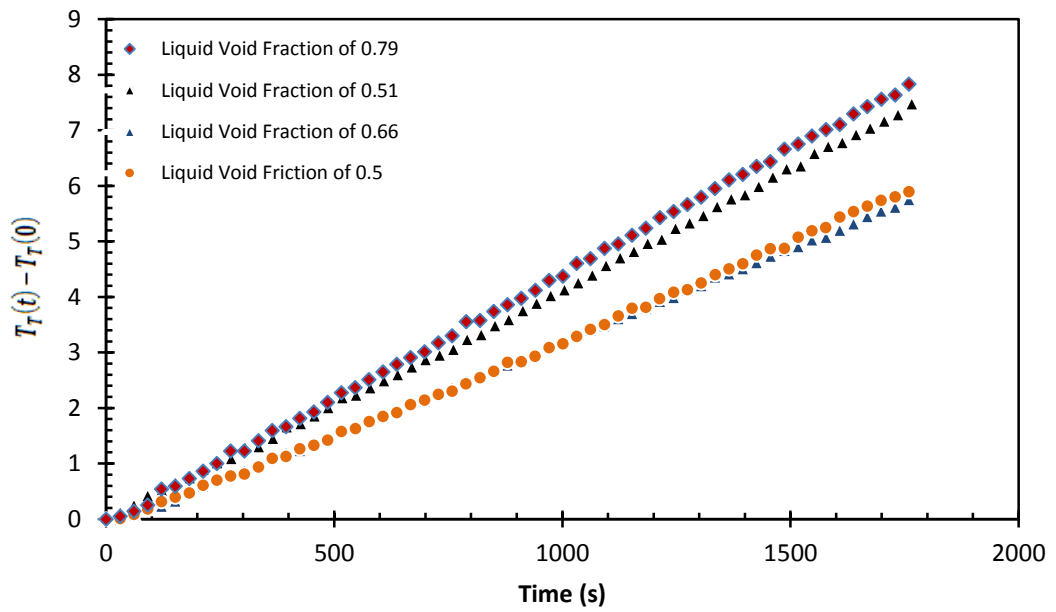


Fig.4.13. Transient tank temperature at different liquid void fractions

Chapter 5

Conclusion and Recommendations

5.1 Conclusion of Present study

The present study is used to examine two-phase segmented flow as a working fluid in a solar thermal collector. An introduction to this study included the definition and applications of two-phase flow, flow patterns in two positions, vertical and horizontal positions and types of solar water heating systems. The literature related to two-phase segmented flow was presented. The mechanism of heat transfer enhancement and the heat transfer coefficient in internal flow were illustrated. Next, the basic relations in two-phase flow, important dimensionless numbers, and a pressure drop that occurred in the pipe were presented. The system configuration was also shown. Finally, the experimental results were presented.

The results from single-phase flow were compared to two-phase segmented flow. The results illustrated that the heat transfer rate and the temperature difference between the entrance and exit of the solar thermal collector for two-phase flow were higher than for single-phase flow. Also, the experimental results showed that the time required for heating the temperature inside the tank from 25°C to 70°C for two-phase flow was less than for single-phase flow. Also, the obtained energy in the tank for two-phase flow was greater than for single-phase flow. Four experiments at equivalent flow rates were conducted to examine the effects of liquid void fraction. The results of these experiments showed that the heat transfer rate was highest when the liquid length was 5 cm and air plug length was 5.2 cm. The heat transfer rate was lowest when the liquid length was 9.7 cm and air plug length was 2.5 cm.

5.2 Recommendations for Future Work

To improve two-phase segmented flow as a working fluid in solar thermal collectors there are some modifications that must be made.

- i) The size of the tube was a little large, which led to air bubbles not occupying the full diameter of the tube. The reason was that the air that entered the flow loop was not sufficient, so the effect of gravity was considerable.
- ii) The compressor was adjusted to give maximum output pressure, with a value of 125 psi, and then the compressor switched off. The minimum output pressure was also adjusted at 75 psi. When the compressor reached this value, the compressor began to charge again. The experiment was initiated when the maximum output pressure was 152 psi, but after a few minutes the pressure inside the compressor decreased and changed the size of the air bubbles. It is a good idea to use a compressor that provides the same rate of air when the experiments are running.
- iii) The T-type probes used to measure the inlet and outlet temperature should be installed closer to the entrance and exit of the solar thermal collector and two T-type probes should be added to the experiment, one installed close to the tank entrance and a second installed at the tank exit. These T-type probes can measure the difference between inlet and outlet tank temperature.
- iv) Several thermocouples should also be installed in the solar collector to measure surface temperatures.
- v) Temperature and pressure gauges should be added to the experiment.
- vi) Need to assess the gas heating rate during compression.
- vii) Need to determine thermal losses from uninsulated pipe.
- viii) Need to do outdoor tests in sunny weather.
- ix) Also, the two-phase segmented flow should be tested as a working fluid in a solar thermal collector in different orientations, such as horizontal, vertical, and angle positions.

References

- Awad, M M and Y S Muzychka. "Bounds on Two-Phase Frictional Pressure Gradient in Minichannels and Microchannels." *Heat Transfer Engineering* 28 (2007): 720-729.
- Ahmad Asyraf, Ramli. "Theoretical Analysis of Solar Water Heating System." PhD diss., Universiti Malaysia Pahang, 2010.
- Bretherton, F. "The Motion of Long Bubbles in Tubes." *Journal of Fluid Mechanics* 10 (1961): 166-188.
- Cavallini, A, et al. "Two-Phase Frictional Pressure Gradient of R236ea, R123a and R410A Inside Multiport Minichannels." *Experimental Thermal and Fluid Science* 29 (2005): 961-870.
- Chen, W L, M C Twu and C Pan. "Gas-Liquid Two-Phase Flow in Microchannels." *Int.J.Multiphase Flow* 28 (2002): 1235-1235.
- Chisholm, D. "A Theoretical Basis for the Lockhart-Martinelli Correlation for Two-Phase Flow." *International Journal of Heat and Mass Transfer* 30 (2004): 1121-1128.
- Chung, P M.Y and M Kawaji. "The Effect of Channel Diameter on Adiabatic Two-Phase Flow Characteristics in Microchannels." *Int.J.Multiphase Flow* 30 (2004): 735-761.
- Churchill, S W and R Usagi. "A General Expression for the Correlation of Rates of Transfer and Other Phenomena." *American Institute of Chemical Engineers* 18 (1972): 1121-1128.
- "Solar Heating Design and Installation Guide.", Chartered Institution of Building Services Engineers-CIBSE, Malta, 2007.
- Fanniger, G. "Solar Water Heating Systems." *Comprehensive Renewable Energy* (2009): 419-447.
- Field, B S and P Hrujak. "Adiabatic Two-Phase Pressure Drop of Refrigerants in Small Channels." *Heat Transfer Engineering* 28 (2007): 704-712.
- Fries, D, F Trachsel and P R Von Rohr. "Segmented Gas-Liquid Flow Characterization in Rectangular Channels." *International Journal of Multiphase Flow* 34 (2008): 1108-1118.
- German Solar Energy Society. "Planning and Installing Solar Thermal Systems: A Guide for Installers, Architects and Engineers." United Kingdom, 2007.
- Goswami, D. Yogi, Frank Kreith, and Jan F. Kreider. *Principles of solar engineering*. CRC Press, 2000.
- Horvath, C, B A Solomon and J M Engasser. "Measurement of Radial Transport in Slug Flow Using Enzyme Tubes." *Industrial and Engineering Chemistry, Fundamentals* 12 (1973): 431-439.
- Hughmark, G A. "Holdup and Heat Transfer in Horizontal Slug Gas-Liquid Flow." *Chemical Engineering Science* 8 (1965): 239-257.
- Kalogirou, S A. "Solar Thermal Collectors and Applications." *Progress in Energy and Combustion Science* (2004): 231-295.

- Kawaji, M and P M Chung. "Adiabatic Gas-Liquid Flow in Microchannels." *Microscale Thermophysical Engineering* 8 (2004): 239-257.
- Kawaji, M, K Mori and D Bolintineanu. "The Effect of Inlet Geometry on Gas-Liquid Two-Phase Flow in Microchannels." *Proc. ICMM2005, Third International Conference on Microchannels and Minichannels*. Toronto, Ontario, 2005.
- Kolb, W B and R L Cerro. "Coating the Inside of a Capillary of Square Cross Section." *Chem. Eng. Science* 46 (1991): 2181-2195.
- Kreutzer, M T, et al. "Inertial and Interfacial Effect on Pressure Drop of Taylor Flow in Capillaries." *AIChE Journal* 51 (2005): 2428-2440.
- Lakehal, D, G Larrignon and C Narayanan. "Computational Heat Transfer and Two-Phase Topology in Miniature Tubes." *Microfluidics and Nanofluidics* 4 (2006): 261-271.
- Lee, H J and S Y Lee. "Pressure Drop Correlations for Two-Phase Flow within Horizontal Rectangular Channels with Small Heights." *Int.J.Multiphase Flow* 27 (2001): 783-796.
- Lockhart, R W and R C Martinelli. "Proposed Correlation of Data for Isothermal Two-Phase Flow, Two Component Flow in Pipes." *Chemical Engineering Progress* 45 (1949): 39-48.
- Mohseni, K and E S Baird. "Digitized Heat Transfer Using Electrowetting on Dielectric." *Nanoscale and Microscale Thermophysical Engineering* 11 (2007): 99-108.
- Monde, M and Y Mitsutake. "Enhancement of Heat Transfer Due to Bubble Passing Through a Narrow Vertical Rectangular Channel." *Heat Mass Transfer* 31 (1995): 77-82.
- Muzychka, Y S and M M Awad. "Two-Phase Flow Modelling in Microchannels and Minichannels." *ICNMM2008, Sixth International ASME Conference on Nanochannels, Microchannels, and Minichannels*. Darmstadt, Germany, 2008.
- Muzychka, Y S and M M Yovanovich. "Laminar Forced Convective Heat Transfer in the Combine Entry Region of Non-Circular Ducts." *Journal of Heat Transfer* 126 (2004): 54-62.
- Muzychka, Y S, E Walsh and P Walsh. "Heat Transfer Enhancement Using Laminar Gas-Liquid Segmented Fluid Stream." *Proceeding of InterPack 2009*. San Francisco, 2009.
- Narayanan, C and D Lakehal. "Two-Phase Convective Heat Transfer in Miniature Pipes Under Normal and Microgravity Conditions." *Journal of Heat Transfer* 130 (2008).
- Nicholas, Gill Janes. "Experimental Measurement Of Thermal Characteristics of Two-Phase Segmented Flow in Minichannel Heat Sink." (2012).
- Ohtake, H, Y Koizumi and H Takahashi. "Frictional Pressure Drops of Single-Phase and Gas-Liquid Two-Phase Flows in Circular and Rectangular Microchannels." *Proceeding of ICMM2005, Third International Conference on Microchannels and Minichannels*. Toronto, Ontario, 2005.
- Oliver, D R and A Young Hoon. "Two-Phase Non-Newtonian Flow: Part 1 Pressure Drop and Holdup." *Transactions of the Institution of Chemical Engineers* 46 (1968): 106-115.

- Oliver, D R and S J Wright. "Pressure Drop and Heat Transfer in Gas-Liquid Slug Flow in Horizontal Tubes." *British Chemical Engineering* 9 (1964): 590-596.
- Ovadia , Shoham. "Mechanistic Modeling of Gas-Liquid Two-Phase Flow in Pipe." (2006): 1-11.
- Sabonnadiere, Jean-Claude. *Renewable energy technologies*. Vol. 146. John Wiley & Sons, 2009.
- Sen, Zekai. *Solar energy fundamentals and modeling techniques: atmosphere, environment, climate change and renewable energy*. Springer Science & Business Media, 2008.
- Taylor, G I. "Deposition of a viscous Fluid on the Wall of a Tube." *Journal of Fluid Mechanics* 10 (1961): 161-165.
- Tran, T N, et al. "Two-Phase Pressure Drop of Refrigerants during Flow Boiling in Small Channels: An Experimental Investigation and Correlation Development." *Int.J.Multiphase Flow* 26 (2000): 1739-1754.
- Ua-Arayaporn, P, et al. "Numerical Simulation of Gas-Liquid Two-Phase Convective Heat Transfer in a Micro Tube." *ECI International Conference on Heat Transfer and Fluid Flow in Microscale*. Castelvechio Pascoli, 2005.
- Ungar, E K and J D Cornwell. "Two-Phase Pressure Drop of Ammonia in Small Diameter Horizontal Tubes." *Seventeenth AIAA Aerospace Ground Testing Conference*. Nashville, TN, 1991.
- Vrentas, J S, J L Duda and G D Lehmkuhi. "Characteristics of Radial Transport in Solid-Liquid Slug Flow." *Industrial and Engineering Chemistry, Fundamentals* 17 (1978): 39-45.
- Walsh, P, E Walsh and Y S Muzychka. "Laminar Slug Flow Heat Transfer Characteristics with A Constant Flux Boundary." *Proceeding of the ASME Summer Heat Transfer Conference*. San Francisco, 2009.
- Yu, Z, O Hemminger and L S Fan. "Experiment and Lattice Boltzmann Simulation of Two-Phase Gas-Liquid Flows in Microchannels." *Chemical Engineering Science* 62 (2007): 7172-7183.

Appendix A
Solar Thermal Collector Specification



SunMaxx Solar™
Hot Water Solutions



SunMaxx TitanPower-AL2 Collector

SUPERIOR PERFORMANCE

Laser-welded aluminum frame results in increased absorber efficiency

CUTTING-EDGE DESIGN

Constructed of anodized aluminum frame and tempered glass

EXCEPTIONAL VERSATILITY

Integrated frame mounting system suitable for both high temperature and cold weather environments

ENDURING RELIABILITY

Features a 10-year warranty

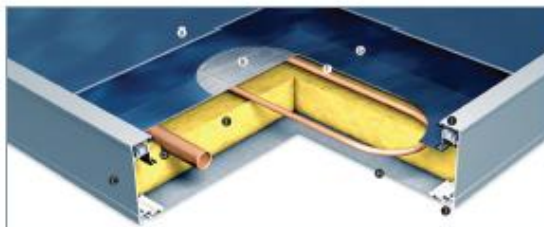


An Investment with Real Returns

The TitanPower-AL2 solar flat plate collector couples together efficiency and quality with affordability. Its laser-welded aluminum frame ensures the highest possible stagnation temperatures and guarantees the highest possible levels of quality control. The use of aluminum also allows for a thicker absorber, increasing efficiency without increasing the price.

The TitanPower-AL2 is the ideal solar collector for residential domestic hot water solar heating applications, but can also be used for small and medium sized commercial solar hot water installations.

- Advanced, high performing serpentine flat plate solar collector
- Adaptable for steamback applications
- Great dollar per BTU ratings for residential applications.
- Easy, streamlined mounting and installation process
- Laser-welded aluminum absorber
- 2 connections at top, along length or on front
- Absorber area 21.53ft²
- Gross area 23.14 ft²
- 10-year warranty
- Solar Keymark and SRCC Certified



- A) Solar glass
- B) Al-absorber sheet
- C) Powder-coated aluminium frame
- D) Collector pipe
- E) Mineral wool insulation
- F) Meander tube
- G) Highly-selective absorber coating
- H) Bottom plate made of aluminium
- I) Secure glass fixing
- J) Revolving groove for assembly



SunMaxx Solar 56 Broome Corp. Pkwy, Conklin, NY 13748 | 1.877.786.6299 1.800.786.0329 fax | www.sunmaxxsolar.com

© 2010 SunMaxx Solar, Inc. Specifications subject to change without notice.



PRODUCT DATA SHEET

TitanPower-AL2 Flat Plate Collector

Technical Specifications

Construction	Flatplate collector for on-roof, flat-roof and facade mounting
Measurement (in.)	73.62 x 45.27
Gross Area (ft. ²)	23.14
Height (in.)	2.95
Absorber Area (net, ft. ²)	21.53 (=aperture area)
Total Weight, dry (lbs)	83.77
Fluid Capacity (gal.)	0.46
Nominal Flow Rate (gal./hr.)	21.33 (low flow conditions: 10.57)
Nominal Pressure Loss (psi)	0.87 (low flow conditions: 0.43, water/propylene glycol 68°F)
Hydraulic Connection	Series connection with collectors side-by-side
Collector Connection	2 pipe ends ø12 mm for compression fittings
Absorber Type	Al-sheet & Cu-tubes, absorber with 1 serpentine ø12 mm
Absorber Coating	Highly selective on aluminium (eta plus_al)
Absorption/Emission	95% / 5%
Covering	Low iron, clear, solar safety glass (ESG)
Transmission of Covering	88%
Impact Resistance	Cover passed optional impact resistance tests following EN12975-2
Insulation	Mineral wool, 1.18"
Collector Case	Aluminium frame, powder coated
Efficiency	eta 0: 80.1% related to the aperture area
Heat Loss Coefficient	a1 (k1) - 2.28231 Btu/hr/ft/K a2 (k2) - .0095337 Btu/hr/ft/K
Max. Stagnation Temperature	375.8° F
Max. Operation Pressure (psi)	145.03
Angle of Inclination	20° – 90°
Permissible Wind Load	.44 psi
Permissible Snow Load	.58 psi
Recommended Heat Transfer Fluid	Antifreeze mix based on propylene-glycol

10-Year Warranty
SRCC Certified
Solar Keymark Certified

SunMaxx Solar, Inc.
56 Broome Corporate Pkwy
Conklin, NY 13748
1.877.786.6299
1.800.786.0329 fax
www.sunmaxxsolar.com

Appendix B

Compressor Specifications

Length	26.25 in
Width	11.37 in
Height	27.5 in
Weight	70 lbs
SCFM AT 40 PSI	5.5
SCFM AT 90 PSI	3.8
Lubrication	Oil-Free
Tank Capacity	8 gal
Maximum Pressure	150 PSI
Running HP	1.3
Style	Horizontal
Voltage	120 V
Motor	Induction
Power Type	Electric

Appendix C

Solenoid Valve Specifications

OMEGA-FLO® 2-WAY GENERAL PURPOSE SOLENOID VALVES

SV3300 Series



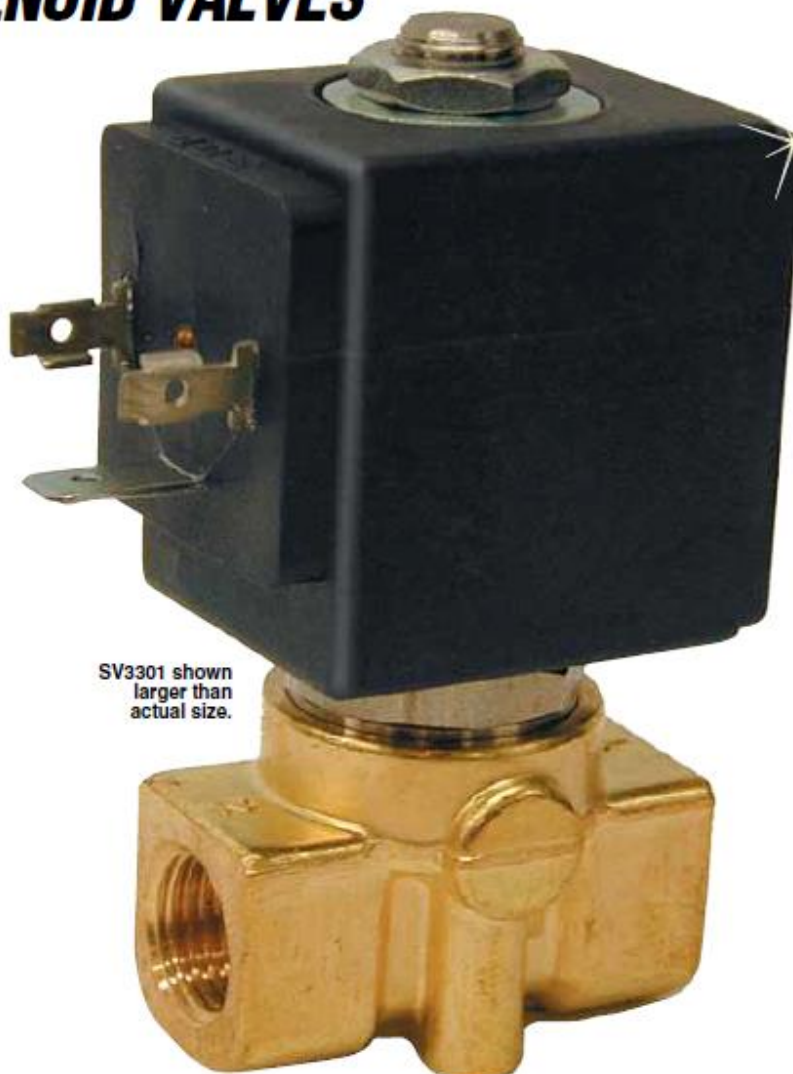
- ✓ Ideal for Compressed Air, Inert Gas, Water and Synthetic Oils
- ✓ Available in Normally Open or Normally Closed
- ✓ Process Temperature to 137°C (280°F)
- ✓ 8 W, AC Coils Standard, 12 or 14 W, AC or DC Coils Available

SV-3300 Series 2-way solenoid valves are direct-acting valves featuring brass, stainless steel construction and FKM seal material. The temperature range from -10 to 137°C (14 to 280°F) is ideal for neutral media such as compressed air, inert gases, water, and synthetic oils. A strain-relief connector is supplied with each unit. A ½" conduit plug is also available.

SPECIFICATIONS

Mounting Position: Any (preferably with solenoid system upright)
Maximum Process Temperature: 137°C (280°F) due to FKM O-ring
Maximum Ambient Temperature: Coil Dependent (See ratings on coils)
Voltage Tolerance: ±10%
Opening Time (msec):
 AC: 10 to 20
 DC: 20 to 80 depending on orifice and pressure
Closing Time (msec):
 AC and DC: 20 to 30 approximately
Cycling Rate: Approx. 1000 cpm

Duty Cycle: Continuous (100%)
Coil Molding Material:
 Black Polyester (Class F):
 SV8COIL-115AC
 SV8COIL-24DC/60HZ
 SVCOIL-24AC/50 to 60HZ
 SV8COIL-220AC
 Black Polyamide (Class F):
 SV8COIL-12DC, SV8COIL-24DC, all 12 Watt coils
 Black Polyphenylsulphide (Class H):
 SV8COIL-115/60HZ
 Black Epoxy Resin (Class H):
 All 14 Watt coils



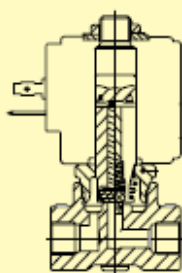
SV3301 shown larger than actual size.

Materials of Construction	
Body	Brass
Armature Tube	Stainless Steel 300
Fixed Core	Stainless Steel 400
Plunger	Stainless Steel 400
Spring	Stainless Steel 300
Shading Ring	Copper
Orifice ≤ 1/8"	Stainless Steel 300
Orifice > 1/8"	Brass
Sealing Material	FKM

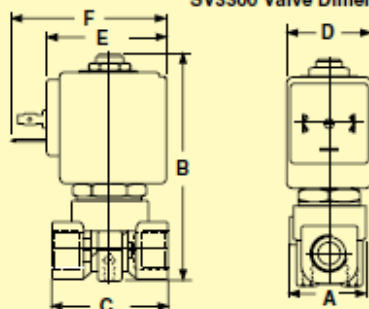
Coil Specifications		
Coil	Inrush VA	Holding VA
8 W	25	14
12 W	36	23
14 W	43	27

J-13

Normally Closed



SV3300 Valve Dimensions



Valve Dimensions

Pipe Size	A	B	C
1/8"	1 3/32"	3 1/16"	1 5/8"
1/4"			

Coil Dimensions

Watt	D	E	F
8	1 1/16"	1 21/32"	2 1/8"
12	1 7/16"	1 29/32"	2 3/8"
14	2 1/16"	2 5/32"	2 5/8"

To Order

Normally Closed	Normally Open	Pipe Size	Orifice Size	Cv Flow Factor	Coils		MIN psi	Operating Pressure M.O.P.D.*	
					Standard	Optional		AC psi	DC psi
SV3301	SV3301-NO	1/8"	1/16"	0.10	8 W	—	0	435	260
SV3302	SV3302-NO	1/8"	5/64"	0.14	8 W	—	0	315	230
		1/8"	5/64"	0.14	—	12 or 14 W	0	505	435
SV3303	SV3303-NO	1/8"	3/32"	0.22	8 W	—	0	200	130
		1/8"	3/32"	0.22	—	12 or 14 W	0	435	360
SV3304	SV3304-NO	1/8"	1/8"	0.28	8 W	—	0	145	85
		1/8"	1/8"	0.28	—	12 or 14 W	0	360	260/290†
SV3305	SV3305-NO	1/8"	3/16"	0.45	8 W	—	0	70	30
		1/8"	3/16"	0.45	—	12 or 14 W	0	170	100/115
SV3306	SV3306-NO	1/4"	1/16"	0.10	8 W	—	0	430	260
SV3307	SV3307-NO	1/4"	5/64"	0.14	8 W	—	0	315	230
		1/4"	5/64"	0.14	—	12 or 14 W	0	505	435
SV3308	SV3308-NO	1/4"	3/32"	0.22	8 W	—	0	200	130
		1/4"	3/32"	0.22	—	12 or 14 W	0	435	360
SV3309	SV3309-NO	1/4"	1/8"	0.28	8 W	—	0	145	85
		1/4"	1/8"	0.28	—	12 or 14 W	0	360	260/290†
SV3310	SV3310-NO	1/4"	3/16"	0.45	8 W	—	0	70	30
		1/4"	3/16"	0.45	—	12 or 14 W	0	170	100/115†
SV3311	SV3311-NO	1/4"	7/32"	0.63	8 W	—	0	45	15
		1/4"	7/32"	0.63	—	12 or 14 W	0	100/145†	35/70†

* Maximum operational pressure differential.

† BSP threads. In most cases BSP and NPT are interchangeable in this size.

‡ Rating for 12 W/14 W units as shown.

Accessories

Model No.	Description
Connectors	
SV-CGC	Replacement cable grip connector
SV-CC	1/2" conduit connector
Coils	
SV8COIL-115AC	Replacement 8 W coil for 110 to 120 Vac/50 to 60 Hz 154°C (310°F) (Class F)
SV8COIL-12DC	8 W coil for 12 Vdc 154°C (310°F) (Class F)
SV8COIL-24DC	8 W coil for 24 Vdc 154°C (310°F) (Class F)
SV8COIL-24AC/60HZ	8 W coil for 24 Vac/50 to 60Hz 182°C (360°F) (Class F)
SV8COIL-220AC	8 W coil for 220 to 240 Vac/50 to 60 Hz 154°C (310°F) (Class F)
SV8COIL-115/60HZ	8 W coil for 115 Vac/60 Hz 182°C (360°F) (Class H)
SV12COIL-120/60HZ	12 W coil for 120 Vac/60 Hz 154°C (310°F) (Class F)
SV12COIL-12DC	12 W coil for 12 Vdc 154°C (310°F) (Class F)
SV12COIL-24DC	12 W coil for 24 Vdc 154°C (310°F) (Class F)
SV14COIL-24DC	14 W coil for 24 Vdc 182°C (360°F) (Class H)
SV14COIL-24/50-60HZ	14 W coil for 24 Vdc/50 to 60Hz 182°C (360°F) (Class H)
SV14COIL-12DC	14 W coil for 12 Vdc 182°C (360°F) (Class H)

Comes complete with operator's manual, 8 W coil and cable grip connector.

Ordering Examples: SV3309, 1/4" normally closed valve for 1/8" orifice.

SV3303-NO, 1/8" normally open valve for 3/32" orifice.

Appendix D

PIC Microcontroller Code

```

#include<16F877.H>
#define adc=10; //Set ADC to 10 bit
#define HS,NOWDT,NOPROTECT,NOBROWNOUT,NOPUT //Configuration Fuses
#define delay(clock=20000000) //20Mhz Clock
#define rs232(baud=9600,xmit=PIN_c6,rcv=PIN_C7,PARITY=N,BITS=8)
#define org 0x1F00,0x1FFF{} //Reserve Memory for Bootloader

int16 pot1_space;
int16 pot2_length;

void main() {
    puts("Valve Controller\r\n"); //Print a message to serial port
    setup_adc_ports(all_analog); //set all pins on ports A and E to analog.
    setup_adc(ADC_CLOCK_DIV_32); //set ADC conversion speed for 20 Mhz Clock.

    set_adc_channel(0); //set ADC channel to 0
    delay_us(21);

    while (true){

        set_adc_channel(0); //set ADC channel to 0
        delay_us(21);
        pot1_space = read_adc();
        set_adc_channel(1);
        delay_us(21); //set ADC channel to 1
        pot2_length = read_adc();

        if (pot1_space >1023) {
            pot1_space =1023;
        }

        if (pot2_length >1023){
            pot2_length = 1023;
        }

        output_low(pin_b2);
        output_high(pin_b1);
        delay_ms(pot2_length);

        printf("%4Lu\t",pot2_length);

        output_low(pin_b2);
        output_low(pin_b1);
        delay_ms(pot1_space);

        printf("%4Lu\r",pot1_space);

    }
}

```

Appendix E

Measurement Devices Specifications

2700, 2701,
2750

Multimeter/Data Acquisition/ Switch Systems



- Combines functions of DMM, switch system, and datalogger
- True 6½-digit (22-bit) resolution
- Choice of 12 switch/control plug-in modules
- Up to 200 differential input channels (with 300V isolation) for measurement and control
- Convenient front panel inputs
- Free TestPoint start-up software
- Free LabVIEW, LabWindows/CVI, Visual Basic, C/C++, and TestPoint drivers (IVI style)
- Ethernet, GPIB, RS-232 communications capabilities
- Optional ExcelINX-1A datalogging software

Fast Setup and Operation

The Integra systems are fully integrated, off-the-shelf measurement and control systems. Their DMM-like interfaces make it easy for users to collect data and/or perform troubleshooting within minutes of installation and startup. Once sensor or DUT leads are hooked to the instrument's input, use the front panel controls to select the measurement function, range, filtering, scaling, trigger source, scanning sequence, alarms, and more. The TestPoint runtime start-up software included with the Integra systems makes it easy to configure and use the system in a graphical "point-and-click" environment. This gives developers the basic tools needed to create a simple application without writing program code. If the application demands greater functionality, this free runtime can be modified with the TestPoint software application package (sold separately).

The Advantage of Integrated Design

The Integra systems offer a variety of advantages over existing solutions for ATE and data acquisition applications. For example, their flexible modular architecture and integrated measurement, switching, and control capabilities save rack space by reducing the number of separate instruments needed. This design also simplifies expanding the system as the number of channels grows or re-purposing it as new test requirements evolve. Integrated signal conditioning, scaling, stimulus, filtering and I/O capabilities eliminate the need for external circuitry when designing and building data acquisition systems. The Integra systems offer accuracy and repeatability superior to plug-in data acquisition boards, while providing faster test times than typical DMM/switch systems. This makes it possible to combine higher test yields with higher test throughput.

Ethernet

The Model 2701 offers a 10/100 BaseT Ethernet connection for high speed and long distance communication between a computer and a virtually infinite number of instruments. Any PC with an Ethernet port can connect to a single Model 2701

Integra Series systems (2700, 2701, 2750) combine precision measurement, switching, and control in a single, tightly integrated enclosure for either rack-mounted or benchtop applications. These cost-effective, high performance test platforms offer affordable alternatives to separate DMMs and switch systems, dataloggers/recorders, plug-in card data acquisition equipment, and VXI/PXI systems. The Integra Series plug-in switching and control modules offer unmatched flexibility and testing efficiency for a wide range of industries and applications. System builders can create test solutions with a combination of channel count, cost per channel, and system performance unmatched by any other single-box measurement system. The input modules provide the flexibility to vary the channel count from 20 to 200 (2-pole), apply a stimulus to the device under test, route signals, control system components, and make precision measurements with up to 14 functions. Robust digital I/O capabilities can be used for triggering, handshaking with other automation equipment, and alarm limit outputs. Scan rates of more than 500 channels/second (up to 3500 readings/second) increase test productivity.

ACCESSORIES AVAILABLE

ExcelINX-1A	Excel Add-In Software for 2700, 2701, and 2750 Instruments
2750-321A	Extra slot cover
7788	50-Pin D-Shell Connector Kit (2 each) (for Models 7703, 7705 Modules w/D-sub Connections)
7789	50-Pin/25-Pin D-Shell Kit (1 each)
7790	50-Pin Male, 50-Pin Female and 25-Pin Male IDC D-Shell Connector Kit (1 each) (Ribbon Cable not included)
7797	Calibration Extender Board (for Model 2750)
7705-MTC-2	50-Pin Male to Female D-Sub Cable, 2m
7707-MTC-2	25-Pin Male to Female D-Sub Cable, 2m

1.888.KEITHLEY (U.S. only)

www.keithley.com

KEITHLEY

A GREATER MEASURE OF CONFIDENCE

2700, 2701, 2750

Ordering Information

2700	DMM, Data Acquisition, Datalogging System w/2 Slots
2701	DMM, Data Acquisition, Datalogging System w/2 Slots and Ethernet Support
2750	DMM, Data Acquisition, Switching, Datalogging System w/5 Slots

These products are available with an Extended Warranty.

Accessories Supplied

TestPoint runtime start-up software; LabVIEW, LabWindows/CVI, Visual Basic, C/C++, and TestPoint drivers; manual; and Model 1751 Safety Test Leads.

Built-in measurement functions include:

- DCV • ACV • DCI • ACI
- Resistance (2- or 4-wire, offset compensation selectable)
- Dry circuit ohms (20mV clamp) 2750 only
- Temperature (with thermocouples, RTDs, or thermistors)
- Frequency/Period
- Continuity

TYPICAL APPLICATIONS

- Production test of electronic products and devices
- Accelerated stress testing (AST)
- Process monitor and control
- Device characterization/R&D
- Low ohms, multichannel measurements

1.888.KEITHLEY (U.S. only)

www.keithley.com

Multimeter/Data Acquisition/ Switch Systems

in a point-to-point configuration, to multiple Model 2701s through a hub, or to multiple Model 2701s distributed on a network.

The Model 2701 Ethernet port uses the industry-standard TCP/IP socket interface. This provides data rates up to 100Mbps/sec. and allows the instrument to be located up to 100 meters from the nearest computer or network hub in hardwired systems and miles in wireless Ethernet systems. The maximum distances between a control PC and the instruments are limited only by the size of the network. The instrument also provides a built-in diagnostic web page for easy remote access to the Model 2701. Entering the instrument's IP address in the URL line of Microsoft Internet Explorer® will allow communication with and control of the Model 2701. This Web page allows users to read and set network parameters, such as IP address, subnet mask, gateway, MAC address, and calibration dates, and to send commands to and query data from the Model 2701.

Temperature Capabilities

Integra Series mainframes support three major types of temperature sensors with built-in signal conditioning and 300V isolation: thermocouples, RTDs, and thermistors. To begin using a sensor, simply hook it up and the instrument does the rest. If a thermocouple is broken or disconnected, the instrument will alert the operator. The mainframes also support three methods for cold-junction compensation (CJC): automatic (built-in), external (built-in), and simulated.



Install up to five input modules in the 2750 mainframe (or up to two in the 2700 and 2701 mainframes). All switch/control modules are fully enclosed in impact-resistant plastic for exceptional ruggedness. Three connector alternatives simplify connecting the modules to DUTs. Rugged D-sub connectors allow quick, secure connections and are especially convenient when performing routine maintenance or when the system is installed in a rack. IDC ribbon cable adapters are supplied with the Model 7701, 7707, and 7709 modules for fast, uncomplicated hookups in production test and process monitoring applications. Oversize screw-terminal connectors simplify setup in applications that require the greatest connection flexibility. Additional D-sub and IDC ribbon cable connector kits and pre-wired cable assemblies are sold separately.

Integra Series integrated switching, measurement, and datalogging solutions

MULTIMETER/DATA
ACQUISITION/SWITCH SYSTEMS

KEITHLEY

A GREATER MEASURE OF CONFIDENCE

2700, 2701, 2750

Ordering Information

- 7700** 20-Channel Differential Multiplexer Module with up to 50MHz Bandwidth w/Automatic CJC and Screw Terminals
- 7701** 32-Channel Differential Multiplexer Module with a 25- and 50-Pin Female D Connector. Supplied with Male IDC Ribbon Cable Connectors
- 7702** 40-Channel Differential Multiplexer Module w/Screw Terminals
- 7703** 32-Channel High Speed, Differential Multiplexer Module with 2 50-Pin Female D Connectors. Includes 2 Mating Connectors
- 7705** 40-Channel Single-Pole Control Module with 2 50-Pin Female D Connectors. Includes 2 Mating Connectors.
- 7706** All-in-One I/O Module: 20-Channel Differential Multiplexer w/Automatic CJC, 16 Digital Outputs, 2 Analog Outputs, a Counter/Totalizer, and Screw Terminals
- 7707** 32-Channel Digital I/O w/10-Channel Differential Multiplexer Module with a 25-Pin Female and 50-Pin Male D Connectors. Supplied with Mating IDC Ribbon Cable Connectors
- 7708** 40-Channel Differential Multiplexer Module w/Automatic CJC and Screw Terminals
- 7709** 6x8 Matrix Module with 25- and 50-Pin Female D Connectors. Supplied with Male IDC Ribbon Cable Connectors
- 7710** 20-Channel Solid-State/Long Life Differential Multiplexer w/Automatic CJC and Screw Terminals
- 7711** 20GHz 50Ω RF Module with Dual 1x4 Configuration and SMA Connections
- 7712** 3.5GHz 50Ω RF Module with Dual 1x4 Configuration and SMA Connections

These products are available with an Extended Warranty.

1.888.KEITHLEY (U.S. only)

www.keithley.com

Multimeter/Data Acquisition/Switch Systems



Rugged 50-pin D-sub connectors ensure dependability and quick setup/teardown in production test racks.

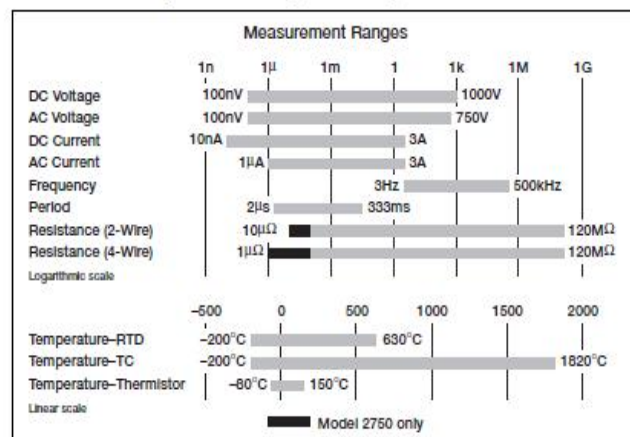


Screw terminals use oversize connectors for easier, mistake-free wiring. Easy-to-use removable terminals are available on some models.

Software Solutions

Whether the task calls for a simple start-up package to acquire several channels of data or the tools to create a fully custom acquisition and analysis solution, Keithley has the software needed to get the most performance from a Model 2700, 2701, or 2750 Multimeter/Switch System. Our broad range of software solutions makes it easy to get applications "Up & Running" quickly and economically.

Measurement Ranges for the Integra Series Systems



KEITHLEY

A GREATER MEASURE OF CONFIDENCE

2700, 2701, 2750

Multimeter/Data Acquisition/ Switch Systems

Important Features and Benefits

- **Full per-channel configurability**—Each channel can be independently configured for making measurements. The parameters that can be chosen for each channel include speed, range, resolution, number of power line cycles (NPLC), filtering type, offset compensation, math functions to be displayed, CJC type, RTD type, frequency gate time, "m" and "b" values in mX + b format, HI/LO limits, low Ω (Model 2750 only), ratio calculation, and thermistor type.
- **Channel monitor feature**—Monitor any specific input channel on the front panel display during a scan. This feature can also serve as an analog trigger to initiate a scan sequence based on some external factor, such as a temperature rising above a pre-set limit. Only the data of interest is acquired, so there's no need to spend hours searching through reams of normal readings to find anomalous data.
- **Front/rear switch**—Switching between the front and rear panel measurement inputs is as easy as pressing a button. Users can select the front panel inputs for tasks such as system set-up and verification, manual probing, troubleshooting, and calibration, while the rear panel inputs through the modules allow fast, automated multiplexing and control.
- **Battery-backed set-up memory**—Up to four different set-up configurations can be stored in onboard memory. If the line power fails during a scan, the system will resume scanning where it stopped once power is restored.
- **Relay counting**—Provides preventive maintenance of the system and switches.
- **Memory buffer**—The mainframe's non-volatile wrap-around reading memory allows continuous, unattended datalogging over long periods—data in the buffer can be transferred to a PC controller automatically as new data is acquired. The real-time clock can be used to time- and date-stamp readings for later review and interpretation.
- **2 TTL-level digital inputs**—For implementing external triggers to initiate a scan sequence.
- **5 "per-channel" HI/LO alarm limit TTL outputs**—Trigger external alarms or perform other control functions without a PC controller.
- **Dry circuit ohms (20mV clamp)**—Protects sensitive devices from damage and prevents self-heating errors during testing (Model 2750 only).
- **Virtual channel**—Stores the results of channel-to channel ratio and average math operations.
- **Onboard statistical analysis**—Mathematical functions available at the push of a button are channel average, mX+b scaling, minimum, maximum, average, and standard deviation.
- **GPIB and RS-232 interfaces (Models 2700 and 2750)**
- **Ethernet and RS-232 interface (Model 2701 only)**
- **3-year warranty**

Which Integra Mainframe is the Best Choice for the Application?

Use this selector guide to decide which Integra Series mainframe offers the combination of features and capacity that's right for a specific application. If testing requirements change in the future, switch/control modules and test code can be easily re-used.

	2700	2701	2750
No. of differential input channels	80	80	200
Matrix crosspoints	96	96	240
Ohms resolution	100 $\mu\Omega$	100 $\mu\Omega$	1 $\mu\Omega$
Dry circuit ohms (20mV clamp)	No	No	Yes
No. of slots	2	2	5
Memory buffer	55,000 rdgs	450,000 rdgs	110,000 rdgs
Size (2U height)	Half-rack width	Half-rack width	Full-rack width (19")
Communications	GPIB, RS-232	Ethernet, RS-232	GPIB, RS-232
Scan-Rate (memory)	180/s	500/s	230/s
Scan-Rate (bus)	145/s	440/s	210/s
Max. Internal Trigger Rate	2000/s	2800/s	2000/s
Max. External Trigger Rate	375/s	2000/s	375/s

1.888.KEITHLEY (U.S. only)

www.keithley.com

KEITHLEY

A GREATER MEASURE OF CONFIDENCE

Integra Series integrated switching, measurement, and datalogging solutions

MULTIMETER/DATA
ACQUISITION/SWITCH SYSTEMS

2700, 2701, 2750

Multimeter/Data Acquisition/ Switch Systems

DC CHARACTERISTICS¹

CONDITIONS: MED (1 PLC) or 10 PLC or MED (1 PLC) with Digital Filter of 10

FUNCTION	RANGE	RESOLUTION	TEST CURRENT ±5% OR BURDEN VOLTAGE	INPUT RESISTANCE OR OPEN CKT. VOLTAGE ²		ACCURACY: ±(ppm of reading + ppm of range) (ppm = parts per million) (e.g., 10ppm = 0.01%)			TEMPERATURE COEFFICIENT 0°-18°C & 28°-50°C
				2700/2701	2750	24 Hour ⁴ 23°C±1°	90 Day ⁴ 23°C±5°	1 Year 23°C±5°	
Voltage ¹¹	100.0000 mV	0.1 µV		>10 GΩ	>10 GΩ	15 + 30	25 + 35	30 + 35	(1 + 5)/°C
	1.000000 V	1.0 µV		>10 GΩ	>10 GΩ	15 + 6	25 + 7	30 + 7	(1 + 1)/°C
	10.00000 V	10 µV		>10 GΩ	>10 GΩ	10 + 4	20 + 5	30 + 5	(1 + 1)/°C
	100.0000 V	100 µV		10 MΩ ± 1%	10 MΩ ± 1%	15 + 6	35 + 9	45 + 9	(5 + 1)/°C
	1000.000 V	1 mV		10 MΩ ± 1%	10 MΩ ± 1%	20 + 6	35 + 9	50 + 9	(5 + 1)/°C
Resistance ^{4,14}	1.000000 Ω	1 µΩ	10 mA		5.9 V	80 + 40	80 + 40	100 + 40	(8 + 1)/°C
	10.00000 Ω	10 µΩ	10 mA		5.9 V	20 + 20	80 + 20	100 + 20	(8 + 1)/°C
	100.0000 Ω	100 µΩ	1 mA	6.9 V	12.2 V	20 + 20	80 + 20	100 + 20	(8 + 1)/°C
	1.000000 kΩ	1 mΩ	1 mA	6.9 V	12.2 V	20 + 6	80 + 6	100 + 6	(8 + 1)/°C
	10.00000 kΩ	10 mΩ	100 µA	6.9 V	6.8 V	20 + 6	80 + 6	100 + 6	(8 + 1)/°C
	100.0000 kΩ	100 mΩ	10 µA	12.8 V	12.8 V	20 + 6	80 + 10	100 + 10	(8 + 1)/°C
	1.000000 MΩ	1.0 Ω	10 µA	12.8 V	12.8 V	20 + 6	80 + 10	100 + 10	(8 + 1)/°C
	10.00000 MΩ	10 Ω	0.7 µA // 10M Ω	7.0 V	7.0 V	150 + 6	200 + 10	400 + 10	(70 + 1)/°C
	100.0000 MΩ	100 Ω	0.7 µA // 10M Ω	7.0 V	7.0 V	800 + 30	2000 + 30	2000 + 30	(385 + 1)/°C
	1.000000 Ω	1 µΩ	10 mA		20 mV	80 + 40	80 + 40	100 + 40	(8 + 1)/°C
Dry Circuit Resistance ^{21,24}	10.00000 Ω	10 µΩ	1 mA		20 mV	25 + 40	80 + 40	100 + 40	(8 + 1)/°C
	100.0000 Ω	100 µΩ	100 µA		20 mV	25 + 40	90 + 40	140 + 40	(8 + 1)/°C
	1.000000 kΩ	1 mΩ	10 µA		20 mV	25 + 90	180 + 90	400 + 90	(8 + 1)/°C
	10.00000 kΩ	10 mΩ	1 mA	6.9 V	12.2 V	40 + 100	100 + 100	100 + 100	(8 + 1)/°C
Continuity (2W)	1.000 kΩ	100 mΩ	1 mA			60 + 30	300 + 80	500 + 80	(50 + 5)/°C
Current	20.00000 mA	10 nA	< 0.2 V			100 + 300	300 + 800	500 + 800	(50 + 50)/°C
	100.0000 mA	100 nA	< 0.1 V			200 + 30	500 + 80	800 + 80	(50 + 5)/°C
	1.000000 A	1.0 µA	< 0.5 V ¹⁹			1000 + 15	1200 + 40	1200 + 40	(50 + 5)/°C
	3.000000 A	10 µA	< 1.5 V ¹⁹						(50 + 5)/°C

Channel (Ratio)²⁰ Ratio Accuracy = Accuracy of selected Channel Range + Accuracy of Paired Channel Range

Channel (Average)²⁰ Average Accuracy = Accuracy of selected Channel Range + Accuracy of Paired Channel Range

TEMPERATURE¹⁹

(Displayed in °C, °F, or K. Exclusive of probe errors.)

Thermocouples (Accuracy based on ITS-90.)

TYPE	RANGE	RESOLUTION	90 DAY/1 YEAR (23°C ± 5°C) RELATIVE TO SIMULATED REFERENCE JUNCTION	USING 77XX MODULE*	TEMPERATURE COEFFICIENT 0°-18°C & 28°-50°C
J	-200 to +760°C	0.001°C	0.2°C	1.0°C	0.03°C/°C
K	-200 to +1372°C	0.001°C	0.2°C	1.0°C	0.03°C/°C
N	-200 to +1300°C	0.001°C	0.2°C	1.0°C	0.03°C/°C
T	-200 to +400°C	0.001°C	0.2°C	1.0°C	0.03°C/°C
E	-200 to +1000°C	0.001°C	0.2°C	1.0°C	0.03°C/°C
R	0 to +1768°C	0.1°C	0.6°C	1.8°C	0.03°C/°C
S	0 to +1768°C	0.1°C	0.6°C	1.8°C	0.03°C/°C
B	+350 to +1820°C	0.1°C	0.6°C	1.8°C	0.03°C/°C

* Using 7710 Module: J: 2.5°C; K: 1°C; N, T, E types: 1.5°C; R, S, B types: 2.7°C.

4-Wire RTD:

(100Ω platinum [PT100], D100, F100, PT385, PT3916, or user type. Offset compensation On)

-200° to	630°C	0.01 °C	0.06°C	0.003°C/°C
----------	-------	---------	--------	------------

Thermistor: (2.2kΩ, 5kΩ, and 10kΩ)²⁸

-80° to	150°C	0.01 °C	0.08°C	0.002°C/°C
---------	-------	---------	--------	------------

DC SYSTEM SPEEDS^{15,18}

	2700/2750	2701
RANGE CHANGES (excludes 4W12) ¹⁶	50/s (42/s)	50/s (42/s)
FUNCTION CHANGES ¹⁶	50/s (42/s)	50/s (42/s)
AUTORANGE TIME ¹⁶	<30 ms	<30 ms
ASCII READINGS TO RS-232 (19.2k BAUD):	55/s	300/s
MAX. EXTERNAL TRIGGER RATE:	375/s	2000/s

DC MEASUREMENT SPEEDS¹⁵

Single Channel, 60Hz (50Hz) Operation

FUNCTION	DIGITS	READINGS/s	PLCs
DCV, DCI, Ω (<10M), Thermocouple, Thermistor	6.5 ^{12,14}	5 (4)	10
	6.5 ¹⁴	35 (28)	1
	6.5 ^{12,14}	45 (36)	1
	5.5 ^{14,17}	150 (120)	0.1
	5.5 ^{14,17}	300 (240)	0.1
	5.5 ¹⁷	500 (400)	0.1
2701 and 2750 only	4.5 ¹⁷	2500 (2000)	0.01
2701 only	3.5	3500 (2800)	0.002
4W12 (<10M)	6.5 ¹⁴	1.4 (1.1)	10
	6.5 ¹⁴	15 (12)	1
	5.5 ¹⁷	33 (25)	0.1
4W12 OComp, RTD ²²	6.5 ¹⁴	0.9 (0.7)	10
	6.5 ¹⁴	8 (6.4)	1
	5.5 ^{14,17}	18 (14.4)	0.1
Channel (Ratio), Channel (AVG)	6.5 ¹⁴	2.5 (2)	10
	6.5 ¹⁴	15 (12)	1
	5.5 ¹⁷	25 (20)	0.1

Multiple Channels, Into Memory¹⁸

	2700	2701	2750
7710 Scanning DCV	180/s	500/s	250/s
7710 Scanning DCV with Limits or Time Stamp On	170/s	500/s	250/s
7710 Scanning DCV alternating 2W12	45/s	115/s	60/s

Multiple Channels, Into and Out of Memory to GPIB^{16,18} or Ethernet

	2700	2701	2750
7702 Scanning DCV	65/s	75/s	65/s
7700 and 7708 Scanning Temperature (T/C)	50/s	50/s	50/s
7710 Scanning DCV	145/s	440/s	210/s
7710 Scanning DCV with Limits or Time Stamp On	145/s	440/s	210/s
7710 Scanning DCV alternating 2W12	40/s	115/s	55/s

1.888.KEITHLEY (U.S. only)

www.keithley.com

KEITHLEY

A GREATER MEASURE OF CONFIDENCE

2700, 2701, 2750

Multimeter/Data Acquisition/ Switch Systems

DC SPEED vs. NOISE REJECTION

Rate	Filter	Readings/s ¹²	Digits	RMS Noise			CMRR ¹⁴
				10V Range	2701	NMRR	
10	50	0.1 (0.08)	6.5	< 1.2 μ V	< 2.5 μ V	110 dB ¹³	140 dB
1	Off	15 (12)	6.5	< 4 μ V	< 6 μ V	90 dB ¹³	140 dB
0.1	Off	500 (400)	5.5	< 22 μ V	< 40 μ V	—	80 dB
0.01	Off	2500 (2000)	4.5	< 150 μ V	< 300 μ V	—	80 dB
0.002	Off	3500 (2800)	3.5	—	< 1 mV	—	60 dB

DC MEASUREMENT CHARACTERISTICS

DC VOLTS

A-D LINEARITY: 2.0 ppm of reading + 1.0 ppm of range.

INPUT IMPEDANCE:

100mV–10V Ranges: Selectable >10G Ω // with <400pF or 10M Ω \pm 1%.

100V, 1000V Ranges: 10M Ω \pm 1%.

Dry Circuits: 100k Ω \pm 1% // <1 μ F.

EARTH ISOLATION: 500V peak, >10G Ω and <300pF any terminal to chassis.

INPUT BIAS CURRENT: <75pA at 25°C.

COMMON MODE CURRENT: <500nA at 50Hz or 60Hz.

AUTOZERO ERROR: Add \pm (2ppm of range error + 5 μ V) for < 10 minutes and \pm 1°C.

INPUT PROTECTION: 1000V all ranges, 300V with plug-in modules.

RESISTANCE

MAXIMUM 4W Ω LEAD RESISTANCE: 80% of range per lead (Dry Ckt mode). 5 Ω per lead for 1k Ω range; 10% of range per lead for 10k Ω , 100k Ω , and 1M Ω ranges; 1k Ω per lead for all other ranges.

OFFSET COMPENSATION: Selectable on 4W Ω , 1k Ω , 10k Ω , 100k Ω , and 1M Ω ranges.

CONTINUITY THRESHOLD: Adjustable 1 to 1000 Ω .

INPUT PROTECTION: 1000V All Source Inputs, 350V Sense Inputs. 300V with plug-in modules.

DC CURRENT

SHUNT RESISTORS: 100mA–3A, 0.1 Ω , 20mA, 5 Ω .

INPUT PROTECTION: 3A, 250V fuse.

THERMOCOUPLES

CONVERSION: ITS-90.

REFERENCE JUNCTION: Internal, External, or Simulated (Fixed).

OPEN CIRCUIT CHECK: Selectable per channel. Open >11.4k Ω \pm 200 Ω .

AC SPECIFICATIONS¹

Function	Range	Resolution	Calibration Cycle	Accuracy: \pm (% of reading + % of range), 23°C \pm 5°C				
				3 Hz–10 Hz	10 Hz–20 kHz	20 kHz–50 kHz	50 kHz–100 kHz	100 kHz–300 kHz
Voltage ²	100.0000 mV	0.1 μ V	90 Days	0.35 + 0.03	0.05 + 0.03	0.11 + 0.05	0.6 + 0.08	4.0 + 0.5
	1.000000 V	1.0 μ V	(all ranges)	0.35 + 0.03	0.06 + 0.03	0.12 + 0.05	0.6 + 0.08	4.0 + 0.5
	10.000000 V	10 μ V	1 Year	0.35 + 0.03	0.06 + 0.03	0.12 + 0.05	0.6 + 0.08	4.0 + 0.5
	100.0000 V	100 μ V	(all ranges)	0.35 + 0.03	0.06 + 0.03	0.12 + 0.05	0.6 + 0.08	4.0 + 0.5
(Temp. Coeff.) ³ /°C ³				0.035 + .003	0.005 + .003	0.006 + .005	0.01 + .006	0.03 + .01
Current ²	1.000000 A	1.0 μ A	90 Day/1 Yr.	0.30 + 0.04	0.10 + 0.04	0.14 + 0.04	0.18 + 0.06	0.18 + 0.06
	3.000000 A ¹⁴	10 μ A	(all ranges)	0.35 + 0.06	0.16 + 0.06	0.18 + 0.06	0.18 + 0.06	0.18 + 0.06
	10.000000 A	100 μ A	1 Year	0.35 + 0.06	0.16 + 0.06	0.18 + 0.06	0.18 + 0.06	0.18 + 0.06
	30.000000 A	300 μ A	(all ranges)	0.35 + 0.06	0.16 + 0.06	0.18 + 0.06	0.18 + 0.06	0.18 + 0.06
(Temp. Coeff.) ³ /°C ³				0.035 + 0.006	0.015 + 0.006	0.015 + 0.006	0.015 + 0.006	0.015 + 0.006
Frequency ⁴ and Period	100 mV	0.333 ppm	90 Day/1 Yr.	100 ppm + 0.333 ppm (SLOW 1s gate)	100 ppm + 0.333 ppm (MED, 100ms gate)	100 ppm + 0.333 ppm (FAST, 10ms gate)	100 ppm + 0.333 ppm (FAST, 10ms gate)	100 ppm + 0.333 ppm (FAST, 10ms gate)
	to 3.33 V	3.33 ppm	(all ranges)	100 ppm + 0.333 ppm (SLOW 1s gate)	100 ppm + 0.333 ppm (MED, 100ms gate)	100 ppm + 0.333 ppm (FAST, 10ms gate)	100 ppm + 0.333 ppm (FAST, 10ms gate)	100 ppm + 0.333 ppm (FAST, 10ms gate)
	750 V	33.3 ppm	1 Year	100 ppm + 0.333 ppm (SLOW 1s gate)	100 ppm + 0.333 ppm (MED, 100ms gate)	100 ppm + 0.333 ppm (FAST, 10ms gate)	100 ppm + 0.333 ppm (FAST, 10ms gate)	100 ppm + 0.333 ppm (FAST, 10ms gate)
	to 3.33 V	33.3 ppm	(all ranges)	100 ppm + 0.333 ppm (SLOW 1s gate)	100 ppm + 0.333 ppm (MED, 100ms gate)	100 ppm + 0.333 ppm (FAST, 10ms gate)	100 ppm + 0.333 ppm (FAST, 10ms gate)	100 ppm + 0.333 ppm (FAST, 10ms gate)

1.888.KEITHLEY (U.S. only)

www.keithley.com

KEITHLEY

A GREATER MEASURE OF CONFIDENCE

DC NOTES

- 20% overrange except on 1000V and 3A.
- Add the following to "ppm of range" uncertainty: 100mV 15ppm; 1V and 100V 2ppm; for Model 2750 1k Ω and Dry Circuit Ω 40ppm; 10–1M Ω 2ppm; for Models 2700/2701 100k Ω 30ppm, 20mA and 1A 10ppm, 100mA 40ppm.
- \pm 2% (measured with 10M Ω input resistance DMM, >10G Ω DMM on 10M Ω and 100M Ω ranges). For Dry Circuit Ω , \pm 2% with Input HI connected to Sense HI; with Sense HI disconnected add 30mV.
- Relative to calibration accuracy.
- For signal levels >500V add 0.02ppm/V uncertainty for portion exceeding 500V.
- Specifications are for 4-wire Ω , 1k Ω , 10k Ω , and 100k Ω with offset compensation on. With 77XX plug-in modules, LSYNC on. With offset compensation on, OPEN CKT. VOLTAGE is 12.8V For 2-wire Ω add 1.5k Ω to "ppm of range" uncertainty. 1k Ω range is 4-wire only.
- Must have 10% matching of lead resistance in Input HI and LO.
- Add the following to "ppm of reading" uncertainty when using plug-in modules:

	10 k Ω	100 k Ω	1 M Ω	10 M Ω	100 M Ω
All Modules:				220 ppm	2200 ppm
7701, 7703, 7707, 7709 Modules:	10 ppm	100 ppm	1000 ppm	1%	10%
7706, 7708, 7710 Modules:	5 ppm	50 ppm	500 ppm	500 ppm	5%
7710 Module 25°C \pm 5°C:	11 ppm	110 ppm	1100 ppm	1.1%	11%

- Add 1.5V when used with plug-in modules.
- For RATIO, DCV only. For AVERAGE, DCV and Thermocouples only. Available with plug-in modules only.
- Add 6 μ V to "of range" uncertainty when using Models 7701, 7705, and 7707, and 5 μ V for Models 7706 and 7709.
- Auto zero off.
- For LSYNC on, line frequency \pm 0.1 %. For LSYNC off, use 60dB for \geq 1PLC.
- For 1k Ω unbalance in LO lead, AC CMRR is 70dB.
- Speeds are for 50Hz (50Hz) operation using factory defaults operating conditions (*RST). Autorange off, Display off, Limits off, Trigger delay = 0.
- Speeds include measurements and binary data transfer out the GPIB or ASCII data transfer for Ethernet and RS-232 (reading element only).
- Sample count = 1000, auto zero off (into memory buffer).
- Auto zero off, NPIC = 0.01 (Models 2700 and 2750), NPIC = 0.002 (Model 2701).
- Additional Uncertainty:

Type	Range	Plug-In Modules				
		Front Terminals Simulated Ref. Junction	7709 Simulated Ref. Junction	7701, 7703, 7707 Simulated Ref. Junction	7706, 7708, 7710 Using CJC	7706 Using CJC
J	–200 to 0°C	0.1	0.1	0.3	0.8	1.6
K	–200 to 0°C	0.2	0.2	0.4	0.8	1.6
N	–200 to 0°C	0.3	0.3	0.6	0.8	1.6
T	–200 to 0°C	0.2	0.1	0.4	0.8	1.6
E	–200 to 0°C	—	0.1	0.3	0.8	1.6
R	0 to +400°C	0.4	0.6	1.2	0.5	1.0
S	0 to +400°C	0.4	0.6	1.2	0.5	1.0
B	+350 to +1300°C	0.8	0.3	1.7	0.5	1.0

- For lead resistance >1k Ω , add the following uncertainty Ω for measurement temperatures of:

	70°–100°C	100°–150°C
2.2 k Ω (44004)	0.22°C	1.11°C
5.0 k Ω (44007)	0.10°C	0.46°C
10 k Ω (44006)	0.04°C	0.19°C

- For 4-wire Ω only offset compensation on, LSYNC on.
- For Dry Circuit 1k Ω range, 2 readings/s max.
- For 2750 front inputs, add the following to Temperature Coefficient "ppm of reading" uncertainty: 1M Ω 25ppm, 10M Ω 250ppm, 100M Ω 250ppm. Operating environment specified for 0°C to 50°C and 90% RH at 35°C.
- Model 2750 only.
- Front panel resolution is limited to 0.1 Ω .

Integra Series Condensed Specifications

MULTIMETER/DATA ACQUISITION/SWITCH SYSTEMS

2700, 2701, 2750

Multimeter/Data Acquisition/ Switch Systems

ADDITIONAL UNCERTAINTY ±(% OF READING)

Low Frequency Uncertainty	MED	FAST
20 Hz – 30 Hz	0.3	—
30 Hz – 50 Hz	0	—
50 Hz – 100 Hz	0	1.0
100 Hz – 200 Hz	0	0.18
200 Hz – 300 Hz	0	0.10
>300 Hz	0	0

CREST FACTOR: ^a	1–2	2–3	3–4	4–5
Additional Uncertainty:	0.05	0.15	0.30	0.40
Max. Fundamental Freq.:	50kHz	50kHz	3kHz	1kHz
Maximum Crest Factor:	5 at full-scale.			

AC MEASUREMENT CHARACTERISTICS

AC VOLTS

MEASUREMENT METHOD: AC-coupled, True RMS.
 INPUT IMPEDANCE: 1MΩ ±2% // by <100pF.
 INPUT PROTECTION: 1000V or 600VDC, 300Vrms with plug in modules.

AC CURRENT

MEASUREMENT METHOD: AC-coupled, True RMS.
 SHUNT RESISTANCE: 0.1Ω.
 BURDEN VOLTAGE: 1A <0.5Vrms, 3A <1.5Vrms. Add 1.5Vrms when used with plug in modules.
 INPUT PROTECTION: 3A, 250V fuse.

FREQUENCY AND PERIOD

MEASUREMENT METHOD: Reciprocal counting technique.
 GATE TIME: SLOW 1s, MED 100ms, and FAST 10ms.

AC GENERAL

AC CMRR:^b 70dB.
 VOLT HERTZ PRODUCT: <= 8 × 10⁷.

AC MEASUREMENT SPEEDS^{7, 13}

Single Channel, 60Hz (50Hz) Operation

Function	Digits	Readings/s	Rate	Bandwidth
ACV, ACI	6.5	2s/Reading	SLOW	3 Hz–300 kHz
	6.5	4.8 (4)	MED	30 Hz–300 kHz
	6.5 ^a	40 (32)	FAST	300 Hz–300 kHz
Frequency	6.5	1 (1)	SLOW	3 Hz–300 kHz
Period	5.5	9 (9)	MED	30 Hz–300 kHz
	4.5	35 (35)	FAST	300 Hz–300 kHz
	4.5 ^b	65 (65)	FAST	300 Hz–300 kHz

Multiple Channel

7710 SCANNING ACV^{13a, 11}, 500/s.
 7710 SCANNING ACV WITH AUTO DELAY ON: 2s/reading.

AC SYSTEM SPEEDS^{7, 8, 11}

	2700/2750	2701
AC System Speed:	(19.2k)	(115.2k)
Range Changes: ¹²	4/s (3/s)	4/s (3/s)
Function Changes: ¹²	4/s (3/s)	4/s (3/s)
Average Time:	< 3s	< 3s
ASCII Readings to RS-232 (19.2k baud):	50/s	300/s
Max. External Trigger Rate:	250/s	2000/s

AC NOTES

- 20 % overrange except on 750V and 3A.
- Specification are for SLOW mode and sine wave inputs >5% of range. SLOW and MED are multi-sample A/D conversions. FAST is Deflector-BANDwidth 300 with nPLC = 1.0.
- Applies to 0°–18°C and 28°–50°C.
- For square wave inputs >10% of ACV range, except 100mV range, 100mV range frequency must be >10Hz if input is <20mV.
- Applies to non-sine waves >5Hz.
- For 1kΩ unbalance in L.O. lead.
- Speeds are for 60Hz (50Hz) operation using factory defaults operating conditions (*RST), Autorange off, Display off, Limits off, Trigger delay=0.
- For ACV inputs at frequencies of 50 or 60Hz (±10%), add the following to “% of Range” uncertainty: 100mV 0.25%, 1V 0.05%, 10V 0.15%, 100V 0.05%, 750V 0.015 (Model 2701 only).
- Auto Zero off.
- Sample count = 1024.
- Deflector-BANDwidth 300 with nPLC = 0.006 (2701 only).
- Maximum useful limit with trigger delay = 175ms.
- Includes measurement and binary data transfer out GPIB or ASCII data transfer for Ethernet and RS-232 (reading element only).

GENERAL SPECIFICATIONS:

EXPANSION SLOTS: 2 (2700, 2701), 5 (2750).
POWER SUPPLY: 100V / 120V / 220V / 240V ±10%.
LINE FREQUENCY: 65Hz to 66Hz and 360Hz to 440Hz, automatically sensed at power-up.
POWER CONSUMPTION: 28VA (2700), 80VA (2701, 2750).
OPERATING ENVIRONMENT: Specified for 0°C to 50°C. Specified to 80% RH at 35°C.
STORAGE ENVIRONMENT: –40°C to 70°C.
BATTERY: Lithium battery-backed memory, 3 years (@ 25°C (Model 2700, 2750) Lithium Ion battery-backed memory 30 days of buffer storage (@ 25°C and >4 hours charge time. Battery lifetime: >3 years (@ 25°C, >1.5 years (@ 50°C (Model 2701)).
WARRANTY: 3 years excludes battery.
EMC: Conforms to European Union Directive 89/336/EEC EN61326-1.
SAFETY: Conforms to European Union Directive 73/23/EEC EN61010-1, CAT I.
VIBRATION: MIL-PRF-28800F Class 3, Random.
WARM-UP: 2 hours to rated accuracy.
DIMENSIONS:
 Rack Mounting: 89mm high × 213mm wide (2700, 2701) or 485mm wide (2750) × 370mm deep (3.5 in × 8.375 in or 19 in × 14.563 in).
 Bench Configuration (with handle and feet): 104mm high × 238mm wide (2700, 2701) or 485mm wide (2750) × 370mm deep (4.125 in × 9.375 in (2700, 2701) or 19 in (2750) × 14.563 in).
SHIPPING WEIGHT: 6.5kg (14 lbs.) (2700, 2701) or 13kg (28 lbs.) (2750).
DIGITAL I/O: 2 inputs, 1 for triggering and 1 for hardware interlock.
 5 outputs, 4 for Reading Limits and 1 for Master Limit. Outputs are TTL compatible or can sink 250mA, diode clamped to 40V.
TRIGGERING AND MEMORY:
 Window Filter Sensitivity: 0.01%, 0.1 %, 1%, 10%, or Full-scale of range (none).
 Reading Hold Sensitivity: 0.01%, 0.1 %, 1%, or 10% of reading.
 Trigger Delays: 0 to 99 hrs (1ms step size).
 External Trigger Delays: <1ms (2700), <1ms (2701, 2750).
 External Trigger Jitter: <1ms (2700), <500µs (2701), <500µs (2750).
 Memory Size: 55,000 readings (2700), 450,000 readings (2701), 110,000 readings (2750).
MATH FUNCTIONS: Incl. Min/Max/Average/Std Dev/Peak-to-Peak (of stored reading), Limit Test, %, 1/x, and mX+b with user defined units displayed.
REMOTE INTERFACE:
 GPIB (IEEE-488.2) (2700, 2750), RS-232C (2700, 2701, and 2750).
 Ethernet TCP/IP (10/100 and 1000BT) (2701).
 SCPI (Standard Commands for Programmable Instruments).
 LabVIEW Drivers.
ACCESSORIES SUPPLIED: Model 1751 Safety Test Leads, Product Information CD-ROM (Model 2701 only).
 Getting Started Foldout, 3m Ethernet crossover cable, software: CD-ROM with IVI/VISA drivers for VB, VC/C++, LabVIEW, TestPoint, and LabWindows/CVI, plus free runtime start-up software.)
ACCESSORIES AVAILABLE:
 488-70k Black Mount Rear Support Kit (2750)
 77XX-904A Module Manual
 77XX Modules
 Extended Warranty
 ExcelINX-1A (Excel add-in datalogger software)
 TestPoint™ Software Development Package
FOR MODEL 2701:
 Ethernet: RJ-45 connector, TCP/IP, 10/100 and 1000Tx auto-sensed.
 IP Configuration: Static or DHCP.
 Password Protection: 11 Characters.
 Software: Windows 98, NT, 2000, ME, and XP compatible. Internet Explorer 5.0 or higher required. Web page server by 2701.

1.888.KEITHLEY (U.S. only)

www.keithley.com

KEITHLEY

A GREATER MEASURE OF CONFIDENCE

2700, 2701, 2750

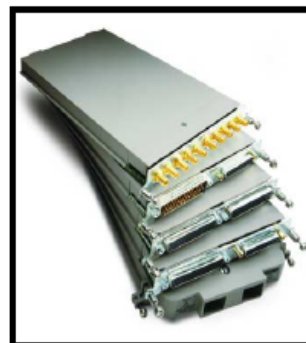
Multimeter/Data Acquisition/ Switch Systems

Switch/Control Module Capabilities

All plug-in modules are compatible with the two-slot Model 2700 and Model 2701 Multimeter/Data Acquisition Systems and the five-slot Model 2750 Multimeter/Switch System. When the application's needs change, simply change modules. Integra systems reconfigure themselves automatically.

Module Capabilities Overview

	7700	7701	7702	7703	7705	7706	7707	7708	7709	7710	7711	7712
DC Volts	✓	✓	✓	✓		✓	✓	✓	✓	✓		
DC Current	✓		✓									
Temperature												
T/C w/Automatic CJC	✓					✓		✓		✓		
T/C w/External CJC	✓	✓	✓	✓		✓	✓	✓	✓	✓		
RTD	✓	✓	✓	✓		✓	✓	✓	✓	✓		
Thermistor	✓	✓	✓	✓		✓	✓	✓	✓	✓		
Resistance (2- or 4-wire)	✓	✓	✓	✓		✓	✓	✓	✓	✓		
Continuity	✓	✓	✓	✓		✓	✓	✓	✓	✓		
AC Volts	✓	✓	✓	✓		✓	✓	✓	✓	✓		
AC Current	✓		✓									
Frequency	✓	✓	✓	✓		✓	✓	✓	✓	✓		
Event Counter/Totalizer						✓						
Signal Routing/Control	✓	✓	✓	✓	✓	✓	✓	✓	✓	✓	✓	✓
Digital Input							✓					
Digital Output						✓	✓					
Analog Output						✓						
RF Switching											✓	✓



1.888.KEITHLEY (U.S. only)

www.keithley.com

KEITHLEY

A GREATER MEASURE OF CONFIDENCE

Integra Series Switch/Control Modules

MULTIMETER/DATA
ACQUISITION/SWITCH SYSTEMS



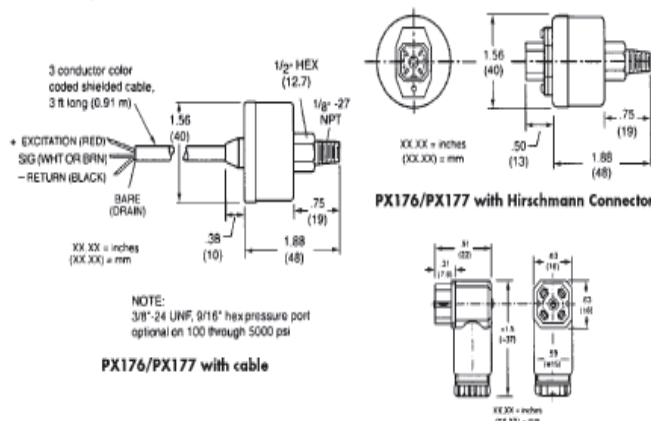
PX176/PX177 Series

Pressure Transducer

INSTRUCTION
SHEET

M0213/1008

Shop online at: omega.com e-mail: info@omega.com
For latest product manuals: omegamail.info



Common Specifications For All Units

Accuracy:	1% FS (includes repeatability, linearity BFSL, and hysteresis)
Proof:	2x FS < or = 300 psi
Pressure:	1.5 FS > or = 500 psi
Burst:	20x FS < or = 25 psi
Pressure:	10x FS < or = 200 psi
	5x FS > or = 500 psi range
Response Time:	50 Hx
Wetted Parts:	Brazed assembly of 300 series SS
Pressure:	1/8 NPT
Port:	3/8 UNF optional on 5000 psi units
Weight:	4 oz.

PX176 Series Voltage Output Specifications

Excitation:	9-20 Vdc @ 15 mA (reverse polarity protected)
Output:	1-6 Vdc
Zero Balance:	1 ± 0.15 Vdc
Span:	
Tolerance:	5 ± 0.1 Vdc
Operating Temp:	-67 to 221° F -55 to 105° C
Compensated Temp:	30 to 185° F -1 to 85° C
Temp Effects:	Zero 1% FS per 100° F change Span 1% FS per 100° F change
Shock Resistance:	50 g's peak @ 5 ms
Electrical Connection:	3 cond shield pigtail leads 3 ft long with drain lead or Hirschmann Connector
Wiring:	Red or Pin #4 White or brown or Pin #2 Black or Pin #3

PX177 Series Voltage Output Specifications

Excitation:	12 to 45 Vdc (reverse polarity protected) linear derating to 35 Vdc from 77° F to 212° F
Output:	4-20 mA
Zero Balance:	4 ± 0.4 mA
Span:	
Tolerance:	16 ± 0.32 mA
Operating Temp:	0 to 212° F -18 to 100° C
Compensated Temp:	30 to 130° F -1 to 54° C
Temp Effects:	Zero 1% FS Span 1% FS
Shock Resistance:	50 g's peak @ 5 ms
Electrical Connection:	2 cond 22 AWG shield pigtail leads 3 ft long with drain lead or Hirschmann Connector
Wiring:	Red or Pin #1 Black or Pin #2

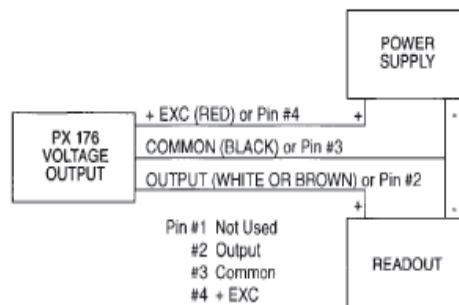
PRECAUTIONS

- Do not use the case of the unit to apply torque to make or break the pressure connection. Always use a wrench on the hex head directly behind the threaded port.
- Do not subject the transducer to high temperature as a result of soldering, brazing, or welding of the system plumbing. In high humidity environments where condensation may occur, mount the transducer so that the connector attaches from the bottom or side. This prevents creating a moisture trap.
- Guard against subjecting the unit to temperatures above its specified maximum during operation.

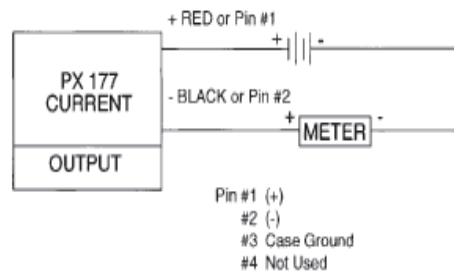
! WARNING - Read Before Installation !

- Fluid hammer and surges can destroy any pressure transducer and must always be avoided. Install a pressure snubber to eliminate the damaging hammer effects.
- Fluid hammer occurs when a liquid flow is suddenly stopped, as with quick closing solenoid valves. Surges occur when flow is suddenly begun, as when a pump is turned on at full power or a valve is quickly opened.
- Liquid surges are particularly damaging to pressure transducers if the pipe is originally empty. To avoid damaging surges, keep fluid lines full (if possible), bring pumps up to power slowly, and open valves slowly. To avoid damage from both fluid hammer and surges, install a surge chamber and a pressure snubber on every transducer.
- Symptoms of fluid hammer and surge's damaging effects:
 - Pressure transducer exhibits an output at zero pressure (large zero offset). If zero offset is less than 10% FS, you can usually rezero the meter, install the proper snubber and continue monitoring pressures.
 - Pressure transducer output remains constant regardless of pressure.
 - In severe cases, there will be no output.

WIRING - PX176 SERIES



WIRING - PX177 SERIES



NOTE: Parts with "-C" suffix have a connector. Spare mating connector part number: PX176-Connector or PX177-Connector.

omega.com newark	OMEGA's On-Line Service omega.com	Internet e-mail info@omega.com
Servicing North America:		
U.S.A.: ISO 9001 Certified	One Omega Drive, Box 4047 Stamford, CT 06907-0047 Tel: (203) 359-1660 Fax: (203) 359-7700 e-mail: info@omega.com	
Canada:	976 Steeles Laval (Quebec) H7L 5A1, Canada Tel: (514) 856-0058 Fax: (514) 856-0886 e-mail: info@omega.ca	
For immediate technical or application assistance:		
U.S.A. and Canada:	Sales Service: 1-800-426-6342 / 1-800-TC-OMEGA® Customer Service: 1-800-422-2378 / 1-800-422-8857* Engineering Service: 1-800-872-9436 / 1-800-USA-WHITE* En Español: (800) 203-359-7803 Fax: (800) 203-359-7807 e-mail: espanol@omega.com info@omega.com.mx	
Mexico:		
Servicing Europe:		
Czech Republic:	Fryská 144, 731 01 Kármán, Czech Republic Tel: +420 (0)59 6311899 Fax: +420 (0)59 6311114 Toll Free: 0800-1-66242 e-mail: info@omega.cz	
Germany/Austria:	Daimlerstrasse 26, D-75392 Dickampfen, Germany Tel: +49 (0)756 9388-0 Fax: +49 (0)756 9388-29 Toll Free in Germany: 0800 639 7678 e-mail: info@omega.de	
United Kingdom: ISO 9001 Certified	One Omega Drive, River Bend Technology Centre Northwick, Leam, Manchester M44 5BD United Kingdom Tel: +44 (0)161 777 6611 Fax: +44 (0)161 777 6622 Toll Free in United Kingdom: 0800-488-488 e-mail: ukinfo@omega.co.uk	

It is the policy of OMEGA Engineering, Inc. to comply with all worldwide safety and EMC/EMI regulations that apply. OMEGA is constantly pursuing certification of its products to the European New Approach Directives. OMEGA will add the CE mark to every appropriate device upon certification. The information contained in this document is believed to be correct, but OMEGA Engineering, Inc. accepts no liability for any errors it contains, and reserves the right to alter specifications without notice. **WARNING:** These products are not designed for use in, and should not be used for, human applications.

WARRANTY/DISCLAIMER
<p>OMEGA ENGINEERING, INC. warrants this unit to be free of defects in materials and workmanship for a period of 13 months from date of purchase. OMEGA's WARRANTY adds an additional one (1) month grace period to the normal one (1) year product warranty to cover handling and shipping time. This ensures that OMEGA's customers receive maximum coverage on each product.</p> <p>If the unit malfunctions, it must be returned to the factory for evaluation. OMEGA's Customer Service Department will issue an Authorized Return (AR) number immediately upon phone or written request. Upon examination by OMEGA, if the unit is found to be defective, it will be repaired or replaced at no charge. OMEGA's WARRANTY does not apply to defects resulting from any action of the purchaser, including but not limited to mishandling, improper interfacing, operation outside of design limits, improper repair, or unauthorized modification. This WARRANTY is VOID if the unit shows evidence of having been tampered with or shows evidence of having been damaged as a result of excessive corrosion, or current, heat, moisture or vibration; improper specification; misapplication; misuse or other operating conditions outside of OMEGA's control. Components in which wear is not warranted, include but are not limited to contact points, fuses, and tritacs.</p> <p>OMEGA is pleased to offer suggestions on the use of its various products. However, OMEGA neither assumes responsibility for any omissions or errors nor assumes liability for any damages that result from the use of its products in accordance with information provided by OMEGA, either verbal or written. OMEGA warrants only that the parts manufactured by the company will be as specified and free of defects. OMEGA MAKES NO OTHER WARRANTIES OR REPRESENTATIONS OF ANY KIND WHATSOEVER, EXPRESSED OR IMPLIED, EXCEPT THAT OF TITLE. AND ALL IMPLIED WARRANTIES INCLUDING ANY WARRANTY OF MERCHANTABILITY AND FITNESS FOR A PARTICULAR PURPOSE ARE HEREBY DISCLAIMED. LIMITATION OF LIABILITY: The remedies of purchaser set forth herein are exclusive, and the total liability of OMEGA with respect to this order, whether based on contract, warranty, negligence, indemnification, strict liability or otherwise, shall not exceed the purchase price of the component upon which liability is based. In no event shall OMEGA be liable for consequential, incidental or special damages.</p> <p>CONDITIONS: Equipment sold by OMEGA is not intended to be used, nor shall it be used: (1) as a "Basic Component" under 10 CFR 21 (NRC), used in or with any nuclear installation or activity; or (2) in medical applications or used on humans. Should any Products be used in or with any nuclear installation or activity, medical application, used on humans, or misused in any way, OMEGA assumes no responsibility as set forth in our basic WARRANTY/DISCLAIMER language, and, additionally, purchaser will indemnify OMEGA and hold OMEGA harmless from any liability or damage whatsoever arising out of the use of the Products in such a manner.</p>

RETURN REQUESTS/INQUIRIES
<p>Direct all warranty and repair requests/inquiries to the OMEGA Customer Service Department. BEFORE RETURNING ANY PRODUCTS TO OMEGA, PURCHASER MUST OBTAIN AN AUTHORIZED RETURN (AR) NUMBER FROM OMEGA'S CUSTOMER SERVICE DEPARTMENT (IN ORDER TO AVOID PROCESSING DELAYS). The assigned AR number should then be marked on the outside of the return package and on any correspondence.</p> <p>The purchaser is responsible for shipping charges, freight, insurance and proper packaging to prevent breakage in transit.</p> <p>FOR WARRANTY RETURNS, please have the following information available BEFORE contacting OMEGA:</p> <ol style="list-style-type: none"> Purchase Order number under which the product was PURCHASED, Model and serial number of the product under warranty, and Repair instructions and/or specific problems relative to the product. <p>OMEGA's policy is to make running changes, not model changes, whenever an improvement is possible. This affords our customers the latest in technology and engineering.</p> <p>OMEGA is a registered trademark of OMEGA ENGINEERING, INC. © Copyright 2008 OMEGA ENGINEERING, INC. All rights reserved. This document may not be copied, photocopied, reproduced, translated, or reduced to any electronic medium or machine-readable form, in whole or in part, without the prior written consent of OMEGA ENGINEERING, INC.</p>

Hypodermic and Mini Hypodermic Probes

Thermocouple and RTD Elements

All probes were designed for industrial, laboratory, manufacturing and chemical research only. They are not intended for medicinal use, or on humans. OMEGA assumes no responsibility if these products are used for medicinal purposes, or on humans, or are misused in any way.

HYP Series

Miniature connector.



OMEGA® Hypodermic Needle Temperature Probes are designed for industrial, laboratory, manufacturing and chemical research applications. Five probe types are available, with diameters from 0.2 to 1.65 mm (0.008 to 0.065"). The HYP0, HYP1 and HYP2 have type T (Copper-Constantan) thermocouple elements, while the HYP3 is available in J, K, T or E calibration, and the HYP4 has a 100 Ω Platinum RTD ($\alpha = 0.00385$).

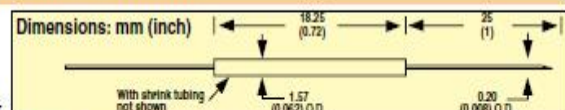
The HYP0 is a mini-hypodermic probe, with 0.2 mm (0.008") diameter. The HYP1 has an OD of 0.3 mm (0.012"), and has an added feature of being steam autoclavable to temperatures up to 160°C (325°F). The HYP3 and HYP4 are industrial probes, with thermocouple and RTD elements respectively.

The HYP0 Mini Hypodermic probe with a needle diameter of only 0.2 mm (0.008") is the least likely to disturb the surrounding insertion

area. Binocular microscope micro-manufacturing techniques result in an extremely small type T (Copper-Constantan) thermocouple being implanted in a 33 gage, 25 mm (1") long stainless steel hypodermic needle. The HYP0 has the fastest response of the hypodermic probes, and has a continuous temperature rating of 200°C (400°F). It has 1.5 m (5') long PFA coated, 36 AWG leads with an SMP type subminiature connector.

Thermocouple Probe Model HYP0

The HYP0 mini-hypodermic probe with a needle diameter of only 0.2 mm (0.008") is the least likely to disturb the surrounding insertion area. Binocular microscope micro-manufacturing techniques result in an extremely small Type T (copper-constantan) thermocouple being implanted in a 33 gage, 25 mm (1") long stainless steel hypodermic needle. The HYP0 has the fastest response of the hypodermic probes, and has a continuous temperature rating of 200°C (400°F). It has 1.5 m (5') long PFA-coated, 36 AWG leads with an SMP-type miniature connector.



To Order

Model No. ANSI Color Code

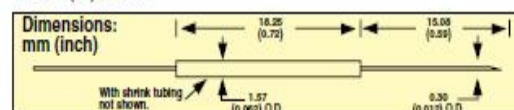
HYP0-33-1-(*)-G-60-SMPW-M

* Specify calibration: K, or T. T = Copper-Constantan, K = CHROMEGA®-ALOMEGA®. Lead wire lengths over 1.5 m (60') at an additional cost/300 mm (12") and modify model number.

Ordering Example: HYP0-33-1-T-G-60-SMPW-M, mini hypodermic probe with Type T grounded thermocouple, 1.5 m (5') long bead wire, and a miniature SMPW male connector.

Thermocouple Probe Model HYP1

OMEGA® Research, autoclavable probe is designed to give instant readings in plants, other semi-solids and liquids. A 30 gage x 15 mm needle provides this very fast response. The measurable temperature range is cryogenic to 200°C (400°F). This is a Type T (Copper-Constantan) grounded-termination probe with PFA insulated extension wire and a subminiature male connector termination. The entire assembly is steam autoclavable to a temperature of 160°C (325°F). All probes have 1.5 m (5') leads.



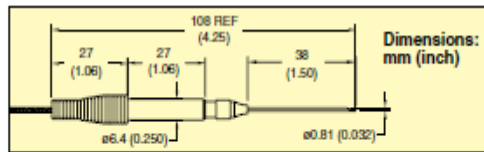
Model No. ANSI Color Code

HYP1-30-1/2-(*)-G-60-SMPW-M

* Specify calibration: K, T, or E. K = CHROMEGA®-ALOMEGA®, T = Copper-Constantan, E = CHROMEGA®-Constantan. For lead wire lengths over 1.5 m (60') at an additional cost/300 mm (12") and modify model number.

Ordering Example: HYP1-30-1/2-T-G-60-SMPW-M, thermocouple probe.

A-93



Thermocouple Probe Model HYP2 and HYP5

The HYP2 and HYP5 Probes have Natural Science, Industrial and Food Processing uses. These assemblies come complete with a Type T (Copper-Constantan) element, 1.2 m (4') PFA insulated lead wires†, and uses a standard (21 gage) hypodermic needle 38 mm (1.5") long. 1.2 m (4') lead wire is standard. Standard size male connector terminates the lead wire.

Model No. ANSI Color Code

HYP2-21-1-1/2-(-)-G-48-OSTW-M

HYP2-21-1-1/2-(-)-G-48-SMPW-M

HYP5-21-1-1/2-(-)-G-SMPW-M

† HYP5 does not have lead wires

* Specify calibration: J, K, T, or E.

J = Iron-Constantan

K = CHROMEGA®-ALOMEGA®

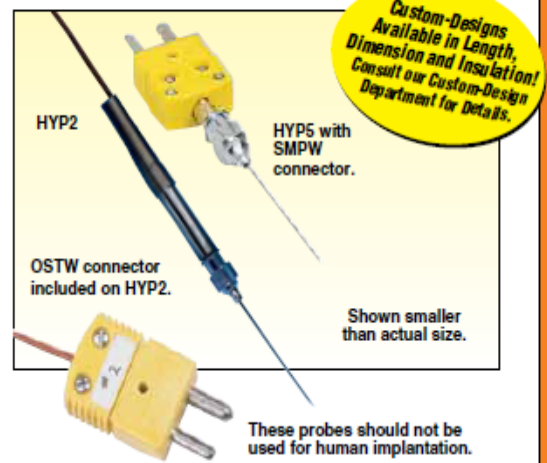
T = Copper-Constantan

E = CHROMEGA®-Constantan

Easy grip handle, add "EGH" suffix, for additional cost.

For lead wire lengths over 1.2 m (48") at an additional cost/300 mm (12") and modify model number.

Ordering Example: HYP2-21-1-1/2-T-G-48-OSTW-M, Type T grounded junction probes.



Thermocouple Probe Model HYP3

OMEGA® Industrial Hypodermic Probe uses a 16 gage x 38 mm (1.5") long needle and may contain J, K, T, E calibrations; they may have a grounded or ungrounded junction, and come with stainless steel overbraided extension wire. The stainless steel overbraiding adds flexibility and extends the probe life. These probes are not autoclavable. They are designed for heavy-duty service. 1.2 m (4') lead wire is standard. Maximum tip temperature is 200°C (400°F).

Model No. ANSI Color Code

HYP3-16-1-1/2-(-)-(**)-48-RP

When ordering, specify calibration and whether grounded or ungrounded junction is desired

* Specify calibration: J, K, T, or E.

J = Iron-Constantan

T = Copper-Constantan

K = CHROMEGA®-ALOMEGA®

E = CHROMEGA®-Constantan

** Specify measuring junction style: U or G

Also Available: R and S (platinum)—consult factory for price and delivery.

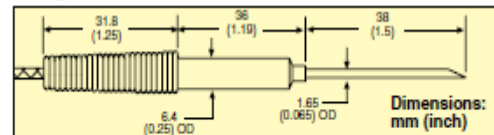
Easy Grip Handle, add "EGH" suffix, for additional cost

For lead wire lengths over 1.2 m (48") at an additional cost/300 mm (12") and modify model number.

To add an SMPW male connector add suffix "-SMPW-M" to model number for additional cost.



Now Available!
M8/M12 CONNECTORS



For a male straight M8 plug add "M8-S-M" to the model number for additional cost, for a male straight M12 plug add "M12-S-M" to the model number for additional cost.

For a male right-angled M8 plug add "M8-R-M" to the model number for additional cost, for a male right-angled M12 plug add "M12-R-M" to the model number for additional cost.

Ordering Example: HYP3-16-1-1/2-K-G-48-SMPW-M, Type K grounded junction probe with 1.2 m (48") leads.

RTD Probe Model HYP4

The RTD Hypodermic Probes are offered for Industrial, Natural Sciences and Food Processing use. These probes contain a 100 Ω platinum RTD ($\alpha = 0.00385$) within a 16 gage x 38 mm (1.5") hypodermic needle, and come with 1.2 m (4') PFA insulated lead wire.

Model No. ANSI Color Code

HYP4-16-1-1/2-100-EU-48-RP

All probes were designed for industrial, laboratory, manufacturing and chemical research only. **They are not intended for medicinal use, or on humans.** OMEGA assumes no responsibility if these products are used for medicinal purposes, or on humans, or are misused in any way.

For lead wire lengths over 1.2 m (48") at an additional cost/300 mm (12") and modify model number.

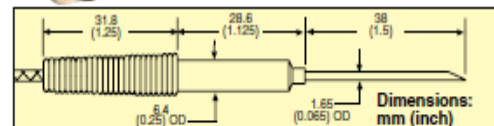
For a male straight M8 plug add "M8-S-M" to the model number for additional cost, for a male straight M12 plug add "M12-S-M" to the model number for additional cost.

For a male right-angled M8 plug add "M8-R-M" to the model number for additional cost, for a male right-angled M12 plug add "M12-R-M" to the model number for additional cost.

To add an MPT-U male connector add suffix "-MTP-M" for additional cost.



Now Available!
M8/M12 CONNECTORS



Ordering Example: HYP4-16-1-1/2-100-EU-48-MTP-M, RTD hypodermic probe with 1.2 m (48") leads and MPT-U male connector.

Appendix F
Turbine Flow Meter Specifications

TURBINE FLOW METER

Stand Alone or Complete Systems with Signal Conditioning

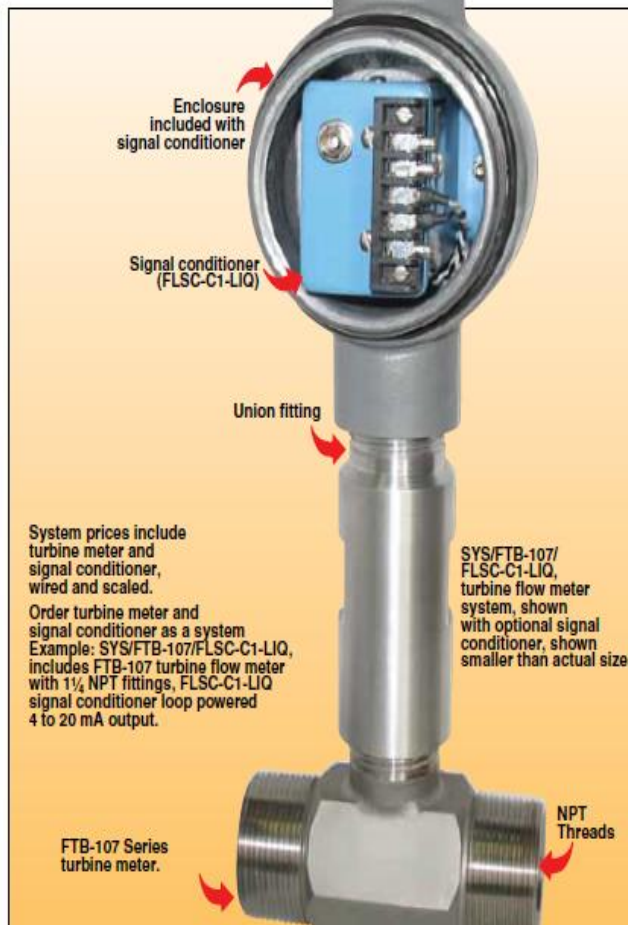
FTB-100 Series



- ✓ $\pm 0.5\%$ of Reading Accuracy
- ✓ Ball Bearing Design for Economy
- ✓ Non-Metallic Bearing Retainers for Long Life
- ✓ Replacement Bearings Field Installable Without Loss of Calibration
- ✓ Disassembles Quickly for Easy Maintenance
- ✓ Deflector Cones Stabilize Low Mass Rotor for Increased Bearing Life
- ✓ 4 to 20 mA, 0 to 5V, and Scaled Frequency Outputs Available

The FTB-100 Series of turbine meters have a shielded ball bearing design for high-accuracy performance ($\pm 0.5\%$ of reading, not full scale) at an economical cost. The non-metallic bearing retainers minimize friction, thereby allowing these meters to be used with clean fluids that have poor lubricating properties (i.e., water). Ball bearings also give the widest linear flow range, particularly in larger turbines. Bearing replacement and clean-up are fast and easy, since all internal parts are easily accessible by removing a single nut.

These turbine flow meters have a low mass rotor design which allows rapid dynamic response, so they can be used in pulsating flow applications.



Deflector cones eliminate downstream thrust on the rotor and allow hydrodynamic positioning of the rotor between the cones. This provides wider rangeability and longer bearing life than conventional turbine flow meters. Integral flow-straightening tubes minimize the effects of upstream turbulence.


FTB-100 Turbine Meters are available with integral signal conditioners which provide scaled and unscaled frequencies, 4 to 20 mA, or 0 to 5 volt outputs. Units without integral signal conditioners are supplied with mating connector for two-wire hook-up.

SPECIFICATIONS

Accuracy: $\pm 0.5\%$ of reading
Repeatability: $\pm 0.1\%$ of reading
Maximum Temperature Range: -268 to 232°C (-450 to 450°F)
Maximum Intermittent Overrange: 150% of maximum range
Minimum Output Amplitude: 30 mV Peak-to-Peak unscaled pulse
Materials of Construction:
Body: 304 stainless steel
Rotor: 17-4 PH steel
Bearings: Ceramic
Minimum straight pipe requirements: 10 pipe diameters upstream, 5 downstream

F-57

Economical Ball Bearing Design with NPT End Fittings



Complete The System

SIGNAL CONDITIONERS
4 to 20 mA, amplified pulse, or 0 to 5 Vdc.

SELECT 1 OR 2

1 **DISPLAY, ALARM, CONTROL DPF60**
Pulse output and voltage or current output.

2 **DISPLAY, TOTALIZE, AND BATCH CONTROL**
Scaled pulse or current output DPF701.

NIST Calibration for Other Viscosity Liquids*

Meter Size	Viscosity Range	
	0.6 to 99 cSt	100 to 299 cSt
FTB-101 thru 106 ½ thru 1"	Additional cost	
FTB-107 thru 109 1¼ thru 2"		
FTB-110 thru 111 2½ thru 3"		

* Standard NIST calibration is for water (viscosity = 1 cSt)

To Order							
Turbine Meter Only Model No.†	Linear Flow Range for Water LPM (GPM)	MNPT End Fittings	Maximum Operating Pressure (psig)	Maximum Pressure Drop (psid)	Length mm (inch)	Nominal K-Factor (Pulses/Gallon)	Weight kg (lb)
FTB-101	1.32 to 13.2 (0.35 to 3.5)	½	5000	3.0	62 (2.45)	13,000	0.4 (1)
FTB-102	2.84 to 28.4 (0.75 to 7.5)	½	5000	5.0	62 (2.45)	10,000	0.4 (1)
FTB-103	4.73 to 36.0 (1.25 to 9.5)	½	5000	5.2	62 (2.45)	6000	0.4 (1)
FTB-104	6.62 to 61 (1.75 to 16)	¾	5000	3.0	70 (2.75)	4100	0.4 (1)
FTB-105	9.5 to 110 (2.5 to 29)	¾	4250	5.0	83 (3.25)	2200	0.4 (1)
FTB-106	15 to 227 (4 to 60)	1	3850	5.1	89 (3.50)	640	0.9 (2)
FTB-107	23 to 352 (6 to 93)	1¼	3850	4.3	99 (3.88)	410	0.9 (2)
FTB-108	30 to 492 (8 to 130)	1½	3000	3.0	111 (4.38)	230	1.4 (3)
FTB-109	57 to 852 (15 to 225)	2	2500	3.3	121 (4.75)	120	1.8 (4)
FTB-110	95 to 1514 (25 to 400)	2½	2250	4.0	154 (6.06)	62	2.3 (5)
FTB-111	151 to 2460 (40 to 650)	3	2000	4.0	191 (7.50)	55	3.2 (7)

Comes complete with operator's manual and 10-point NIST calibration certificate for water.

Ordering Examples: FTB-101, ½ NPT turbine meter with standard NIST calibration for 1 cSt viscosity.

FTB-106, 1 NPT turbine meter with NIST calibration for 5 cSt viscosity liquid.

† Complete systems with signal conditioner available, consult sales.

F-58

F

INTEGRAL OR REMOTE SIGNAL CONDITIONER

FLSC-C1-LIQ



- ✓ Loop Powered
4 to 20 mA
- ✓ Signal Linearization
- ✓ Factory
Configuration
Available
- ✓ Windows®
Configuration
Software*



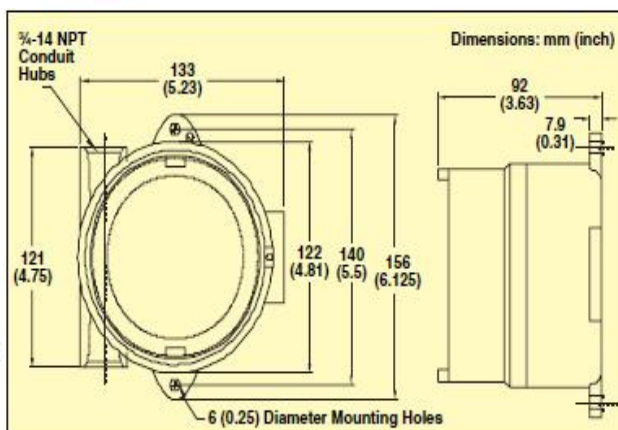
FLSC-C1-LIQ shown
smaller than actual size.

The FLSC-C1-LIQ is a microprocessor controlled 2-wire 4 to 20 mA transmitter. The FLSC-C1-LIQ converts a low level, frequency signal from a flow sensor into an analog 4 to 20 mA output. The output is proportional to the flow rate. The FLSC-C1-LIQ is designed for integral mounting to the FTB-100, FTB-200 and FTB-400 Series** liquid turbines.

** Visit OMEGA for details.

SPECIFICATIONS

Input Signal Type: Magnetic pickup
Input Frequency Range: 0.2 Hz to 4 KHz
Signal Level: 10 mV rms to 30 Vdc
Power Supply: Loop power 10 to 30 Vdc
 Reverse polarity protected
Loop Burden Voltage: 8.5V
Analog Output: 4 to 20 mA
 24 mA overflow condition
Load Resistance: Maximum 650 Ω
 at 24 Vdc
Accuracy: $\pm 0.02\%$ of full scale
Temperature Drift: 40 ppm/degree C
Communications: RS232 port for
 configuration and diagnostics
Operating Temperature: -40 to 85°C
 (-40 to 185°F)
Humidity: 0 to 90% non-condensing
Enclosure: Extruded Aluminum
 Explosion-Proof ATEX enclosure
Regulatory: CE Compliant
 Up to 20 point linearization
 Windows Configuration Software*
 (cable sold separately)



Enclosure meets Class I, Div 1 & 2, Groups A, B, C & D, Class 1, Zones 1 & 2, Groups IIB + H2 IIA, Class II, Div 1 & 2 Groups E, F & G, Class III, NEMA 3, 4, 7(B, C, D) 9(E, F, G), Cenelec EEx d IIC IP66, UL, CSA, FM Approved, ATEX Certified.

To Order

Model No.	Description
FLSC-C1-LIQ	Loop-powered signal conditioner, 4 to 20 mA, CE/ATEX
OM-CONV-USB	USB to RS232 converter
FLSC-C-CABLE	Molex to 9-pin "D" connector

Comes complete with operator's manual and enclosure.

* Available free at omega.com/ftp

Ordering Example: FLSC-C1-LIQ, loop-powered turbine signal conditioner in ATEX enclosure with FLSC-C-CABLE Molex to 9-pin "D" connector.

INTEGRAL OR REMOTE SIGNAL CONDITIONER

FLSC-C3-LIQ



- ✓ DC or AC Powered
- ✓ Pulse and Analog Outputs
- ✓ High or Low Alarms (Optional)
- ✓ 20 Point Linearization
- ✓ Factory Configuration Available
- ✓ Windows® Configuration Software*



FLSC-C3-LIQ shown smaller than actual size.

The FLSC-C3-LIQ is a DC powered, microprocessor controlled transmitter. It outputs a pulse scaled per unit of flow, and analog signal proportional to flow rate.

The FLSC-C3-LIQ-AL can be configured with high or low alarms. The FLSC-C3-LIQ is designed for integral mounting to the FTB-100, FTB-200 and FTB-400 Series** liquid turbines.

** Visit OMEGA for details.

SPECIFICATIONS

Input Signal Type: Magnetic pickup, MCP pickup, contact closure, pulse

Input Frequency Range: 0.2 Hz to 4 KHz

Signal Level: 10 mV rms to 30 Vdc

Power Supply: 13 to 30 Vdc reverse polarity protection

Analog Output: 4 to 20 mA, 1 to 5V 24 mA overflow condition

Load Resistance: Maximum 650 Ω at 24 Vdc

Accuracy: $\pm 0.02\%$ of full scale

Temperature Drift: 40 ppm/degree C

Pulse Output: 0 to 5V, 0 to 10V, open collector, AC square. Internal pull up

10 k Ω . Recommended minimum

load resistance 50 k Ω

Pulse Scaling: Divide by 1, 10 or 100 per flow unit

H/Low Alarm (-AL Model) Optional:

Relay (2A, 30 Vdc), 0 to 5V, open

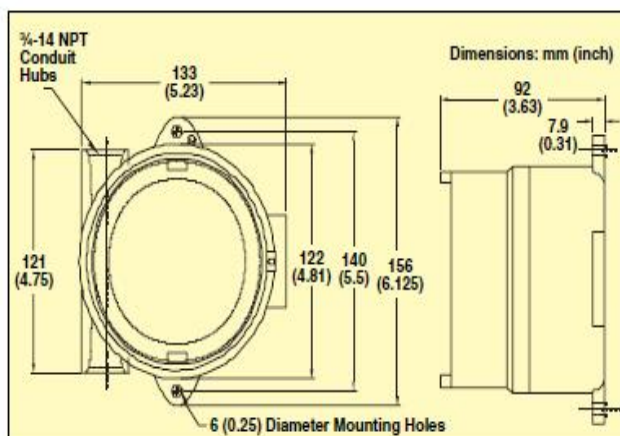
collector (0.5A, 30V)

Communications: RS232 port for

configuration and diagnostics

Operating Temperature: -40 to 85°C

(-40 to 185°F)



Enclosure meets Class I, Div 1 & 2, Groups A, B, C & D. Class 1, Zones 1 & 2, Groups IIB + H2IIA. Class II, Div 1 & 2 Groups E, F & G. Class III. NEMA 3, 4 7(B, C, D) 9(E, F, G). Cenelec EEx d IIC IP66, UL, CSA, FM Approved. ATEX Certified.

Humidity: 0 to 90% non-condensing

Enclosure: Extruded aluminum explosion-proof ATEX

Regulatory: CE Compliant up to 20 point linearization Windows Configuration Software* (cable sold separately)

To Order

Model No.	Description
FLSC-C3-LIQ	DC powered signal conditioner 4 to 20 mA, CE ATEX
FLSC-C3-AL-LIQ	DC powered signal conditioner 4 to 20 mA, alarm CE ATEX
OM-CONV-USB	USB to RS232 converter
FLSC-C-CABLE	Molex to 9-pin "D" connector

Comes complete with operator's manual and enclosure.

* Available free at omega.com/ftp

Ordering Example: FLSC-C3-LIQ, DC powered turbine signal conditioner with FLSC-C-CABLE Molex to 9-pin "D" connector.

F-60